

**The Cosmic Population of Extended Radio  
Sources: A Radio-Optical Study**

A THESIS  
SUBMITTED FOR THE DEGREE OF  
**Doctor of Philosophy**

by

**Kshitij Thorat**

UNDER THE SUPERVISION OF

**Dr. Ravi Subrahmanyam**

and

**Dr. Lakshmi Saripalli**

**Raman Research Institute**

Submitted to

Joint Astronomy Programme, Department of Physics

Indian Institute of Science, Bangalore - 560012



# DECLARATION

I hereby declare that the work presented in this thesis is entirely original and has been carried out by me at the Raman Research Institute under the auspices of the Joint Astronomy Programme of the Department of Physics, Indian Institute of Science. I further declare that this has not formed the basis for the award of any degree, diploma, membership, associateship or similar title of any University or Institution.

Department of Physics  
Indian Institute of Science  
Bangalore -560012  
India

**Kshitij Thorat**  
Date:

## Acknowledgements

I would like to thank here those people without whose help the thesis could not have been written.

First and foremost, I would like to thank my thesis supervisors Prof. Ravi Subrahmanyan and Prof. Lakshmi Saripalli for their guidance, patience and support and for their help in writing of this thesis with prompt and detailed comments and suggestions. I am very thankful to Prof. Tarun Deep Saini, my formal guide at IISc, for his constant help (as well as for teaching me the value of back-of-the-envelope calculations). I thank Prof. Joseph Samuel and Prof. Biman Nath, whose advise this thesis has benefited from.

Thanks must also go to my collaborators, who have helped me better appreciate many aspects of my work. Special thanks go to Prof. Ron Ekers from CSIRO and Dr. Helen Johnston from AAO who have provided insightful comments on the aspects of radio and optical studies, respectively. I take this opportunity to thank Anant Tanna for his help in reducing the radio data and Prof. Brian Schmidt for his help on optical imaging.

I am very thankful to all my teachers in the Ph.D. coursework, whose instruction has formed the basis of my understanding of astronomy. In particular, I thank

---

Dr. Sunita Nair and Prof. Biman Nath for teaching me the basics of radiative processes and Prof. Avinash Deshpande for his lectures (in the ‘village’ !) on radio astronomy. I would also like to thank the faculty members from A. & A. Group in RRI and IISc, whose lectures, discussion and advice has been very helpful to me. I remember with gratitude the time spent with Prof. Ajay Patwardhan at St. Xavier’s College, Mumbai, who introduced me to many advanced concepts in physics.

I am very grateful to the administrative and technical staff at RRI and IISc for their help in various practical matters. I thank Krishna for helping me out several times and Lakshamma and Hanumanthappa for the timely hot beverages. My heartfelt thanks go to Vidya for her care and help in all matters, official as well as personal.

I could not have gone through my Ph.D. life without my friends at IISc and RRI. I thank Shashikant, Wasim, Ruta, Harshal and Siddharth for the long discussions on technical and non-technical matters. I thank Mamta, Kanhaiya, Nishant, Lijo, Nazma, Mayuri, Bidya, Arunima, Harsha and other friends and colleagues on astro floor for their help and support. My special thanks to Anagha, Chandreyee and Nipanjana for putting up with many of my faults and oddities and for providing help and tea whenever needed.

I am very grateful to Fluffy, Bluffy, Whiskey and Kandapi for their presence and without whom hard times would have been harder still.

I finally thank my family and Madhura for their incredible patience and their unwavering faith.

# Synopsis

## Introduction

This thesis presents studies of cosmic populations of extragalactic radio sources. The problems selected for this thesis are 1) the derivation of constraints on the emergence of new sub-mJy populations at flux density below about 1 mJy (at 1.4 GHz) paying careful attention to including sources with low surface brightness and counting sources rather than components 2) development of a new method to estimate the asymmetry in the large scale galaxy environment with respect to the axes of extended radio sources and use this to examine for evidence of impact of the environment on the morphology of radio sources. The studies presented herein have been carried out using the Australia Telescope Low Brightness Survey (ATLBS), which is a sensitive radio survey at 1.4 GHz, imaging 8.42 square degrees of the sky along with accompanying optical observations of the same region.

There are multiple populations of extragalactic radio sources in the cosmos. These consist of populations of powerful radio-loud quasars and radio galaxies to populations of weaker radio sources such as star-forming galaxies. These popu-

---

lations of radio sources show evidence of evolution with cosmic epoch. Because the radio galaxy phenomenon and the AGNs at the centers of their host galaxies may influence the evolution of the galaxy via feedbacks, examinations of these source populations over cosmic time are a necessary complementary study to understanding the process of galaxy formation and in general, cosmology. Below we give brief introduction to the problems studied in this thesis.

## Sub-mJy Radio Source Counts

Radio source counts, which have historically been a key probe of cosmology, now represent a measure of cosmological evolution in radio source populations. Currently, the estimation of source counts at sub-mJy flux density as well as the nature and evolution of these sources is undetermined. At flux densities  $\leq 1.0$  mJy a ‘flattening’ of normalized differential source counts has been widely reported in literature (Windhorst et al. (1985), Hopkins et al. (2003), Huynh et al. (2005) and references therein). The flattening is observed as an apparent change of slope for the normalized differential source counts from  $\sim 0.7$  at  $5.0 - 100.0$  mJy to about  $0.4$  in the  $0.25 - 5.0$  mJy range. Attempts to understand the nature of the sub-mJy population have arrived at discordant results and identify the sub-mJy sources with different populations: starburst galaxies (Condon (1989), Benn et al. (1993), Huynh et al. (2005)), early type galaxies (Gruppioni et al., 1999), low (radio) luminosity active galactic nuclei (AGNs) (Huynh et al., 2008) or a mixture of these. Due to unavailability of spectroscopically complete samples of hosts of sub-mJy sources, the exact nature of the sub-mJy radio source population is currently uncertain. However, the presence of a population which

---

emerges at sub-mJy flux density and is different from the AGN-dominated radio source population is not in doubt. The studies in the literature are inconsistent in identifying the precise location of the emergence of flattening in counts at sub-mJy flux density. Several studies show that the source counts are consistent with a continuation in the slope of the differential counts below mJy flux density (Prandoni et al. (2001) and Subrahmanyan et al. (2010)). The scatter in the sub-mJy counts from different studies may be because of the relatively small areas covered by deep surveys (in many cases, a single pointing of an interferometric array) which may have relatively large errors arising from large scale clustering in the spatial distribution of cosmic radio sources (however the study by Condon (2007) concludes that the scatter in the source counts stems from variations in corrections and sensitivity in different studies) In contrast, wide-field surveys may not reach the depth to probe sub-mJy counts. Another reason is the correction applicable to the observed source counts necessary to estimate the true source counts; these are especially pertinent at low flux densities. To resolve these issues, a survey which combines the attributes of wide spatial coverage as well as excellent sensitivity and a procedure which accounts for the biases in estimation of the sub-mJy source counts is needed. In conclusion, accurate measurements of the source counts at sub-mJy flux densities are needed to correctly estimate the cosmic evolution of radio sources.

## **Environments of Extended Radio Sources**

Another issue of importance in the study of extragalactic radio sources is their interaction with their environments. The gas environments in which radio sources

---

reside and evolve ought to have an influence on the morphology of the radio sources. This has been shown in many case studies where the radio structures have been compared with the X-ray gas environments (Blanton et al. (2011); Boehringer et al. (1993)). Studies of the optical environments of radio galaxies have also been carried out previously (Longair & Seldner, 1979; Yee & Green, 1984; Hill & Lilly, 1991; Zirbel, 1997). The motivation behind these studies has been to examine differences between different classes of radio sources, the evolution of environments with cosmic epoch as well as the possibility of identifying clusters/groups of galaxies using radio sources as a tracer (Wing & Blanton, 2011). Many previous studies have found that the environments of FRI/FRII sources are different and are dependent on the cosmic epoch. FRI sources, typically, are found in rich environments. FRII sources in the local universe are generally hosted by field galaxies, but at higher redshifts are found in richer environments (Hatch et al., 2011; Best et al., 2003; Overzier et al., 2008). However, there have been fewer studies that relate the richness of the environments and morphological asymmetries of radio galaxies. Earlier investigations by Subrahmanyan et al. (2008) and Safouris et al. (2009) are noteworthy in this regard where the radio structures of two giant radio galaxies were examined in the context of the large-scale galaxy distributions in their vicinity (also see Chen et al. (2012) and references therein). The study was also used to infer properties of the ambient thermal gas medium in which the structures evolved. Clear correlations between structural asymmetries and associated extended emission-line gas were also found for radio galaxies that have relatively smaller sizes of a few hundred kpc (McCarthy et al., 1991).

---

## Thesis Work

To progress the field in the problems highlighted above, the following work has been done in this thesis.

### Radio Imaging of ATLBS Survey

To characterize the cosmic evolution of radio sources and their properties, observations and imaging of faint radio sources is essential. The Australia Telescope Low Brightness Survey (ATLBS), which has been used in the studies presented in this thesis, has been designed specifically to image diffuse radio emission to relatively high redshifts ( $z \sim 1 - 1.5$ ). Therefore obtaining good surface brightness sensitivity was a prime objective in planning the radio observations and in imaging the data obtained from these observations. This requires a nearly complete synthesized aperture and observations of a representative patch of the extragalactic sky. These requirements have been fulfilled in ATLBS survey, which has excellent uv coverage, especially at short spacings, and images a region off the galactic plane that is devoid of strong radio sources. The observations were carried out for two adjacent fields, designated as A and B with their centers at RA:00<sup>h</sup> 35<sup>m</sup> 00<sup>s</sup>, DEC:−67° 00′ 00″ and RA:00<sup>h</sup> 59<sup>m</sup> 17<sup>s</sup>, DEC:−67° 00′ 00″, in the 20 cm band, with a center frequency of 1388 MHz, in full polarization mode. The radio data was imaged by using techniques such as multi-frequency deconvolution and self-calibration to make two mosaics of region A and B which are free of artefacts.

These high-resolution radio images (with beam FWHM of 6″) of the ATLBS

---

survey regions cover 8.42 square degrees sky area with rms noise  $72 \mu\text{Jy beam}^{-1}$  and are of exceptional quality in that there are no imaging errors or artifacts above the thermal noise over the entire field of view. The images have excellent surface brightness sensitivity and hence provide good representation of extended emission components associated with radio sources.

## **Optical Imaging of ATLBS Survey**

The ATLBS survey region has been also observed in SDSS  $r'$  band, specifically for providing information about the galaxies hosting radio sources observed in ATLBS survey as well as galaxies in the neighbourhood of the radio sources. The optical observations were carried out using the CTIO 4 meter Blanco Telescope in Chile and using the MOSAIC II imager, which is a mosaic of 8 CCDs. In total, 28 optical images were created from the optical data. Each image was formed from a set of 5 dithers, using which spurious sources in the images were rejected. The final images are complete down to a magnitude of 22.75.

## **Radio Source Counts**

Using the sensitive radio and optical images, a study of radio source counts was carried out. This study made use of some novel strategies and algorithms to generate a source list and correct it for various biases to obtain the radio source counts. More specifically, care was taken to identify sources with low surface brightness by making use of low resolution images for initial identification, and using multiple indicators (including optical images) to identify components of sources. The blending issues inherent in using low resolution images has been

---

avoided using higher resolution images to identify blended sources. Thus, use of low resolution images (beam FWHM =  $50''$ ) almost completely removes effects of resolution bias and the use of high resolution images avoids blending issues. These strategies, together with use of optical images to locate candidate galaxy hosts and a careful visual examination of resolved and complex sources instead of automated classification ensures that the ATLBS catalog is a ‘source catalog’ as opposed to a ‘component catalog’. The distinction between ‘sources’ (which are single sources) as opposed to components (parts of a single source appearing separate) is crucial in estimating the true source counts.

The source list was used to estimate the radio source counts down to 0.4 mJy. Comparing the counts with previous work shows that the ATLBS counts are systematically lower and the upturn in sub-mJy source counts has not been found down to the noise limited flux densities probed. The systematically low counts for ATLBS relative to most previous studies are attributed to the ATLBS counts representing sources as opposed to components, as well as corrections for noise bias as well as clustering effects that may affect source counts derived from the small sky coverage typical of deep surveys. This study also demonstrates the substantial difference in counts that result from using component catalogs as opposed to source catalogs: at 1 mJy flux density component counts may be as much as 50% above true source counts. This implies that automated image analysis for counts may be dependent on the ability of the imaging to reproduce connecting emission with low surface brightness as well as the ability of the algorithm to recognize sources, which require that source finding algorithms effectively work with multi-resolution and multi-wavelength data.

---

## Galaxy Environments of Extended Radio Sources in ATLAS Survey

A study of the galaxy environments of the extended sources in the ATLAS survey was carried out using the optical images. This study of the environments of radio sources from the ATLAS survey is restricted to those that are extended and hence to a subset of the ATLAS-ESS (Extended Source Sample) sources. Briefly, the ATLAS-ESS subsample consists of 119 radio sources that have angular size exceeding  $0'.5$ . Applying a redshift cut (to exclude sources with high redshifts whose optical environment may be beyond the depth of the optical images) as well as other constraints (such as availability of optical magnitudes of the host galaxy), a sub-sample of 43 sources was formed, including sources of diverse radio morphologies (FRI/FRII, WATs and HTs) as well as 7 radio sources which are highly asymmetric in their radio morphology. For these sources, where no spectroscopic data was available, a redshift estimate was obtained from a magnitude-redshift relation derived from other sources in the ATLAS survey. Using the optical images convolved with a matched filter (following the prescription from Postman et al. (1996)) consisting of a radial and magnitude filter, smoothed maps were formed for each source in the sample. These give the likelihood of a cluster being present in a given position in the map (in this case the location of interest being the position of the radio source in the map). Further, five parameters were defined in this study, which give estimates of the *angular anisotropy* of galaxy density around the axis of the radio source. This method used to quantify environmental asymmetry for the study presented in the thesis is new.

---

The parameters defined thus were used to examine the environments of radio sources in the sample over a wide range in redshift. Specifically a comparison of FRI/FRII environments was made in two different redshift regimes (above and below  $z = 0.5$ ) and it was found that the FRI and FRII sources inhabit environments of similar richness at low and high redshifts, with no evidence for redshift evolution. The WAT and HT sources were (as expected from earlier studies in literature) found in the most dense environments. Examination of the anisotropy parameters for the asymmetric radio sources clearly showed the influence environment has on radio source morphology, specifically in that the higher density of galaxies was found on the shorter side of the radio sources in almost all cases.

## **Images and Other Resources**

The radio and optical images are an excellent resource for examining with automated algorithms for source finding, parameter fitting, and morphological classification, and as a resource for testing such algorithms that would be used on upcoming all-sky continuum surveys with the LOFAR and ASKAP/SKA. The techniques and methods developed and presented in the thesis may be used in future studies of radio source populations.

---

## Publications

### REFEREED PUBLICATIONS

1. ATLBS EXTENDED SOURCE SAMPLE: THE EVOLUTION IN RADIO SOURCE MORPHOLOGY WITH FLUX DENSITY, Saripalli, L.; Subrahmanyan, R.; **Thorat, K.**; Ekers, R.D.; Hunstead, R.W; Johnston,H. M.; & Sadler, E.M.,2012, ApJS, 199, 27.
2. HIGH RESOLUTION IMAGING OF THE ATLBS REGIONS: THE RADIO SOURCE COUNTS, **Thorat, K**; Subrahmanyan, R.; Saripalli, L.; Ekers, R.D., 2012, ApJ, 762, 16
3. ENVIRONMENTS OF EXTENDED RADIO SOURCES IN ATLBS SURVEY, **Thorat, K**; Saripalli, L.; Subrahmanyan, R. *Accepted for publication in MNRAS.*

### CONFERENCE PROCEEDINGS

1. RADIO-OPTICAL IMAGING OF THE ATLBS SURVEY, Thorat., K.; Conference Proceedings of International Conference on Diffuse Relativistic Plasmas; J. Astrophys. Astr., 32, 495-496

# CONTENTS

<b>1</b>	<b>Introduction</b>	<b>1</b>
1.1	A Short History of Radio Surveys . . . . .	1
1.1.1	Wide-field Surveys . . . . .	3
1.1.2	Deep Radio Surveys . . . . .	6
1.2	Extragalactic Radio Sources . . . . .	10
1.2.1	Radio Galaxies . . . . .	11
1.2.2	Star Forming Galaxies and Faint Radio Sources . . . . .	17
1.3	Motivation for the thesis work . . . . .	19
1.4	Summary . . . . .	21
<b>2</b>	<b>Radio Observations and Imaging</b>	<b>23</b>
2.1	Australia Telescope Compact Array . . . . .	25
2.2	Observations . . . . .	27
2.3	Imaging . . . . .	29
2.3.1	Clean Bias . . . . .	34
2.4	Final Mosaic Images . . . . .	35
2.5	Summary . . . . .	36

## CONTENTS

---

<b>3</b>	<b>Optical Observations and Imaging</b>	<b>43</b>
3.1	Introduction . . . . .	43
3.2	CTIO 4-meter Telescope . . . . .	44
3.3	Observations . . . . .	44
3.4	Data Reduction and Imaging . . . . .	46
3.4.1	Calibration . . . . .	47
3.4.2	WCS Setting . . . . .	50
3.4.3	Stacking . . . . .	51
3.5	Photometry . . . . .	52
3.5.1	Standard Star Photometry . . . . .	53
3.5.2	Photometry of Survey Fields . . . . .	54
3.5.2.1	Star - Galaxy Separation . . . . .	55
3.5.2.2	Comparison of Galaxy Counts . . . . .	58
3.6	Summary . . . . .	58
<b>4</b>	<b>The radio source counts</b>	<b>61</b>
4.1	Introduction . . . . .	61
4.2	On the identification of sources in the ATLBS survey . . . . .	68
4.2.1	Thermal Noise Considerations . . . . .	68
4.2.1.1	Detection Threshold in the Low Resolution Image	69
4.2.1.2	Detection Threshold in the High Resolution Image	71
4.2.2	Source Blending-Confusion . . . . .	73
4.2.3	Bandwidth Smearing Correction . . . . .	76
4.2.4	On the classification of radio sources in the ATLBS survey	80

4.2.4.1	Initial Source Classification Using the Low Resolution Image . . . . .	80
4.2.4.2	Final Source Classification Based on the High Resolution Image . . . . .	80
4.2.5	The identification of Sources with Complex Structures . . . . .	84
4.2.6	Completeness in radio source detection . . . . .	87
4.3	Source Counts . . . . .	89
4.3.1	Corrections to the source counts . . . . .	90
4.3.1.1	Noise Bias Correction . . . . .	90
4.3.1.2	Effective Area Correction for Sources . . . . .	91
4.3.1.3	Effective Area Correction for Blended Sources . . . . .	92
4.3.1.4	Resolution Bias Correction . . . . .	93
4.3.1.5	The ATLBS source counts . . . . .	95
4.4	A discussion on the slope and magnitude of the counts at sub-mJy flux densities . . . . .	95
4.5	Summary and conclusions . . . . .	103
<b>5</b>	<b>Environments of Extended Radio Sources</b>	<b>107</b>
5.1	Introduction . . . . .	107
5.2	Sample Definition and Selection . . . . .	111
5.3	Redshift-magnitude relation . . . . .	112
5.4	Quantifying the galaxy environments of extended radio sources . . . . .	113
5.4.1	Description of the Method . . . . .	118
5.4.2	Implementation of the Method . . . . .	120
5.4.3	Parameters quantifying radio source environment . . . . .	123

## CONTENTS

---

5.5	Results and Discussion . . . . .	127
5.5.1	The environments of Head-Tail and Wide-angle Tailed ATLBS- ESS sources . . . . .	128
5.5.2	The environments of FR I and FR II ATLBS-ESS sources	130
5.5.3	Dipole and quadrupole environmental anisotropy . . . . .	135
5.5.4	Asymmetric ATLBS-ESS sources . . . . .	137
5.6	Summary . . . . .	140
<b>6</b>	<b>Conclusions</b>	<b>145</b>
6.1	Summary and Results . . . . .	146
6.2	Pathways for Continued Work . . . . .	149
<b>A</b>	<b>Appendix</b>	<b>151</b>

## LIST OF FIGURES

1.1	Deep radio surveys in limiting flux density-survey area plane . . .	10
1.2	Radio Image of Cygnus A . . . . .	12
2.1	ATCA Interferometer . . . . .	25
2.2	Radio pointing with sidelobe sources . . . . .	31
2.3	Radio pointing with sidelobe sources removed . . . . .	32
2.4	ATLBS survey regions . . . . .	36
2.5	Representative area from region A . . . . .	37
2.6	Representative area from region B . . . . .	38
2.7	Source in low-resolution radio image overlaid on optical image . .	39
2.8	Source in high-resolution radio image . . . . .	40
2.9	Representative radio sources . . . . .	41
3.1	The CTIO 4-meter Blanco Telescope . . . . .	45
3.2	Stellarity index distribution . . . . .	56
3.3	Plot of Half-light radius (in pixels) versus total $r'$ band magnitude	58
3.4	Optical galaxy counts . . . . .	59

## LIST OF FIGURES

---

4.1	Simulated source counts-single population . . . . .	63
4.2	Simulated source counts-two populations . . . . .	64
4.3	Differential source counts-complete . . . . .	96
4.4	ATLBS differential source counts with reduced bin-width . . . . .	99
4.5	Component to source ratio as a function of flux density . . . . .	101
4.6	Differential source counts for component catalog . . . . .	102
4.7	Final differential source counts for ATLBS . . . . .	104
5.1	Examples of radio sources used in environments study . . . . .	110
5.2	Magnitude-redshift relation . . . . .	114
5.3	Smoothed map of the environment of the source J0024.4–6636 . . . . .	123
5.4	Schematic depiction of the overdensity parameters . . . . .	126
5.5	Histograms of $a_1$ parameter for (a) WAT/HT and (b) FRI/FRII sources. . . . .	129
5.6	Environments of high and low redshift FRI/FRII sources . . . . .	134

## LIST OF TABLES

4.1	Source types and classification criteria . . . . .	86
4.2	The ATLBS survey 1.4 GHz Source Catalog . . . . .	88
4.3	ATLBS 1.4 GHz source counts with a self-calibrated noise bias . .	103
5.1	Sources used to fit the magnitude-redshift relation . . . . .	115
5.1	Table. 5.1 continued. . . . .	116
5.2	Environmental overdensity parameters for extended sources . . . .	142
5.3	Environmental overdensity parameters for asymmetric sources . .	143



## Introduction

This thesis presents studies of extragalactic radio source populations using the Australia Telescope Low Brightness Survey (ATLBS) and accompanying optical observations. The work concerns the characterization of the radio sources and their optical environments. In this chapter of the thesis, I present the background for the work carried out for the thesis, focusing on extragalactic radio sources and radio surveys off the Galactic plane. More detailed introductions to the specific studies presented in later chapters form the opening sections of the individual chapters.

### **1.1 A Short History of Radio Surveys**

The first radio observations were carried out by Karl Jansky in the 1930s. He had discovered radiation at radio frequencies (20.5 MHz) which could not be ac-

## 1. INTRODUCTION

---

counted for by any terrestrial sources. Initially attributed to the Sun, he soon believed it to be from outside the Solar System and more specifically directly from the center of the Galaxy. His work was taken up by Grote Reber in the following decade who reached the same conclusion, that the so called ‘cosmic static’ had origins outside of the Solar System (Reber, 1940). The observations carried out by Reber and others showed that the radio signals were coming from the Galactic plane.

By 1949, several such radio sources had been identified with astronomical objects observed in other wavebands. These objects included Taurus A (Crab Nebula), Virgo A (NGC 4486 or M87) and Centaurus A (NGC 5128) (Bolton et al., 1949). Two of these objects were thus identified with galaxies, marking the beginning of extragalactic radio astronomy. Soon more radio sources, including Cassiopeia A and Puppis A (both supernova remnants) and Cygnus A (a radio galaxy), were identified with optical counterparts (Baade & Minkowski, 1954).

These early findings provided the impetus for the first radio surveys to serve as a basis for examining the population of radio sources, their identifications and phenomenology and cosmic evolution. A notable series of surveys is the Cambridge radio surveys. This series of surveys includes the 2C survey, which highlighted the issue of source confusion in radio surveys. This was amended in the next survey in the series, the 3C survey, in which the operating frequency of the telescope was increased from 81.5 MHz to 159 MHz, which resulted in a better resolution by a factor of two (Archer et al. (1959), Edge et al. (1959)). The 3C survey produced more reliable flux densities and positions for radio sources than

## 1.1 A Short History of Radio Surveys

---

its predecessor. The 3C survey is also notable for detecting the first quasar ever, 3C 273 (Schmidt (1963), Oke & Schmidt (1963)). The 273<sup>rd</sup> object in the 3C survey catalog, it was identified with an optical counterpart which could not be resolved in optical observations. The angular size of the optical counterpart was ‘point like’, as in the case of a star (i.e. given by the ‘seeing’), but spectroscopy revealed presence of several broad (width  $\sim 50\text{\AA}$ ) optical emission lines superimposed on a flat continuum which was unlike any star. This unusual spectrum could be explained if the object had a redshift of 0.158. Thus the object was named as a ‘Quasi-Stellar Object’ or ‘Quasar’. Successive Cambridge surveys have continued, with the most recent being the 10<sup>th</sup> Cambridge survey (10C) (Franzen et al., 2010) carried out with the Arcminute Microkelvin Imager Large Array at 15.7 GHz.

Radio surveys may be divided into two types: wide-field radio surveys and deep radio surveys. This is because of the fact that the observing time for any survey is a limited resource and the depth of a survey comes at the expense of sky coverage it may undertake. Both types of surveys are useful for different objectives. In the next part of this chapter different radio surveys are discussed. A comprehensive review of continuum radio surveys can be found in de Zotti et al. (2010).

### 1.1.1 Wide-field Surveys

Some of the prominent wide-field surveys are the Parkes-MIT-NRAO (PMN), the Westerbork Northern Sky Survey (WENSS), the Sydney University Molonglo Sky

## 1. INTRODUCTION

---

Survey (SUMSS), the Faint Images of Radio Sky at Twenty-centimeter (FIRST) and the NRAO VLA Sky Survey (NVSS).

The PMN survey (Griffith & Wright, 1993; Wright et al., 1994; Griffith et al., 1994; Condon et al., 1993; Tasker et al., 1994; Griffith et al., 1995; Wright et al., 1996) is an all sky survey carried out at 4.85 GHz. The primary aim of the PMN survey was to provide radio observations complementary to those carried out with the Green Bank Survey (Griffith & Wright, 1993; Gregory et al., 1996) (also at 4.85 GHz). The PMN survey, covering the sky from  $-87.5^\circ \leq \delta \leq 10^\circ$ , catalogs a total of 50814 sources at flux limits varying from 20 mJy to 72 mJy depending on the declination, imaged with beam FWHM  $\sim 5'$ . Together with the Green Bank survey (from  $0^\circ \leq \delta \leq 75^\circ$ ), it provides radio coverage for nearly the whole sky at relatively high frequencies.

The WENSS survey (Rengelink et al., 1997), carried out at much lower frequencies (325 MHz and also at 610 MHz) as compared to the PMN and Green Bank surveys, covers the northern sky beyond the declination of  $30^\circ$  with beam FWHM  $\sim 54''$  to a flux limit of 18 mJy. Apart from sky coverage, WENSS is useful in obtaining the spectral information of northern sky radio sources, either by comparing fluxes with other northern sky radio surveys or on its own. WENSS survey is also useful in detection of diffuse radio sources (see van Weeren et al. (2010) and van Weeren et al. (2011), for example) due to the relatively superior surface brightness sensitivity.

The SUMSS survey (Bock et al. (1999); Mauch et al. (2003)) is a low fre-

## 1.1 A Short History of Radio Surveys

---

quency (843 MHz) survey in the southern sky, covering a region below declination of  $-30^\circ$  with beam FWHM of  $\sim 43''$  and complete to flux density of 8 mJy or 18 mJy (for below and above declination of  $-50^\circ$  respectively). The SUMSS survey contains 211063 objects that have been recently cataloged.

Perhaps the most widely used radio surveys in recent times are the NVSS and FIRST surveys. These two surveys, carried out with the Very Large Array radio interferometer, complement each other. The NVSS survey (Condon et al., 1998) provides coverage for the entire sky north of declination  $-40^\circ$  at a frequency of 1.4 GHz to a limit of 2.5 mJy, cataloging about 1.8 million sources. The NVSS survey images are of relatively low resolution (FWHM =  $45''$ ), which make the images useful in detection of extended, diffuse radio emission (Solovyov & Verkhodanov, 2011). The very wide coverage it provides lends itself to be used in cosmological studies, especially in the detection of Integrated Sachs-Wolfe (ISW) effect (see Dupé et al. (2011) and references therein). The FIRST survey (Becker et al., 1994, 1995), which was also carried out at 1.4 GHz, has a higher resolution (FWHM =  $5''$ ). The FIRST survey covers (by design) similar area to the SDSS optical survey (York et al., 2000). Due to this fact, various multi-wavelength studies of radio sources have been possible in which lists of sources from FIRST and SDSS surveys are cross-matched (see Urrutia et al. (2009), McGreer et al. (2009), Hodge et al. (2009), as examples).

## 1. INTRODUCTION

---

### 1.1.2 Deep Radio Surveys

Compared to the surveys listed above, which have very large coverage of the sky but relatively shallow depth in terms of the limiting flux density, some surveys have been especially designed to probe deeper limiting flux densities. Where large-area surveys are able to provide large databases of relatively bright radio sources, deep radio surveys provide information about the faint radio source population, making them essential in studies of evolution as well as composition of radio source populations.

Some examples of deep surveys include the Phoenix Deep Survey (PDS) (Hopkins et al., 1998), the Australia Telescope ESO Slice Project (ATESP) survey (Prandoni et al., 2000), the Australia Telescope Hubble Deep Field-South radio survey (ATHDFS) (Norris et al., 2005). Deep surveys typically cover sky regions of a few square degrees and probe sub-milliJansky flux density. These flux density regions contain very faint radio source populations, the composition of which is the matter of much debate. A more extensive discussion and investigation of this issue has been presented in Chapter 4.

A host of deep radio surveys were carried out with the VLA radio interferometer, which include the VLA ELAIS survey, VLA VIRMOS survey, VLA HDFN survey, VLA COSMOS survey and VLA Swire survey. The VLA ELAIS (European Large-Area ISO Survey) (Ciliegi et al., 1999), was carried out at 1.4 GHz to image the regions surveyed in infrared bands in the European Large-Area ISO Survey. Covering 4.22 square degrees, it was able to achieve a flux density limit

## 1.1 A Short History of Radio Surveys

---

down to 0.135 mJy in selected deep regions. The survey importantly provides information complementary to that obtained from the infrared observations of the same region which helps better estimate the radio-infrared correlation. The VLA ELAIS survey also probes the sub-milliJansky radio source population. The VLA VIRMOS survey (Bondi et al., 2003) at 1.4 GHz provides radio coverage for 1 square degree subfield of the region surveyed in the optical band in the VLT VIRMOS survey. It reaches a flux density limit of 0.08 mJy; giving 1013 radio sources in the catalog. The HDFN (Hubble Deep Field-North, covered in optical by deep Hubble Space Telescope observations) survey (Richards, 2000) covered only 40', but probed the sub-milliJansky regime down to 40  $\mu$ Jy, with a catalog of 371 radio sources. The VLA Swire survey (Owen & Morrison, 2008), covering 40'  $\times$  40' at 1.4 GHz, probes the Lockman Hole area (covered as a part of Spitzer Wide-area InfraRed Extragalactic survey) down to 20  $\mu$ Jy. The VLA COSMOS (Schinnerer et al., 2007) survey is another survey where radio observations have been carried out along with observations in other wavebands, providing multi-frequency coverage for a given sky area. In the case of VLA COSMOS survey (which covers 2 square degrees of sky covered in the Cosmic Evolution Survey) the coverage ranges from X-ray band to radio, including optical spectroscopic observations. The VLA COSMOS survey provides a catalog of 3643 radio sources at 1.4 GHz. Amongst the most recent deep radio surveys is the survey of the Lockman Hole (same area as that covered by the VLA Swire survey) by Condon et al. (2012), which is one of the deepest radio surveys yet, reaching down to the limit of 1  $\mu$ Jy.

Though deep surveys are very important in probing the faint radio source

## 1. INTRODUCTION

---

population, deep surveys may suffer due to the small coverage. This may result in errors in the estimates of properties of the radio source populations, especially number counts. The source counts of radio sources may be affected due to clustering effects. Recent studies have tried to estimate the effect of clustering on radio source counts. For example, Condon (2007) has estimated the rms fluctuations in radio source counts in 17 non-overlapping fields using the FLS-VLA survey (Condon et al., 2003) and found that the clustering in small fields may not be cosmic in origin, but may depend on issues such as varying sensitivity over survey regions. A similar study by Prandoni et al. (2001) also found that clustering effects on estimation of source counts may not be significant. More recently, however, the study by Heywood et al. (2013) has demonstrated that the contribution of clustering effects or ‘sample variance’ may be quite important in correct estimation of the radio source counts. The latter study carried out simulations in which areas of sky of different sizes (‘broad’ patches of size 4.5 square degrees and ‘deep’ patches of 0.196 square degrees) containing radio sources were simulated and the scatter in the source counts were studied. It was demonstrated in this study that significant scatter may be introduced in source counts through clustering of sources, depending on the limiting flux density threshold of the survey; this issue is most severe in deep radio surveys covering small area.

In the future, radio surveys will be carried out using telescopes designed to instantaneously survey large sky areas with excellent flux density sensitivity. One of the primary aims of telescopes such as LOFAR, MEERCAT, ASKAP etc. is carrying out deep continuum radio surveys, which provide information about the radio sky with an order of magnitude improvement over most of the existing deep

## 1.1 A Short History of Radio Surveys

---

surveys in both limiting magnitude and the sky coverage (see Fig. 1.1). For a comprehensive review of the upcoming radio continuum surveys and their objectives see Norris et al. (2013). Recently, an all sky survey ( $-55^\circ$  to  $+90^\circ$ ) is being done at 150 MHz using the Giant Metrewave Radio Telescope (TGSS@ncra.tifr.res.in).

The aim of all radio surveys is to provide information about the radio sources in the sky. In the next section, the various types of extragalactic radio sources and their properties are discussed.

# 1. INTRODUCTION

---

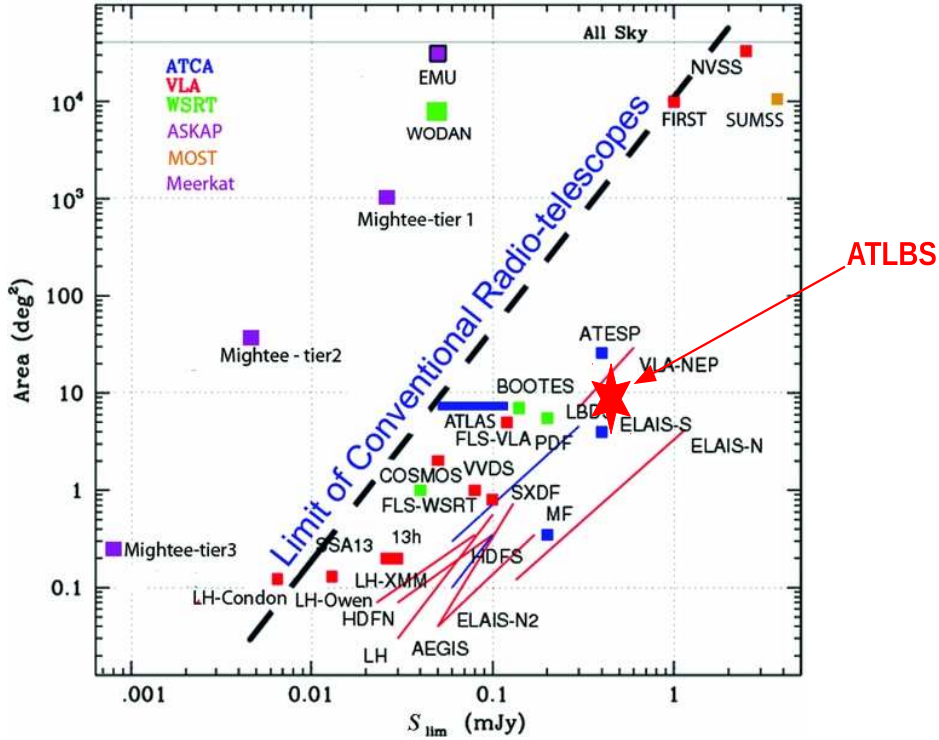


Figure 1.1: A depiction of current and planned deep surveys, in limiting flux density- survey area plane. The figure is taken from Norris et al. (2013) (Fig. 1) and suitably modified to depict ATLBS survey.

## 1.2 Extragalactic Radio Sources

Extragalactic radio sources are the focus of this thesis. These may be divided into two main categories separated by the mechanisms which power them. The radio sources above a few mJy are dominated by radio galaxies (and quasars), which are

powered by the process of accretion on to supermassive black holes residing in the center of their ‘host’ galaxies. Such sources are said to be powered by an ‘active galactic nucleus’ (AGN), also referred to as ‘central engine’. Radio galaxies are almost always seen to be associated with elliptical galaxies at low redshift. On the other hand, in most of the fainter radio sources the radio emission is a result of non-nuclear activity, such as star formation. These radio sources are most often hosted by spiral/irregular starburst galaxies. Each category has been discussed in some detail below; however, it is not a complete review of the subject in any sense.

### 1.2.1 Radio Galaxies

Cygnus A (Fig. 1.2) is one of the very first radio galaxies to be observed (Hey et al., 1946) and in many aspects the prototype of radio galaxy, having been studied in more detail due to its proximity (approx. 170 Mpc distant from the Milky Way). Interferometer observations showed strong oscillations in the intensity of radio radiation received from the source, leading observers to conclude that the radiation originated from a small number of discrete components. The argument that the period of variation might be used to determine the physical size of the radiating object was used by Ryle (1949), who estimated it as  $R = c\Delta t$  (where  $\Delta t = 20$  sec is the period of the oscillations in the intensity for Cygnus A) with  $R = 10^{12}$  cm. Based on the estimates for size, Cygnus A and other radio sources were thought to be ‘radio stars’ emitting most of their radiation in radio waves and being difficult to observe in optical wavebands. Accurate positions of radio sources were not available for some time due to the poor resolution of radio tele-

## 1. INTRODUCTION

---

scopes. Following the accurate position estimation by F.G. Smith, the optical counterpart of Cygnus A was observed by Baade & Minkowski (1954) (also earlier by Mills & Thomas (1951)), though the radio source position was not known well enough to make an unambiguous identification of the optical counterpart) as a galaxy (or an ‘extragalactic nebula’, as it was then called) in a cluster of galaxies, with the redshift of the emission lines in the spectrum establishing that it was outside the Galaxy. Subsequent measurements of the spectra of optical counterparts of radio sources established that most of these showed similar emission lines (Schmidt, 1965)) and that these were associated with galaxies. With these findings, the term ‘radio galaxy’ gradually replaced the term ‘radio star’.

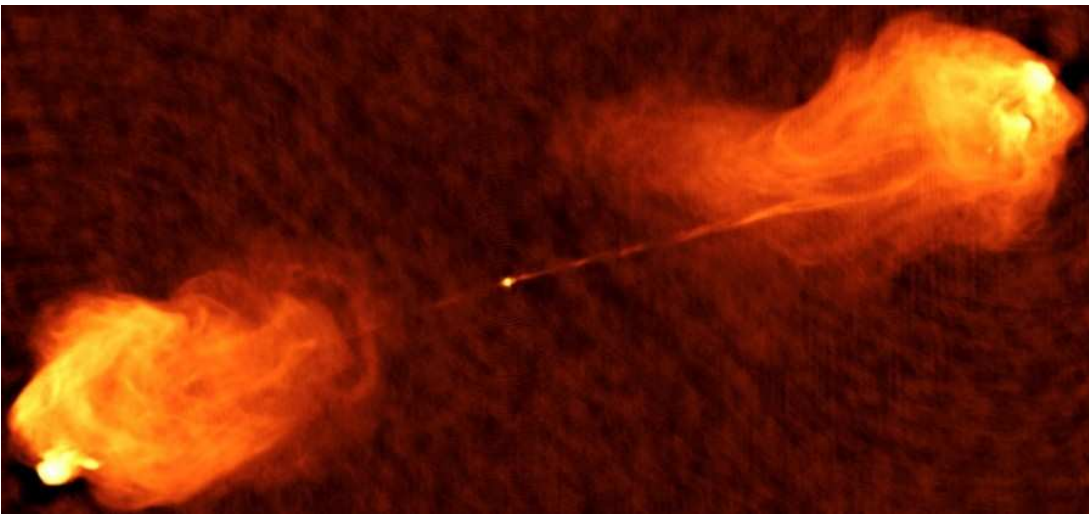


Figure 1.2: Radio Image of Cygnus A (5 GHz). Image courtesy of NRAO/AUI.

With improved radio telescopes, the studies of radio structures as well as the physics, especially the mechanisms powering these sources, progressed. The structure of Cygnus A was examined by Jennison & Das Gupta (1953) who found it to be composed of *two* components with the position of the optical counterpart

in between the pair of components. Subsequently it was found that many radio sources were composed of two components (Maltby & Moffet, 1962). The initial hypothesis of the radio sources being generated through a collision of galaxies (Baade & Minkowski, 1954) (supported by a double-nucleus morphology of Cygnus A) was soon questioned (Shklovskii, 1961). The hypothesis that the radio galaxies have their origins in events happening at the nuclei of the host galaxy was suggested by the morphology of the radio sources, which had two components on the two sides of the associated optical galaxy (as well as ‘triple sources’, with a third component coincident with the position of the optical galaxy itself). Optical observations that showed evidence of violent activity in nuclei of galaxies including presence of broad emission lines and variability in the flux were also suggestive of origins for the radio source in the nucleus of the host radio galaxy.

The radiative process by which the radio emission was being generated is suggested quite early (Alfvén & Herlofson, 1950) as synchrotron emission, produced by relativistic particles in magnetic fields. The magnetic fields associated with the radio sources were detected through the polarization of the radiation. The mechanism through which a population of relativistic particles was generated and the energy deposited at enormous distances from the galaxy was then the matter of debate. Though competing mechanisms have been proposed (the ‘slingshot model’ (Valtonen, 1977)) in which the energy transport is through a pair of supermassive black holes), currently the accepted paradigm for the mechanism of creation of double radio sources is the one first presented by Blandford & Rees (1974), which is also known as the ‘twin exhaust’ model. In this model, the energy generated at the nucleus is conveyed via two ‘exhausts’ or channels in opposite

## 1. INTRODUCTION

---

directions through which plasma is collimated into two supersonic beams of relativistic matter. Thus, the mechanism through which the double radio sources are formed is as follows. The energy is initially generated in the nucleus of the (optical) galaxy through accretion onto the supermassive black hole at the nucleus. The energy is then transported outwards through collimated beams of relativistic plasma which carry the energy as bulk motion. At the location where these beams or jets encounter the ambient medium, a shock front is formed. Particles at the jet are accelerated and thus the energy is transferred through the bulk motion of the jet to random energy of the accelerated particles. These highly relativistic particles, which are traveling in the pervading magnetic field, thus are responsible for generating the synchrotron radiation. For a detailed description of the physics of radio galaxies see Begelman et al. (1984).

Since radio galaxies span a large range in luminosity and also exhibit a variety in their morphologies as well as other properties, sample studies of sources grouped in physical characteristics also yield important and complementary information towards understanding the radio galaxy phenomenon besides studies of individual sources.

An important study in the classification of radio sources was by Fanaroff & Riley (1974). Fanaroff and Riley studied radio galaxies from the 3CR (revised third Cambridge survey), a subsample of which consisted of radio galaxies that clearly were resolved into two or more components. These sources were classified into two types by the ratio of the distance between the brightest points on the opposite sides of the host galaxy to the total extent of the source as measured from

## 1.2 Extragalactic Radio Sources

---

the lowest contour; Class I consisting of radio galaxies for which the ratio was less than 0.5 and Class II for which the ratio was larger than 0.5. Though this was a classification scheme based solely on morphological basis, it was found that there existed a ‘sharp division in luminosity between the two classes’. The sources in Class I were found to have a power below  $2 \times 10^{25} \text{ W Hz}^{-1} \text{ sr}^{-1}$  at 178 MHz, and the sources in Class II were above this power. This classification therefore appears to be fundamentally related not only to the morphology of the radio sources but also the underlying mechanisms of energy generation and/or the dynamics of the radio sources. The radio galaxies in the second class (henceforth referred to as FRII sources), are more powerful than the radio sources in the first class (FRI sources henceforth) and also show presence of hotspots, which are bright regions at the extremities of the radio source. The ‘core’ region (corresponding to the host galaxy) might not be very bright in comparison to the radio emission from the hotspots. The FRI radio sources, in comparison, do not show the presence of hotspots. The jets, which are more prominent in the FRI sources, tend to instead end in ‘lobes’ of emission lacking hotspots (lobed-FRIs) or in ‘plumes’ (naked-jet FRIs). The brightness distribution of the FRI sources therefore drops off away from the core. In fact the FRI sources also include the so-called Wide Angle Tailed (WAT) and Head-Tailed (HT) sources. The WAT and HT sources favor galaxy cluster environments and may in fact be used to detect clusters of galaxies at high redshifts.

With subsequent studies of the distribution of radio galaxies in the radio-optical plane (defined by the radio power and absolute optical magnitude) this simple picture started to change. The initial goal of these investigations was

## 1. INTRODUCTION

---

to construct a ‘radio H-R diagram’ (Owen and Ledlow, 1994). Various studies (Owen & Laing (1989), Owen & Ledlow (1994), Owen et al. (1996)) found that the radio dividing power was a function of the optical luminosity of the host galaxy, with the radio dividing power increasing as  $P \propto L_{opt}^{1.8}$  (Owen et al., 1996). This was interpreted in terms of a larger power being needed for radio sources to form an FRII structure in the environments of brighter (and thus denser) host galaxies. The two FR classes were found to be well separated by this modified dividing radio power at any given optical host luminosity, with only negligible overlap between the two populations (Owen et al., 1996). The modeling of radio source dynamics by Bicknell (1995) and Gopal-Krishna & Wiita (2001) among others reproduces these observations with varying degrees of success.

More recent studies (Lin et al. (2010), Best (2009), Wing & Blanton (2012)) have found that there is considerable overlap between the two radio populations in the radio-optical plane. The comparison of FRI/II populations in the overlap region by Best (2009) showed that 20% of the FRII sources below the Owen-Ledlow threshold have radio sizes smaller than 40 kpc. This agrees with the findings by Owen et al. (1996) that the FRII radio galaxies below the threshold appear to be confined inside the host galaxy. Such galaxies, though having FRII type radio structure, are likely to evolve into FRI sources due to interactions with the environment and/or the jet being weak (Kaiser & Best (2007), Kawakatu et al. (2009)). For a recent review, see Saripalli (2012).

Thus radio galaxies, which dominate the radio source population above few mJy, show a remarkable variety in morphologies and a large range in output in

the form of radio emission. These sources, while being the more powerful variety, are not the only population of sources and in the next part of this chapter the population of faint radio sources is discussed.

### 1.2.2 Star Forming Galaxies and Faint Radio Sources

Apart from the radio galaxies discussed above there exists another major population of extragalactic radio sources that has radio emission fueled not by AGNs but through the process of star formation. The existence of such a population was known through observations of faint radio sources (Mitchell & Condon, 1985) rather late as compared to the more powerful radio galaxies. The star-forming galaxies were invoked to account for the number density of faint radio sources, especially in the sub-milliJansky flux density regime.

The range of radio luminosity occupied by star forming galaxies is approximately from  $10^{18}$  to  $10^{24}$  W Hz<sup>-1</sup>. The radio emission from starburst galaxies is due to 1) free-free emission in HII regions which are ionized by massive, young stars and 2) synchrotron emission from cosmic-ray electrons in the body of the galaxy, which have been shock-accelerated in the supernova remnants of massive stars. The lifetime of massive stars, which is less than  $3 \times 10^7$  years, and the lifetime of the synchrotron-emitting particles in supernova remnants, which is less than  $10^8$  years, means that the radio emission from these galaxies is a very good extinction-free indicator of *recent* star formation (for a review of radio emission from these galaxies, see Condon (1992)). Thus, the radio emission from these

## 1. INTRODUCTION

---

galaxies may be an important probe of the cosmological evolution of star-forming processes.

As discussed in Section 1.1, deep radio surveys are useful in detecting these faint radio sources. With increasing sensitivity and thus lower limiting flux densities the population of star-forming galaxies and, in general, the faint radio source population has been studied with great detail in recent years. In contrast to the earlier view that the faint radio source excess is formed by the population of star-forming galaxies, recent work by Seymour et al. (2008) and Smolčić et al. (2008) suggest that radio-quiet AGNs may form a large proportion of faint sources. However, the exact composition of the faint radio source population has not yet been conclusively determined.

Apart from the different categories of extragalactic radio sources mentioned above, the radio sky also consists of a background that has not been resolved into component sources. This background, called the Cosmic Radio Background (CRB), has been the subject of recent studies. Different studies have tried to estimate the contribution of different source populations to the CRB. For example, Ponente et al. (2011) estimate the contribution of star-forming galaxies to the CRB. Recent work by Fixsen et al. (2011) has estimated the temperature of the CRB over a range of frequencies (3, 8, 10, 30 and 90 GHz) and have found that the CRB brightness spectrum (after subtraction of Cosmic Microwave Background and the Galaxy Foreground) is well fit by a power law with an index of  $-2.599 \pm 0.036$  from 22 MHz to 10 GHz (given by the equation :  $T = 24.1 \pm 2.1(K) (\nu/\nu_0)^{2.599 \pm 0.036}$ ). This is 5-6 times more than the expected

contribution from the currently known radio source populations, which implies that another radio source population, currently unknown, may exist. The work by Condon et al. (2012) has tried to resolve the radio background and arrived at the conclusion that the background must be very smooth and that any hidden population of sources, which may give rise to the radio background, is too numerous to be associated with galaxies. For a possible explanation of the CRB excess based on the estimation of the Galactic emission components see Subrahmanyan & Cowsik (2013).

### 1.3 Motivation for the thesis work

From the above discussion, it is clear that the extragalactic radio source population forms one of the key pieces in our understanding of the physics of cosmic evolution of galaxies and active galactic nuclei on scales as diverse as hundreds of kiloparsecs to a parsec. Since the evolution of extragalactic radio sources may occur over large timescales, it is necessary to observe as large number of radio sources as possible, to study them in a statistical sense. Further, to study the evolution of the radio source population with cosmic epoch it is necessary to have sensitive observations of the radio sky, which allow probing of the faint radio sources to high redshifts. Both these constraints require surveys of the radio sky which have good sensitivity and also sample a large region of the sky.

However, only radio observations of the extragalactic radio sources may not provide the information regarding the interactions taking place between the ra-

## 1. INTRODUCTION

---

radio sources and their environments, which are essential to correctly assess the co-evolution of the galaxies and extragalactic radio sources; in particular, the effects of the galactic and extragalactic environs on radio sources and also the influence of the radio sources on their environs. Observations in optical, x-ray and infrared bands typically provide information regarding the host galaxies of extragalactic radio sources as well as their large scale environments characterized by neighbouring galaxies and intragalactic/intracluster gas. Therefore, the cosmic extragalactic radio population needs to be examined via radio surveys with good sensitivity and adequate surface brightness sensitivity to image the large angular/spatial extents, complemented with observations in other wavebands. In fact, a common property of the radio surveys described in Section. 1.1 is the coverage of the survey area in other wavebands, through large scale optical surveys such as SDSS to deep observations of small regions by the Hubble Space Telescope.

Australia Telescope Low Brightness Survey (ATLBS), is such a survey. A sensitive interferometric radio survey at 1.4 GHz, it is a moderately wide-field as well as fairly deep ( $\sim 0.4$  mJy) survey, combining the best of both worlds. Thus, using the ATLBS survey, it is possible to study populations of both powerful and faint radio sources. The primary motivation behind the ATLBS survey was to image diffuse radio sources to high redshifts and to estimate the evolution in extended radio sources with cosmic epoch. The faint radio sources targeted by the ATLBS survey may be sources with low luminosity radio sources at moderate redshifts, such as star-forming galaxies or radio-quiet AGNs, or high luminosity radio galaxies or quasars at high redshifts. The ATLBS survey is complemented by broadband optical observations covering the same region of the sky and pro-

viding information on the host galaxies of the radio sources in ATLBS and their optical environments.

In this thesis, different studies of extragalactic radio sources have been done using the ATLBS radio and optical observations. The sensitivity of ATLBS survey allows an investigation of sub-mJy radio source populations. The high resolution provides structural information on extended emission associated with radio sources which, along with the optical observations, enables studies of the connection of radio sources types and morphological asymmetries with their environments characterized by galaxies, which may in turn be associated with the ambient gaseous density. Together, the studies described herein provide important information regarding extragalactic radio source populations and the cosmic evolution of radio sources and their environments.

## 1.4 Summary

In summary, the following points may be noted:

- Radio surveys are essential in examining the populations of radio sources in the sky; different types of radio surveys give complementary information on the radio sky.
- Wide-field radio surveys provide large sky coverage and make statistical and cosmological studies of radio sources possible.
- Deep radio surveys probe the faint radio source population and give information about the cosmological evolution of radio sources.

## 1. INTRODUCTION

---

- Extended extragalactic radio sources, made up of radio galaxies, possess a large range in both morphology and radio power. In both these characteristics their environment may play a significant causative role.
- Faint radio sources, which are associated with starburst and star-forming galaxies, are a useful probe of the cosmic star-formation history.

The layout of the thesis is as follows. The next chapter describes the details of the radio observations and imaging. Chapter 3 similarly describes the optical observations and imaging for the optical data taken for the sky region covered by the radio observations. Chapter 4 presents the source catalog from the ATLBS survey and source counts estimated therefrom. Chapter 5 focuses on the optical environment of extended radio sources and their quantification. Finally, in Chapter 6 the conclusions of this thesis are presented.

## Radio Observations and Imaging

To characterize the cosmic evolution of radio sources and their properties, observations and imaging of faint radio sources is essential, as explained in Chapter 1. The Australia Telescope Low Brightness Survey (ATLBS), which has been used in the studies presented in this thesis, has been designed specifically to image diffuse radio emission to relatively high redshifts ( $z \sim 1 - 1.5$ ). Therefore, obtaining good surface brightness sensitivity has been a prime objective in planning the radio observations and in imaging the data obtained from these observations. In this chapter, the details of the radio observations and imaging process are presented.

The primary motivation behind the radio observations forming the ATLBS survey was to image diffuse emission which may be missed in interferometric surveys in absence of adequate uv plane coverage. However, diffuse radio sources, especially FRI sources, form the bulk of the extragalactic radio sources. There-

## 2. RADIO OBSERVATIONS AND IMAGING

---

fore, these sources are of critical importance in estimating interactions between radio sources and their surroundings; especially in processes such as radio-mode feedback. It is known that FRI sources, while not evolving as strongly as FRII sources, show signs of evolution with cosmic epoch. To estimate this evolution it is necessary to image the (already) faint, diffuse FRI sources to high redshift. On the other hand, the population of faint sources in the local universe needs to be accurately characterized since current observations show a large degree of uncertainty in the nature (star-forming galaxies, radio-quiet AGNs and/or low power radio galaxies) and numbers of this population. Other types of highly diffuse radio sources like haloes or relics, which are generally associated with clusters of galaxies, also require good surface brightness sensitivity to be observed. To summarize, good surface brightness sensitivity is highly desirable in radio surveys seeking to examine cosmic populations of radio surveys. Many of the sources mentioned above are best observed at low frequencies due to their high spectral index. However, substantially worse radio frequency interference at low frequencies suggests that moderately higher frequencies may in some cases be preferred for a survey.

The above constraints therefore require the survey to be carried out with a nearly full synthesized aperture, at moderately high frequencies and targeting a sky region devoid of bright sources. These requirements have been fulfilled in ATLAS survey, which has excellent uv coverage especially at short spacings, is observed at 1.4 GHz and images a region which is empty of strong radio sources. These requirements have also prompted the use of Australia Telescope Compact Array for the survey. Below is a short description of the Australia Telescope

Compact Array.

### 2.1 Australia Telescope Compact Array

The radio observations were made with the Australia Telescope Compact Array (ATCA). ATCA is a part of Australia Telescope National Facility (ATNF), operated by the Commonwealth Scientific and Industrial Research Organization. The array is located in Narrabri, NSW, Australia. ATCA was chosen based on several considerations based on the requirements of the survey. Since a primary aim of the survey was to have observations which allowed for making radio images of excellent surface brightness, which requires complete uv coverage (without any gaps), a linear array such as ATCA was thought to be better than two-dimensional arrays such as the VLA or GMRT. These other arrays that have 3D configurations may give excellent uv coverage that are, however, not necessarily *complete*.



Figure 2.1: Antennas of the ATCA interferometer (Image courtesy CSIRO, Australia).

## 2. RADIO OBSERVATIONS AND IMAGING

---

ATCA consists of 6 antennas each of 22 meters. Five of these are movable on a railway track (see Fig. 2.1). The railway track has two segments, one oriented east-west and the other north-south, though in the observations carried out for the ATLAS survey, only the east-west track has been used. The east-west segment is 3 km in length, whereas the north-south segment spans 214 meters. The sixth antenna is fixed and is located 3 km west of the western end of the east-west track. This gives a maximum baseline for the array at 6.0 kilometers. The minimum antenna spacing for the array is 30.64 meters.

The antennas of the ATCA are of Cassegrain design, on alt-azimuth mounts. The Cassegrain design means that the receivers for an antenna are located in a feed cabin at the center of the main reflector. The secondary reflector is located at the prime focus of the antenna. The main reflector and secondary reflector of the antenna are shaped; designed to maximize the gain to antenna noise ratio for the operating frequencies. The surface of the movable antennas are made of solid panels, which allows observations to be made to high frequencies (up to 116 GHz). The sixth antenna has the inner 15.3 meters made of solid panels and the rest made of perforated panels, which allow observations at frequencies up to 50 GHz. ATCA is capable of observations in a wide range in frequencies, upwards of L band (1.2 - 1.78 GHz). The feedhorns and receivers are located on a rotating turret, which translates the feed corresponding to the observing frequency into the optic axis. ATCA has feeds of dual linear polarization and hence is able to measure two orthogonal polarizations simultaneously.

ATCA offers a variety of configurations for different principal arrays (four

configurations per principal array). For the observations described in this chapter, the configurations of the 750 m and 6 km arrays have been used. The radio observations are described in detail in the next section.

## 2.2 Observations

The radio observations which form the ATLAS survey were made with different array configurations of the ATCA. The observations were made in the 20 cm band, with a center frequency of 1388 MHz. The observations were made in two sub-bands at central frequencies of 1344 MHz and 1432 MHz, with a bandwidth of 128 MHz in each sub-band. Each sub-band was covered by 16 independent frequency channels, but only the multi-channel continuum visibilities in the 13 central channels were used. This division of the total bandwidth into individual channels is useful in reducing the effects of bandwidth smearing (chromatic aberration) as well as possible imaging errors due to spectral index variations between different sources. These observations recorded visibilities in full polarization mode.

The ATLAS survey covers two regions in the southern sky. These regions are designated as ‘A’ and ‘B’ having their centers at RA:00<sup>h</sup> 35<sup>m</sup> 00<sup>s</sup>, DEC:−67° 00′ 00″ and RA:00<sup>h</sup> 59<sup>m</sup> 17<sup>s</sup>, DEC:−67° 00′ 00″ respectively (J2000.0 epoch coordinates). The two regions were specifically selected to be devoid of strong radio sources, low Galactic foreground emission, and at an optimum latitude that allowed for good visibility coverage for radio observations with the ATCA (at the minimum

## 2. RADIO OBSERVATIONS AND IMAGING

---

30 m baseline, to avoid shadowing, the observations have to be made south of  $-50^\circ$ ). Together, these regions cover an area of  $\sim 8.4$  square degrees.

Since a primary aim is to image diffuse radio emission, complete coverage at short baselines was necessary for ATLBS radio observations. The radio observations were initially made with the array configurations of 750A, 750B, 750C and 750D. These configurations provided complete u-v coverage up to 750 meters. In addition, baselines to the 6th antenna provided u-v data between 3015 meters to 5020 meters. Using these observations, radio images at relatively low resolution with beam FWHM=  $50''$  were made. The observations and imaging of this data were presented in an earlier publication (Subrahmanyam et al., 2010).

To obtain better u-v coverage up to 6 km, new observations were made with the array configurations: 6A, 6B, 6C and 6D. The plan of the observations was as follows. The two regions A and B were observed in each array for 12 hours each, which made the total duration of the observation to be 192 hours. Each of the regions was covered as a mosaic of 19 pointings, since the primary beam covers only half a degree. The mosaicing was not with sufficient overlap between adjacent pointing so as to synthesize spacings smaller than the dish diameter; therefore, structures in scales exceeding the primary beam FWHM would not be reproduced in the imaging. Each pointing was observed for 20 seconds before switching to the next pointing and the pointings were thus cycled with a period of  $19 \times 20$  seconds in an observing session of 12 hours. This strategy ensured that the uv-coverage changed minimally between data points. Additionally, up to 750 m baselines the spacings between data points did not change more than

the antenna size in one such cycle. In the next section, the imaging procedure followed for the data is described.

## 2.3 Imaging

The reduction and imaging of the data was done with the radio interferometer data reduction software MIRIAD (Sault et al., 1995).

The data was calibrated for amplitude and phase using the calibrator source PKS B2353 – 686. The absolute flux calibration was done using the calibrator sources PKS B1934 – 638. The visibility data was also examined for radio frequency interference and was removed where necessary.

The uv-data with visibilities from the configurations 6 A-D and the uv-data for the rest of the configurations were initially reduced separately and then combined in a single data set. The following were the steps taken to reduce the data. First, images were produced with the 6 km data. These images were deconvolved using the Clark CLEAN algorithm (Clark, 1980), which is faster for large images. The deconvolution was carried out till the first negative components were encountered. This ensures that the deconvolution does not pick up spurious flux as clean components. The ‘loop gain’ of the minor cycle of the deconvolution was kept at 0.0005 and the number of iterations in the minor cycle was kept to 500000. The deconvolved components obtained were used as a model for phase self calibration of the data.

## 2. RADIO OBSERVATIONS AND IMAGING

---

Prior to mosaic imaging of all the pointings, the sources in the primary beam sidelobes needed to be removed from the visibility domain in the individual pointings. This issue arises because of the alt-azimuth mounts of the telescope along with the blockage due to the sub-reflector support legs: the quadrupod. During the course of the observations, the beam of the antenna rotates with respect to the pointing center. While the sources inside the primary beam main lobe move azimuthally through a more or less circularly symmetric main lobe, those in the sidelobes have a time-dependent beam structure modulating them, due to azimuthal beam structure outside the main lobe. Thus the primary beam sidelobe source visibilities are modulated in a time-variable manner and visibilities of even unresolved sources in sidelobes may not be constant. Therefore the image plane PSF of sources outside the main lobe will differ from the PSF of sources within the main lobe. Moreover, the PSF of sources outside the main lobe will be position dependent (see Fig. 2.2 for the sidelobe sources in image domain). To isolate the sources imaged with primary beam main lobe as opposed to those in the sidelobes (which may not be deconvolved properly), the following procedure was followed. After a phase self-calibration iteration, the deconvolved components of sources exclusively within the primary beam main lobe were selected by masking the regions outside the primary beam main lobe in the images. Visibilities corresponding to the sources from primary beam main lobe were subtracted from the data and the residual visibilities were imaged to model the sources outside the primary beam sidelobes. The model was allowed to include both positive and negative intensity components. Visibility domain subtraction of this model provided a dataset free of sidelobe sources and to this were added back the visibilities of sources inside the primary beam main lobe. Next, the visibilities from

the array configurations of 750 m length were reduced in a similar way to get visibilities referring only to the sources within the primary beam main lobe (see Fig. 2.3 for the deconvolved image containing only the primary beam main lobe sources). It may be noted that a somewhat different approach has been adopted for eliminating the effects of sources at large offsets compared to ‘Peeling’. The reason is that there are numerous sources in the first sidelobe, due to the rather uniform illumination in the design of the ATCA antenna optics and, therefore, these sources need to be removed jointly. The Peeling self-calibration solution will be different for different sources in the sidelobes.

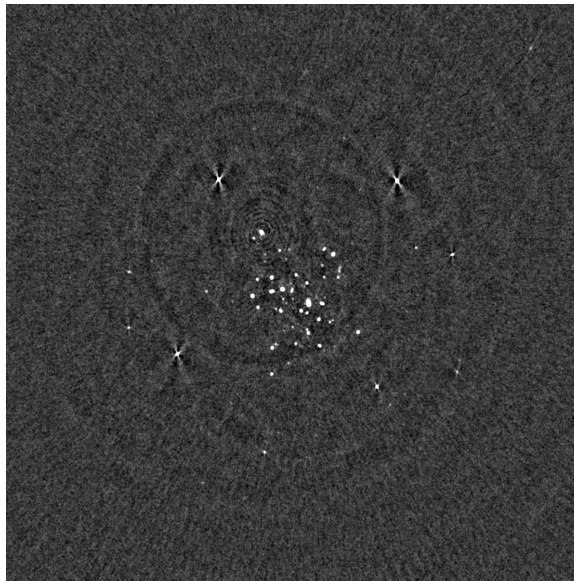


Figure 2.2: Sample of a single radio pointing (with 750 m data) without the removal of sources in the primary beam sidelobes and prior to deconvolution. The unusual point spread function for the sources in the sidelobes may be seen in the figure.

## 2. RADIO OBSERVATIONS AND IMAGING

---

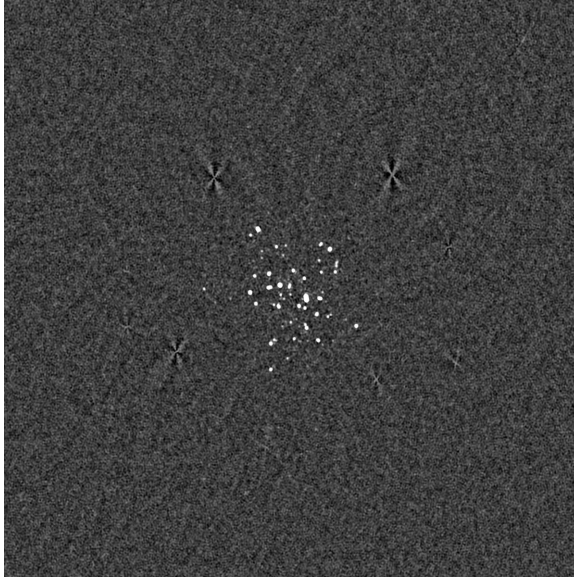


Figure 2.3: The same single radio pointing (with 750 m data) after the removal of the sources in the primary beam sidelobes and deconvolution.

The visibility data, thus free from sources in the primary beam sidelobes, was then further imaged to obtain the final radio images. The imaging at this stage consisted of use of multiple techniques such as self calibration (see Pearson & Readhead (1984), for a review) and multi-frequency deconvolution to ensure high fidelity final images. In the final imaging cycle, multiple iterations of self calibration (initially phase only, later amplitude) and multi-frequency deconvolution were used. The self-calibration corrects for the calibration errors left over after the normal calibration by solving jointly for complex antenna gains along with image components using the available visibilities, thus giving superior calibration. The multi-frequency deconvolution solves simultaneously for image intensities and spectral indices at every image pixel, and takes into account the fact that the primary beam gain is a function of the observing frequency and may

vary. It also accounts for the spectral index which varies among the sources in the images.

The imaging was done with large sidelobe suppression area to obtain a good synthesized beam. Initial self calibration iterations were of phase-only type. The multi-frequency deconvolution described in Sault & Wieringa (1994) was used to get the clean components from self-calibrated data. Because the  $u,v$ -coverage was not complete in the 750-6000 m range, deconvolution was assisted by selecting regions where higher probability of radio emission was present and masking the rest of the image. This was done by first smoothing the image to detect most of the diffuse emission and masking regions below  $4.5 \sigma$  in the smoothed image. This process was repeated, iteratively, along with phase and amplitude self calibration. The amplitude self-calibration cycles were performed which continually renormalizing the mean antenna gains so that the overall flux density scale was preserved. The flux density thresholds for masking were varied in successive cycles to better capture diffuse emission in successively improving images. Similarly, the solution intervals for the successive iterations varied from 15 to 5 minutes.

One step in the processing was amplitude self-calibration separately for the two frequency bands without gain renormalization—this is equivalent to amplitude calibration based on the mean spectral index for the radio sources in the image. This step was done with a full observing session as the solution interval, to allow for a constant relative gain adjustment in the two bands over the entire duration of the observation.

## 2. RADIO OBSERVATIONS AND IMAGING

---

In the final step, the images of individual pointings were regridded and stitched together in a linear mosaic to obtain the combined mosaic image of region A and B separately. The images were added linearly with weights computed to maintain the rms image noise in the final mosaic image constant over the sky – the linear mosaic operation also yielded a gain image that defined the source attenuation over the mosaic image.

### 2.3.1 Clean Bias

A possible effect, arising from the deconvolution process used in imaging the radio data is that of ‘clean bias’ (Condon et al., 1998). The clean bias comes about if the uv coverage of the data used for imaging is sparse (i.e. as with snapshot observations) and the deconvolution process is carried out to low flux densities. In such cases the sidelobes of the synthesized beam, which may be prominent, can be mistaken for clean components and picked up during the deconvolution process. This effectively redistributes the flux density of the ‘real’ radio source to spurious components.

In the case of ATLBS survey, the data used has excellent uv coverage which ensures that this effect is not prominent. However, to estimate the magnitude of this effect, simulations have been carried out using ATLBS data. In these simulations, additional point sources were added to the uv data and imaged. These sources were added with flux densities corresponding to 3, 3.5, 4, 4.5, 5, and 5.5 times the rms noise in the images. The flux densities of these sources was then

contrasted with the input flux densities to estimate the flux density being lost to the clean bias. It was found that the flux densities measured do not show any systematic loss even at the lowest flux densities. It can therefore be assumed that the clean bias does not affect the ATLBS data significantly.

## 2.4 Final Mosaic Images

The sky area covered by these regions is depicted in Fig. 2.4. Sample sub-images of these high resolution images are presented in Fig. 2.5 and Fig. 2.6. To better appreciate the difference between the high and the earlier low resolution images (Subrahmanyam et al., 2010), a sky region has been presented in low and high resolutions in Fig. 2.7 and Fig. 2.8, respectively. The linear combination of pointings was done with a weighting that maintained rms noise in the images nearly uniform; this value is  $72 \mu\text{Jy beam}^{-1}$ . Over the 8.42 square degrees sky area where the attenuation in the mosaic images is less than 0.5 (and hence the rms noise in primary beam corrected images does not exceed the above central by more than a factor of two) there are no image errors apparent above the image thermal noise. This exceptional quality in the wide-field images makes it a useful database for automated source finding and classifying algorithms as well as reliable studies of radio source properties.

In addition, the range of source morphologies makes possible the validation and development of automated source finding algorithms, which may become crucial in the analysis of data from large surveys such as LOFAR and SKA. Representative sources from the high resolution images are presented in Fig. 2.9.

## 2. RADIO OBSERVATIONS AND IMAGING

---

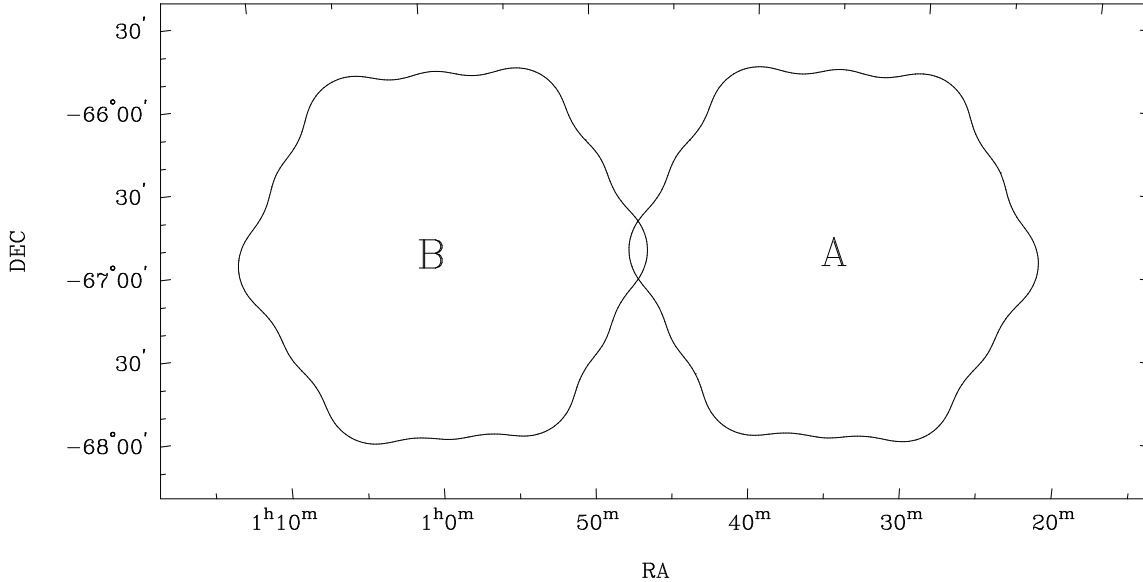


Figure 2.4: The boundaries of regions A and B are shown. Within these regions the attenuation of the sky sources is less than 0.5 in the mosaic images.

### 2.5 Summary

High-resolution radio images of the ATLBS survey regions are presented in this chapter with beam FWHM of  $6''$ . The wide field mosaic images covering  $8.42$  square degrees sky area with rms noise  $72 \mu\text{Jy beam}^{-1}$  are of exceptional quality in that there are no imaging errors or artifacts above the thermal noise over the entire field of view. The images have excellent surface brightness sensitivity - the visibility coverage is complete out to  $750 \text{ m}$  - and hence provides good representation of extended emission components associated with radio sources. The images are, therefore, an excellent resource for examining with automated algorithms for source finding, parameter fitting, and morphological classification, and as a resource for testing such algorithms that would be used on upcoming all-sky continuum surveys with the LOFAR and ASKAP. The high-resolution ATLBS images are available at the website [www.rri.res.in/ ATLBS](http://www.rri.res.in/ATLBS) as well as in

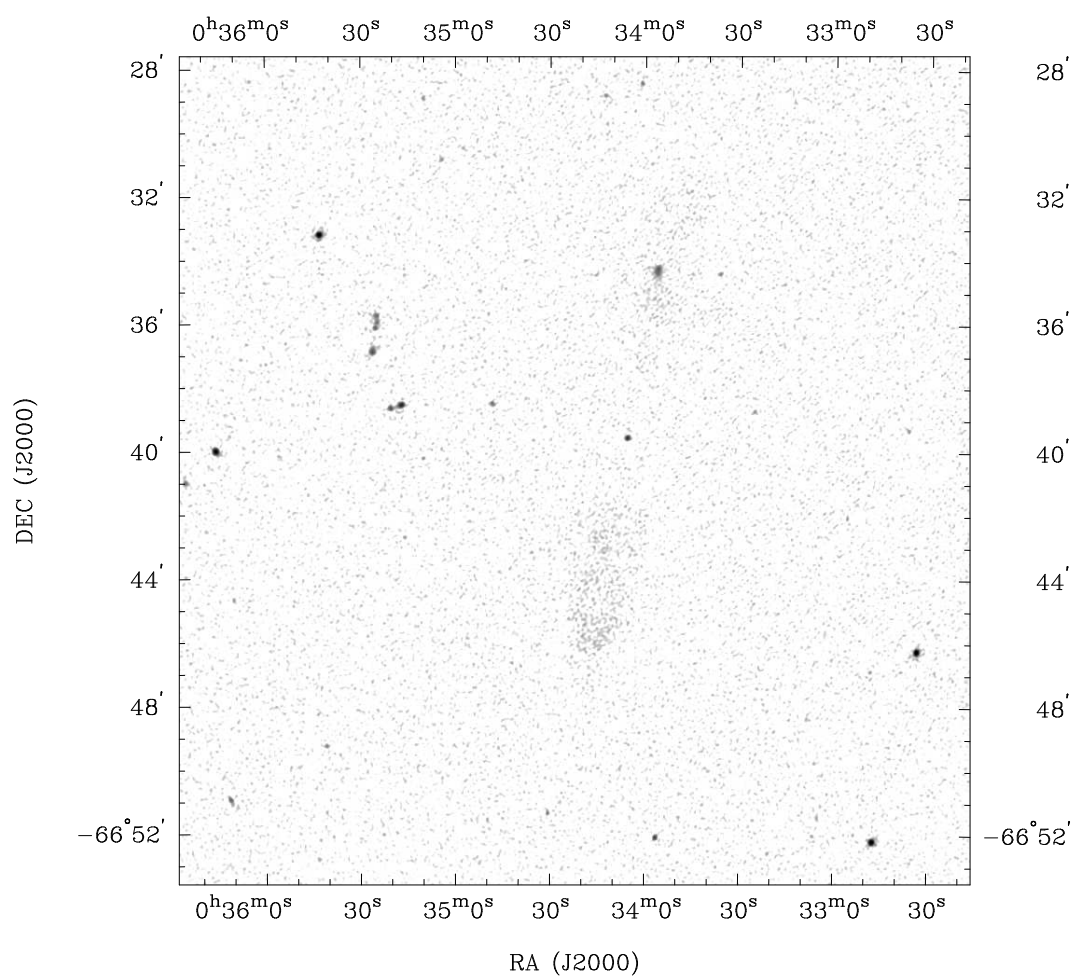


Figure 2.5: A representative region from Field A shown in greyscale. The image has beam FWHM  $6''$  and rms noise of  $72 \mu\text{Jy beam}^{-1}$ .

## 2. RADIO OBSERVATIONS AND IMAGING

---

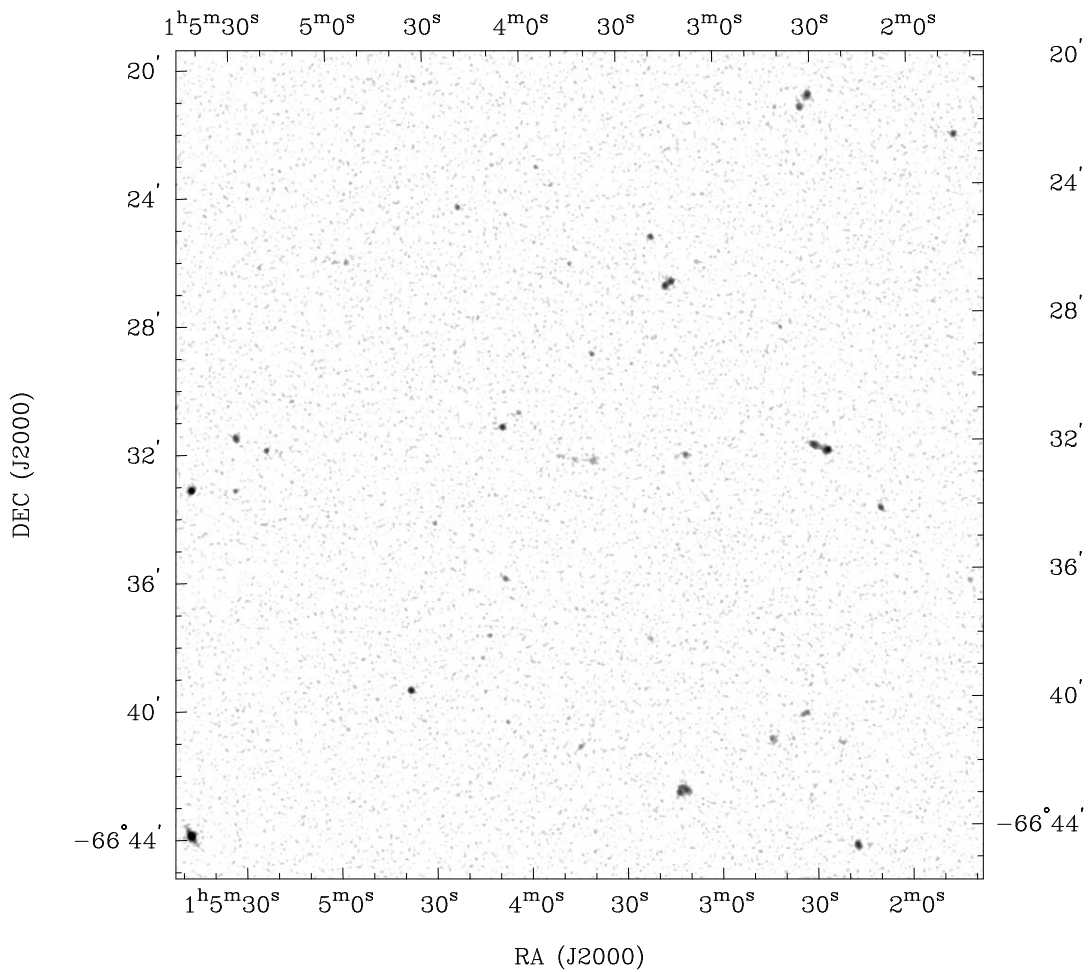


Figure 2.6: A representative region from Field B shown in greyscale. The image has beam FWHM  $6''$  and rms noise of  $72 \mu\text{Jy beam}^{-1}$ .

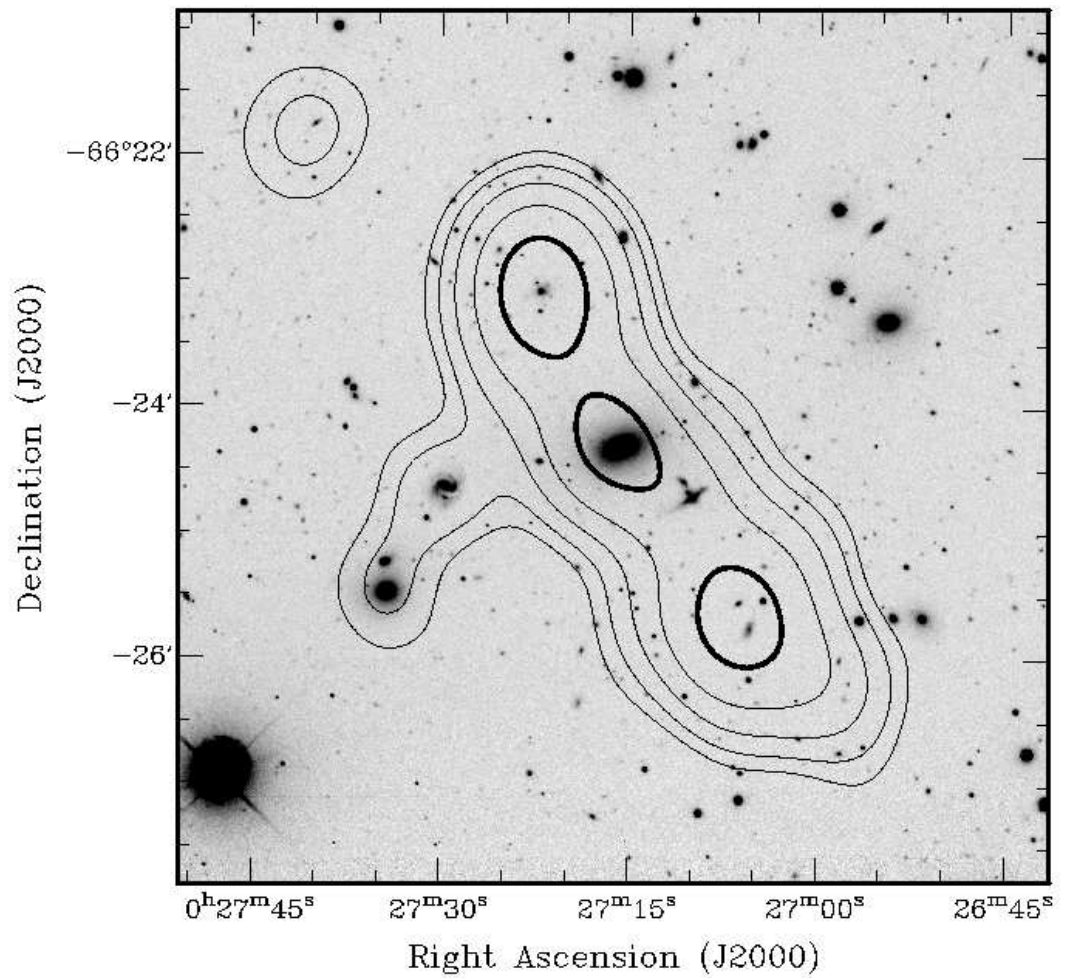


Figure 2.7: A sky region from low resolution image. The contours are selected to increase in factors of 2, starting from 0.38 mJy. The greyscale depicts the optical  $r'$  band image derived from the optical observations using the MOSAIC II imager on the CTIO 4-meter telescope (see Chapter 3 for the details of optical observations). The image reaches a depth of  $r' = 22.75$ .

## 2. RADIO OBSERVATIONS AND IMAGING

---

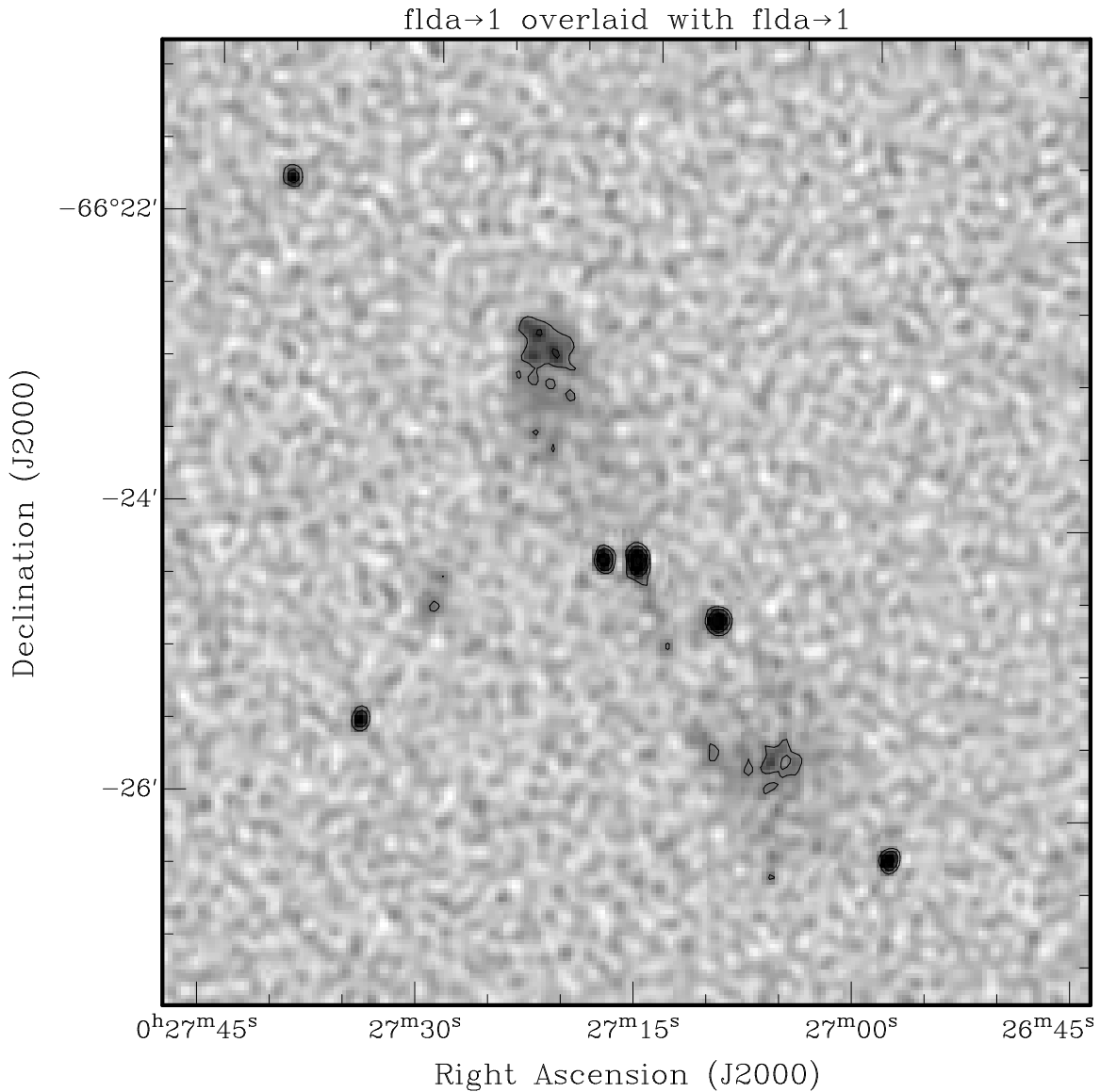


Figure 2.8: The same region as in Fig. 2.7, shown in high resolution. Note that what may be perceived as a single source at low resolution is a composite of multiple sources. For a discussion of blending-confusion issues see 4.2.2. The octave contours start from 0.28 mJy.

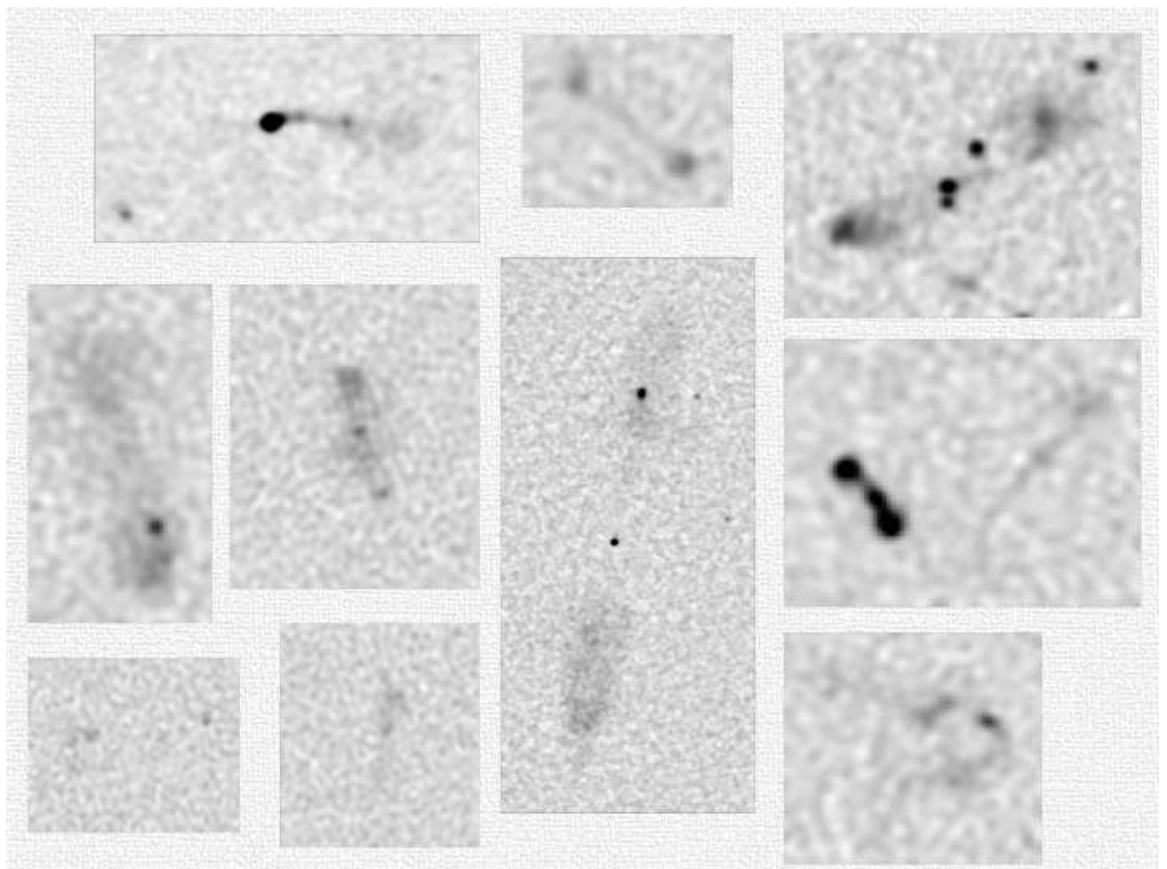


Figure 2.9: Representative radio sources from the radio images.

## 2. RADIO OBSERVATIONS AND IMAGING

---

the Appendix.

The images used in Chapter 4 to study the source counts in the transition regions for mJy to sub-mJy regions, where an upturn indicating emergence of a new population has been reported previously. An extended source sample based on these images is used in Chapter 5 to study the influence of galaxy environment on structural asymmetry in radio sources. The latter study makes use of optical images which cover region A and B described above. In the next chapter, the observing, imaging and photometry of the optical data associated with the ATLBS survey is described.

## Optical Observations and Imaging

### 3.1 Introduction

The radio observations described in Chapter 2 form the primary observations of the ATLBS survey, giving sensitive radio images of the survey regions. These radio images have been used in studies of radio sources, in source counts (Chapter 4) and environments of extended radio sources (Chapter 5). In both these studies, the accompanying optical observations have been utilized. The optical images have been used provide identification of the hosts and provide information of the galaxy environments of radio sources. In this chapter, the details of the observations, imaging and photometry of the optical data is presented.

The organization of the chapter is as follows. In the next section the CTIO 4 meter Blanco telescope, which was used for carrying out the optical observations, is described in some detail. In Section 3.3 the details of the optical observations

### 3. OPTICAL OBSERVATIONS AND IMAGING

---

are presented. In Section 3.4 the imaging of the observed data is presented. The photometry of the optical images is described separately in Section 3.5. Finally, in Section 3.6 the concluding remarks and a summary of the chapter is presented.

## 3.2 CTIO 4-meter Telescope

The optical observations of the ATLBS survey regions were carried out with the Cerro-Tololo Inter-American Observatory's 4-meter Victor Blanco Telescope (Fig 3.1), located in Chile. The telescope has a primary mirror with a collecting area of  $\sim 10 m^2$ . At the prime focus of the telescope imaging instruments are deployed. The imager which has been used for the optical observations of the ATLBS fields is the MOSAIC II imager, a mosaic of 8 SiTe CCDs (each of  $2k \times 4k$  pixels), together giving  $8192 \times 8192$  pixels. With a field of view or image size of  $37' \times 37'$ , it gives a pixel scale of  $0.27''$ . The CCDs in the mosaic are arranged in two rows of four CCDs each and each CCD is further divided into two parts (due to using two different amplifiers for readout process). The sky coverage provided by the CCDs is not complete however; there are gaps present between two amplifiers of each CCD, between each pair of CCDs as well as a gap between the two rows of the CCDs.

## 3.3 Observations

The optical observations were done to cover the two widefield ATLBS survey regions (A and B). The observations were done in three bands :  $g'$ ,  $r'$  and  $z'$ . The  $g'$  filter is centered at  $4813 \text{ \AA}$  with a width of  $1537 \text{ \AA}$ . The  $r'$  band filter is centered



Figure 3.1: The CTIO 4-meter Blanco Telescope

at  $6287 \text{ \AA}$  with a width of  $1467 \text{ \AA}$  and has a very sharp cutoff at both ends. The  $z'$  filter is centered at  $9400 \text{ \AA}$  with a width of  $2000 \text{ \AA}$  (each of these was covered by 14 pointings).

To sample the gaps between the CCDs of the mosaic as well as avoid imaging errors due to spurious sources such as cosmic rays and satellite trails, observations at each pointing was made in a set of dithers (optical images slightly offset from the pointing centers). Standard dithering strategy was used, which was constrained by the number of nights available for observation. In total 4 nights were available for observation. It was assumed that approximately 9 hours would be available for observations per night. Of this time, 2 hours were set aside for focusing and taking standard images (without any dithers). The readout time per dither was 100 seconds. Due to this  $r'$  and  $z'$  bands were observed in 5-dither mode and  $g'$  band was observed in 3-dither mode. Since only the  $r'$  band has been used in the work carried out for this thesis, only the imaging of the  $r'$  band is described herein.

### 3. OPTICAL OBSERVATIONS AND IMAGING

---

Each of the  $r'$  band images were observed with five dithers per pointing. Apart from the central dither, where the image center coincided with pointing center, the remaining four dithers were offset from the central dither by  $1'$  in East, West, North and South directions. Each of the dithers was observed for 100 seconds. Each of the dithers was processed separately before stacking them into single images. The processing of the data as well as the imaging is described in the next section.

#### 3.4 Data Reduction and Imaging

The reduction of the optical data was carried out with the Image Reduction and Analysis Facility (IRAF) software. Because the optical data was obtained using a mosaic of CCDs, uncommon issues not found in usual single-CCD observations were present in the reduction of the data. Due to this, extensive use was made of the MSCRED package of IRAF, which has been designed specifically to calibrate and image mosaic data.

The data was reduced in multiple steps. Broadly, the data was put through:

1. Calibration
2. World Coordinate System Setting
3. Stacking

Each of the steps is explained in some detail below.

### 3.4.1 Calibration

The calibration of the optical dithers is described in this section. During the observations, counts in pixels may be present even when the CCDs are not exposed to any source in the sky. This ‘bias’ needs to be removed (subtracted) from the images. In addition, there may be pixel-to-pixel response variations or image gradients present which must be removed by ‘flattening’ the images (a divisive operation). For carrying out the calibration of the images specific images or frames (bias and dome flats) were taken during the course of the observation. In the first step, each of the calibration frames was processed.

Each of the calibration images was first corrected for bias using overscan region and bias frames as well as processed for the removal of cross-talk and masking of bad pixels. The ‘overscan’ is an extended part of the image not actually exposed to the sky, but used to measure the additional counts generated in pixels. Since the pixel counts in the overscan are taken for each image/frame separately, the bias value it provides is specific to the time the image was observed. The images used in this work have an overscan region of 50 pixels. After using the overscan for subtracting bias from all the images, the images were trimmed of the overscan regions. For image-wide bias removal, specific bias frames were used. 20 such frames were available, which were combined in a ‘master’ bias frame. This ‘master bias’ frame was used for bias correction from all the frames. The cross-talk, which is the generation of spurious sources generated in one of the CCDs due to the sources in another CCD. For the MOSAIC II imager, this is a very small effect (0.1-0.2%). The cross talk correction was done with the cross talk

### 3. OPTICAL OBSERVATIONS AND IMAGING

---

correction files provided for the MOSAIC II imager by NOAO. Additionally, the known bad pixels were masked using the mask files provided by the observatory.

For the purpose of flat fielding, dome flats as well as twilight flats were obtained. The dome flats are frames in which the frames are exposed to an artificial uniformly illuminated screen. Twilight flats are frames generated by using the twilight sky as a source of uniform illumination. Among these only dome flats were used since the twilight flats were found to be unsatisfactory. The twilight frames were examined and it was found that the three twilight flats showed counts higher than 30000 on average. Since this is beyond the region of linear response of the CCDs, these were rejected. The remaining flats, while showing counts in the range 10000 - 20000 on average, were contaminated by stars, and hence also rejected. The dome flats (already processed for bias correction) were combined into a single image to use for flat fielding. This ‘master dome flat’ was used for the initial flattening of the images.

The bias correction, cross-talk correction and bad pixel masking of the dithers exposed to the sky (‘object’ frames) were carried out while also carrying out bias correction and flat-fielding using the combined bias and flat frames generated in the earlier steps. At this point, the object frames were also corrected for bleed trails, which are trails generated in pixels during the readout process due to neighboring saturated pixels that correspond to very bright objects (mostly stars). The saturated pixels were identified with the help of the saturation values recorded in the header. The bleed trails were identified using a minimum trail length of 20 pixels and a pixel value one-third of saturation value. The bleed

### 3.4 Data Reduction and Imaging

---

trails were removed by interpolating over them. The saturated pixels were also added in the bad pixel mask of each image.

After using the master dome flat, the variation in the mean image intensity level of individual CCDs was only about 8 – 10%. To further improve the flattening correction, a sky flat was also made which is an image combining all the object frames after the removal of all the objects (stars as well as galaxies). To do this object masks were first created for all the object frames. Using these the objects were removed from the frames. These frames were then combined in a Sky flat. In most of the images, the background uniformity is limited to 2 – 4%. In some cases though, it was seen that the flattening (as quantified by the spread in the mean counts of the amplifiers in a single image) did not go below 7%. This may be attributed to the presence of bright stars in the sub-fields, rather than any intrinsic response variations of the CCD pixels; the hypothesis was confirmed by visual identification of the fields of amplifiers with high counts, which reveal that these host bright star(s) in selected cases).

The flat-fielding process concludes the calibration stage of the imaging. It may be noted that fringe correction, dark current correction and pupil-ghost corrections were not applied, since these issues are either absent or negligible in the  $r'$  band images.

After calibrating the images, the next step described below is to set the world coordinate system for the images.

### 3. OPTICAL OBSERVATIONS AND IMAGING

---

#### 3.4.2 WCS Setting

In each of the images, a world coordinate system (WCS) generated at the observatory is already present and corrections to it are generally not very significant. Having the correct WCS is extremely important for stacking the separate dithers, which have to be combined with accounting for the offsets of each dither. If the WCS is incorrect then stacking may not produce the desired images and may generate artefacts in the images. This was the case with the images used in this study. Therefore, a new WCS was generated for the images, which is described below.

After initial stacking, it was found that the stacked images did not have correct coordinate systems. While testing the positional matching of the objects in the stacked  $r'$  band images with USNO A2.0 astrometric catalog, groups of objects were found, which showed positional matching worse than tens of arcseconds. Initially the cause of the problem was not clear and faint objects that may have poor positional matching or objects at the edge of the stacked image (where the image noise is higher) were suspected. However, these origins were ruled out by selecting only bright stars for positional matching and taking only central regions of the stacked images for the positional matching. In both cases, objects were present which showed large offsets. It was later established that these objects may correspond to multiple images of the same object. This was attributed to object coordinate mismatch in the dithers of a pointing, leading to multiple sources corresponding to a single real source.

The problem was solved by creating WCS from scratch prior to the stacking. For this purpose, the USNO A2.0 astrometric catalog was used. Using the coordinates of the objects from the USNO A2.0 catalog and matching them to objects in the  $r'$  band dither images, a new WCS was created with the IRAF task MSCCTPEAK. The WCS created was then applied to other exposures with the task MSCSETWCS. For fine-tuning of the WCS for each of the pointings, the task MSCCMATCH was used. This is also required due to the large size of the images, which necessitates setting the correct coordinate system for all regions of a given image. The fine correction involves two steps, the first being a coarse search for object matching (between image and the astrometric catalog used) and a second step of finer matching and centering of objects. The new WCS, thus generated, does not show the problems of the original WCS described above. The final positional matching between the  $r'$  band images and USNO A2.0 catalog shows a typical rms of  $0''.3$ .

This leaves only the final step of the imaging, which is the stacking of the dithers to produce the final images.

### 3.4.3 Stacking

The stacking was carried out by combining the WCS corrected dithers. Initially the WCS-set dithers were tangent plane projected (with the task MSCIMAGE). Interpolation using a  $\frac{\sin(x)}{x}$  form function was used when tangent plane projecting the dithers, except for bad pixels where bilinear interpolation was used for computational speed. This has resulted in artefacts in vicinity of bright, saturated

### 3. OPTICAL OBSERVATIONS AND IMAGING

---

stars, but it was found that overall bilinear interpolation works better for bad pixels.

An issue to be taken care of before the stacking was to remove intensity gradients and match intensities across the dithers of each pointing. Matching of intensities in the dithers of the same pointing is important for combining the dithers and some intensity mismatches were found despite the calibration processing. These were corrected with the tasks MSCSKYSUB and MSCIMATCH.

In a final step, separate dithers of images were combined by using averaging with sigma clipping, which rejects outliers while combining the separate dithers. This has been used to remove spurious features such as satellite trails and cosmic rays, which may affect a single dither, but not the whole dither set *at the same position*. Another effect of combining the dithers is the coverage for the gaps between the dithers. The final images, which are  $37' \times 37'$  in size are free of artefacts. In the next section the photometry of the optical images is described.

## 3.5 Photometry

The photometry of the  $r'$  band images has been carried out using IRAF as well as the Source Extractor software. IRAF has been used to carry out the initial photometry, the aim of which is to fix the photometric parameters for later use in photometric calibration. The object of the photometry is to obtain a relation between the measured counts (or instrumental magnitude) and the true magnitude of an object. The process is described below in some detail.

### 3.5.1 Standard Star Photometry

Standard star exposures have been used to derive the photometric parameters. Standard stars from the field *NGC 458 AB*<sup>1</sup> (Alvarado et al., 1995) have been used in this study. All together there are 3 standard star exposures for the first and 1 standard star exposure for the second night over which the *r'* band observations were taken. The standard star exposures cover a range in airmass. This permits fitting instrumental magnitudes to the catalog magnitudes with airmass variation taken into account, though a color term has not been used as only a single band is under consideration here. The fit is for two free parameters: an additive shift and the airmass term. 33 standard stars in total have been used to fit the relation. These stars were chosen to cover a wide range in intensity for a better estimation of the photometric parameters. The PHOT task was used to derive the instrumental magnitudes and the PHOTCAL package has been used for the fitting process. The instrumental magnitudes are obtained with aperture photometry, with an aperture of radius 8 pixels. The equation used to derive the photometric parameters is :

$$\text{Instrumental Magnitude} = \text{Catalog Magnitude} + C1 + C2 \times \text{Airmass}. \quad (3.1)$$

Here *C1* and *C2* were the free parameters of the fit. The average mismatch between the instrumental and catalog magnitudes was found to be only 0.05 magnitudes.

---

<sup>1</sup>[http://www-star.fnal.gov/Southern\\_ugriz/Old/www/NGC\\_458-AB.html](http://www-star.fnal.gov/Southern_ugriz/Old/www/NGC_458-AB.html)

### 3. OPTICAL OBSERVATIONS AND IMAGING

---

#### 3.5.2 Photometry of Survey Fields

The next step in the photometry is deriving the magnitudes of the objects in the  $r'$  band images. This is best done with the Source Extractor software SExtractor; (Bertin & Arnouts, 1996) software which allows for quick estimation of magnitudes of a large number of objects as compared to IRAF. This was carried out in the following way. The parameters derived from the standard star photometry were used to get the magnitude zero-points for each of the images. Then Source Extractor was used to extract objects from the images and perform photometry on them.

Source Extractor software goes through several steps for the photometry. These are, briefly, background estimation and subtraction, object detection and photometry on the detected objects. The zero-point for magnitudes is different for each exposure and may be calculated by knowing the photometric parameters determined, the exposure time of the image and the airmass for the image. The zero-point is:

$$\text{Zero-point of Magnitude} = -C1 - C2 \times \text{Airmass} + 2.5 \log(\text{Exposure Time}) \quad (3.2)$$

The magnitudes determined for any exposure are measured with the zero-point as the pedestal. The magnitude determined by Source Extractor is:

$$\text{Magnitude} = 2.5 \log(\text{Background Subtracted Counts for the Object}) \quad (3.3)$$

The background determination in Source Extractor may be done separately

for object detection and for photometry. For object detection, the background was determined over a mesh size of 64 pixels. This background was subtracted from the image and objects were detected above it. The object detection was done at a  $2.5\sigma$  level, where  $\sigma$  denotes the RMS for the image. The objects detected are checked aggressively for detection due to nearby bright objects, and if so, discarded.

The flux detected for magnitude determination is background subtracted. The background determination for the photometry is done separately in an annulus around the object. An annulus of width 20 pixels has been used for this purpose. It was found that for getting magnitudes, the Kron-like apertures of Source Extractor work best. This measures the flux of objects in an aperture of size  $2.5 \times r_{eff}$  where  $r_{eff}$  is the effective radius for the object given by the first moment of intensity distribution.

A catalog of objects was produced using the above procedure. This lists the position of each object, the magnitude of each object and the stellarity index of each object, which allows a distinction between stars and galaxies in the images.

### 3.5.2.1 Star - Galaxy Separation

Since galaxies and not stars are of primary interest in any extragalactic survey and not stars, there is a need to differentiate between the detected objects as galaxies or stars. Source Extractor does a preliminary identification of detected objects by generating a stellarity index for the objects. This is the CLASS\_STAR output parameter of Source Extractor. The parameter has a range of 0.0 – 1.0, where

### 3. OPTICAL OBSERVATIONS AND IMAGING

---

an index of 1.0 denotes a perfect point source and an index of 0.0 denotes a galaxy.

The results of using the method on the above photometric catalog of one of the  $r'$  band images *a13* is shown here. The stellarity index distribution is sensitive to the seeing for the image, and in Fig. 3.2 the results of using three different seeing FWHMs for the same image are presented.

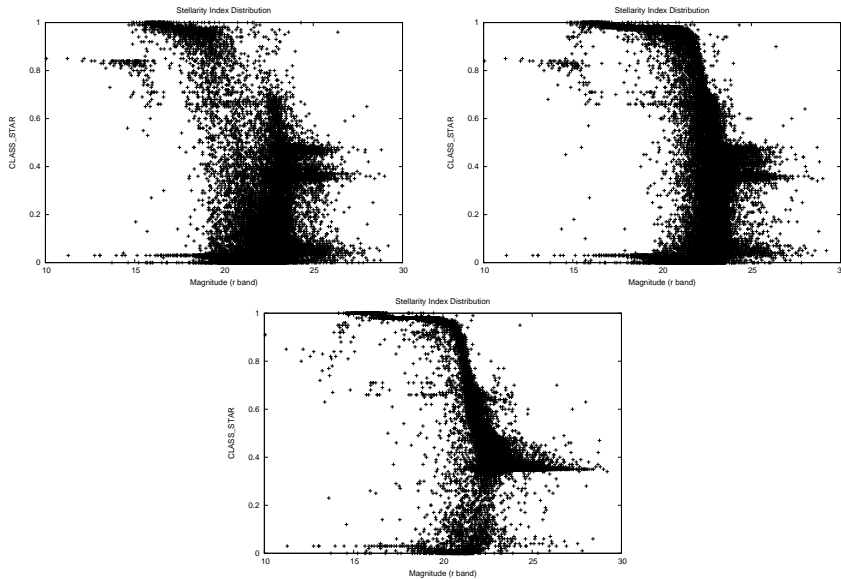


Figure 3.2: Stellarity Index Distribution with PSFs  $0.8''$ ,  $0.91''$  and  $1.5''$  respectively

An estimate of the seeing FWHM for each image has been obtained using the IRAF task PSFMEASURE. This measures the point spread function of a number of specified objects, giving an average FWHM for the psf for an image. For the image *a13*, this is  $0''.91$ . This value has been used to derive the stellarity index for the objects detected in the image.

From the stellarity index distribution for the field with seeing FWHM 0."91, and indeed from other plots of stellarity index distribution as well it is concluded that at low magnitudes (roughly below 20.0 magnitude) stars and galaxies are clearly divided whereas for higher magnitudes (dimmer objects) the separation between stars and galaxies is not clear. At dimmer magnitudes, the stellarity index samples the whole range available to it. With a cutoff of CLASS\_STAR less than 0.2 an identification of galaxies is possible with little mismatch. But since this may result in missing fainter galaxies, the objects in the central 'bulge' of the stellarity index distribution have also been included. This implies shifting the stellarity index cutoff to 0.4.

The method adopted differentiates clearly between stars and galaxies shown in faintness to 22.0 magnitude. Other methods to differentiate between stars and galaxies like using the half-light radius as a function of total magnitude do not operate well at faint magnitudes. Below, a plot of half light radius as a function of total magnitude for a sample image is shown in Fig. 3.3. The horizontal branch locates the stars and the vertical one the galaxies. It is seen that above a magnitude of 20.7, this method does not work well.

In conclusion, the stellarity index has been used to differentiate between stars and galaxies in the work in this thesis. A value of 0.4 has been chosen as a more relaxed upper limit for the stellarity index to be more inclusive and to avoid losing galaxies with higher stellarity indices.

### 3. OPTICAL OBSERVATIONS AND IMAGING

---

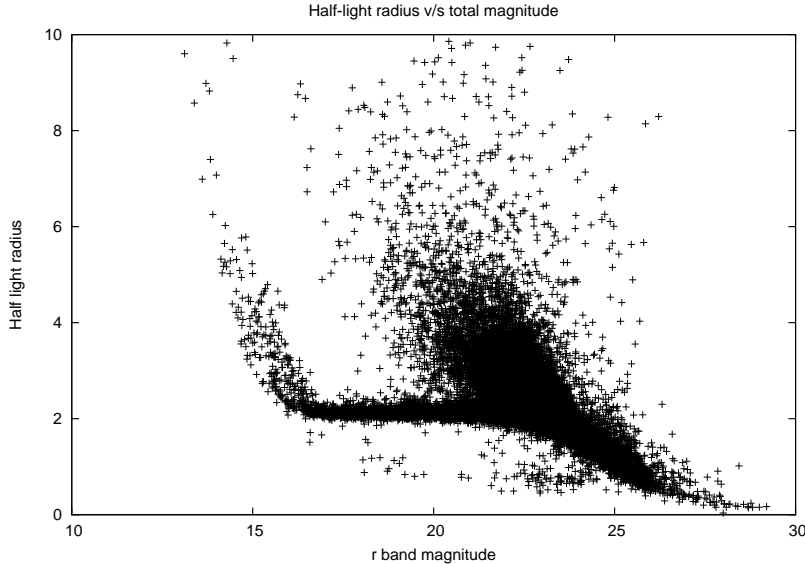


Figure 3.3: Half-light radius (in pixels) plotted versus total  $r'$  band magnitude

#### 3.5.2.2 Comparison of Galaxy Counts

In Fig. 3.4, the derived ATLAS optical galaxy counts are compared with those from the literature. The comparison is between galaxy counts with Zhao et al. (2009) as well as Yasuda et al. (2001). While Zhao et al. (2009) present observations of the Extended Groth Strip (EGS) field in  $u$ ,  $g$  and  $R$  bands (with their  $R$ -band differential counts going deeper than ours), Yasuda et al. (2001) present galaxy counts in SDSS  $u'$ ,  $g'$ ,  $r'$ ,  $i'$ , and  $z'$  filters. ATLAS galaxy counts (complete to 22.75 mag) agree well with the counts presented in both these works.

## 3.6 Summary

The observations and imaging of the optical data for the ATLAS survey, which has been carried out using the IRAF and Source Extractor software have been described in this chapter. The ATLAS survey regions have been covered as a

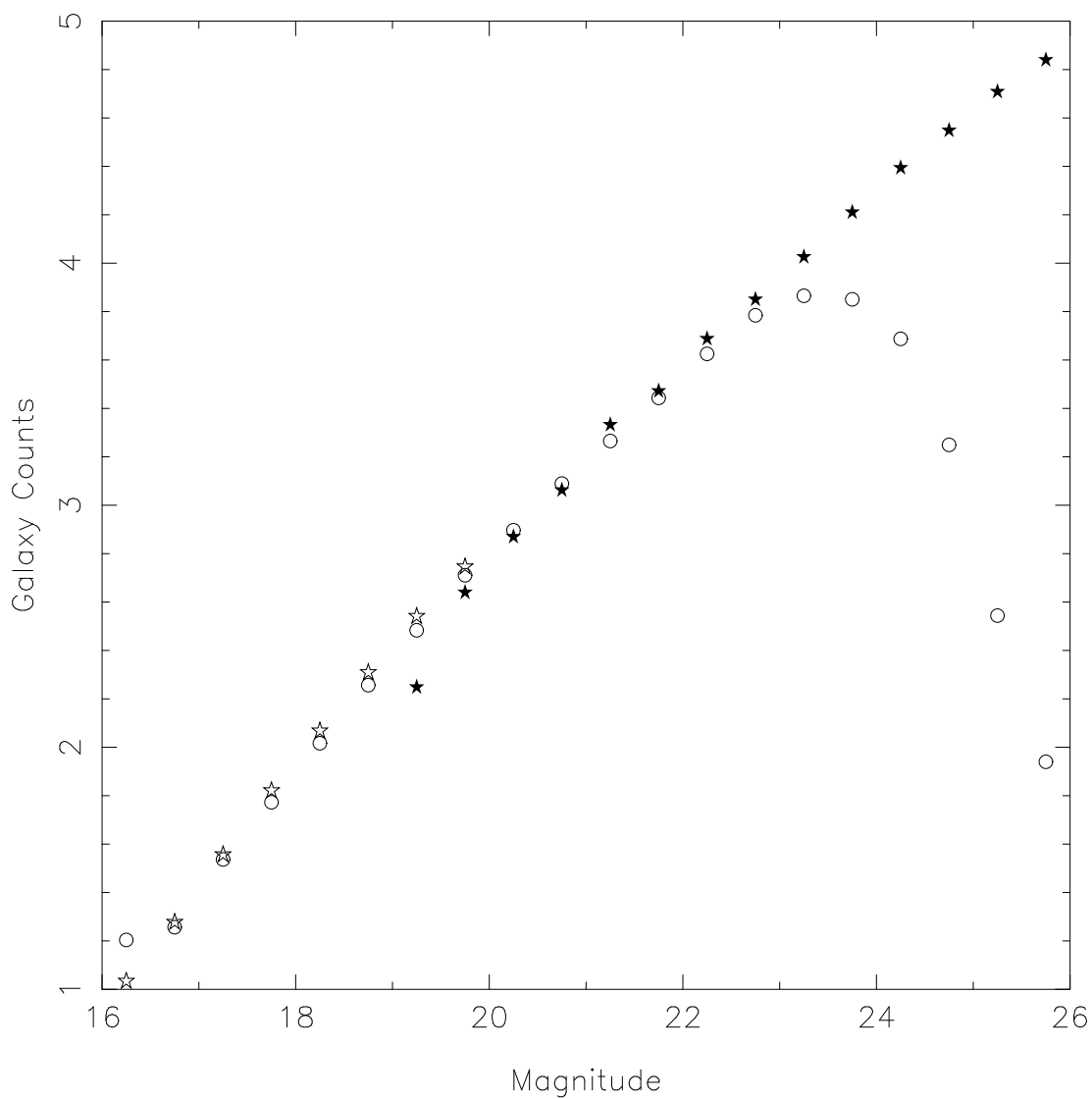


Figure 3.4: The  $r'$  band galaxy counts for the ATLBS survey region (displayed using unfilled circles). For comparison with literature, the counts from Zhao et al. (2009) are shown using filled stars and that of Yasuda et al. (2001) are shown using unfilled stars.

### 3. OPTICAL OBSERVATIONS AND IMAGING

---

mosaic of 28 optical  $r'$  images. Each image is made using 5-point dither pattern with a  $4 \times 2$  array of CCDs. These images are calibrated and presented to be free of artefacts and spurious sources such as cosmic rays and satellite trails. The derived galaxy catalogs are complete down to 22.75 magnitudes. The catalogs created from the optical images provides optical identifications for the hosts of the radio sources in the ATLBS survey and also provides their galaxy environments. These images are used in Chapter 5 to study the environments of the ATLBS extended sources and their relation to asymmetries in radio structure, as well as in the source counts study presented in the next chapter.

The radio source counts

## 4.1 Introduction

Historically, radio source counts has been a key observational probe of cosmology, more specifically of the geometry of the universe. In a Euclidean universe the volume scales with distance as  $V \propto r^3$  whereas the flux density scales as  $S \propto r^{-2}$ , which means that the integral number of sources (for a population of non-evolving sources with constant comoving number density) above any flux density scales as  $n \propto S^{-3/2}$ . Departures from this expectation were key evidence for non-Euclidean geometry. More recently, the geometry of the cosmos has been established with precision and source counts represent a measure of cosmological evolution in radio source populations. The behavior of counts at sub-mJy flux density, the nature and evolution of these sources and the question of exactly what flux density a new population emerges are unclear.

#### 4. THE RADIO SOURCE COUNTS

---

To show the effect of the geometry and population evolution on the estimated source counts, in Fig 4.1 are plotted source counts simulated for a LCDM universe for a single source population, non-evolving in number density as well as source luminosity, and normalized by the expected Euclidean source count profile. Also shown in Fig. 4.1 is the observed PDS source counts for comparison. The simulated source counts have been generated assuming a single population and a single luminosity for the sources (which has been taken to be approximately matching the luminosity of a radio galaxy). In this paradigm, flux density bins act as proxies for the source redshift, with the highest flux density bins corresponding to the local universe. The simulated source counts in Fig 4.1 have been also normalized to match the observed source counts for the local universe (at the highest flux density bins around  $\sim 1$  mJy). Comparing the observed and the simulated counts, it can be seen that the general profile is similar for both; however there are differences. The simulated source counts cannot be matched to the observed source counts at all flux density bins; they have different ‘shapes’. This suggests that the source population is evolving in luminosity and/or number density.

The explanation of the observed source counts is significantly different if there are multiple populations of radio sources contributing. Below in Fig. 4.2 the case when two non-evolving populations contribute to the total source counts has been shown. In these counts, a second nonevolving population of sources has been added. This population of sources has luminosity approximately four orders of magnitude smaller, while having a comoving number density four orders of magnitude higher. The combined source counts are shown using a dashed line. It may be seen that the combined counts show a flattening at sub-millijansky levels,

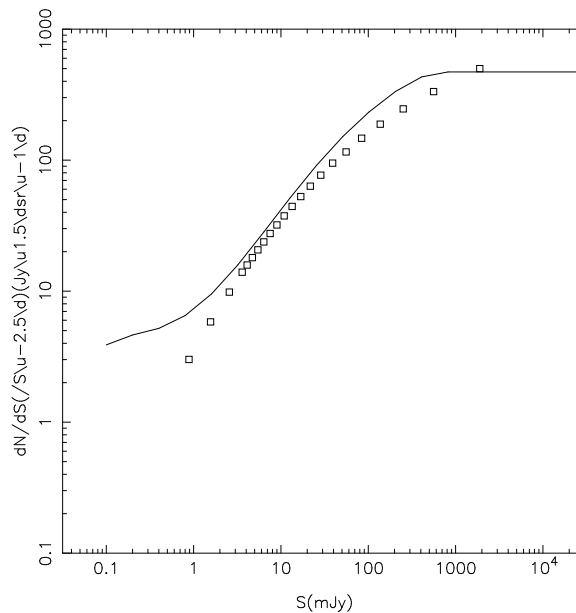


Figure 4.1: Simulated source counts for LCDM universe. The continuous curve shows the fit to the observed Phoenix Deep Survey source counts.

similar to that exhibited by the observed source counts. This simulation shows that a flattening of source counts may be produced by two (or more) populations of sources with different luminosities as well as different number densities. Such modeling may be made more accurate by considering evolving (in luminosity as well as number density) source populations.

Indeed, at flux densities  $\leq 1.0$  mJy a ‘flattening’ of normalized differential source counts has been widely reported in literature (Windhorst et al. (1985) (WMO85 henceforth), Hopkins et al. (2003), Huynh et al. (2005) and references therein). The rms noise level in the latter studies are:  $45 \mu\text{Jy}$  for WMO85, varying between 12 to about  $100 \mu\text{Jy}$  for Hopkins et al. (2003) (see Fig. 9 from Hopkins et al. (2003)) and approximately  $10 \mu\text{Jy}$  for Huynh et al. (2005). The flattening is observed as an apparent change of slope for the normalized differential source

## 4. THE RADIO SOURCE COUNTS

---

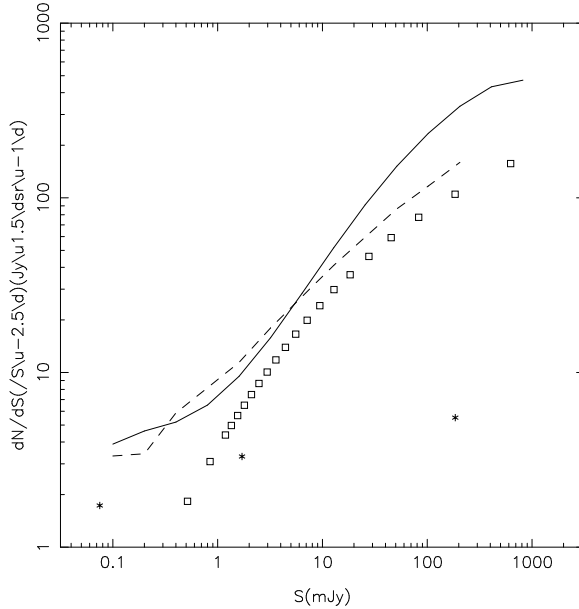


Figure 4.2: Simulated source counts for two non-evolving populations for LCDM universe. Squares denote the source counts from the first population and stars depict the second population. The dashed curve shows the combined population. The continuous curve shows the fit to the observed PDS source counts for comparison.

counts from  $\sim 0.7$  at  $5.0 - 100.0$  mJy to about  $0.4$  in the  $0.25 - 5.0$  mJy range. The flattening of sources has also been seen at frequencies as low as 325 MHz. At 610 MHz, recent observations of the radio sky (Garn et al. (2008b), Ibar et al. (2009) and Moss et al. (2007)) have provided radio source counts which show the flattening. For example, Garn et al. (2008a) present radio source counts at 610 MHz from the ELAIS N1 field which show a flattening of sub-mJy sources at  $\sim 1 - 2$  mJy. The same field was observed at 325 MHz by Sirothia et al. (2009), who report a flattening of radio source counts at  $\sim 1$  mJy (corresponding to  $\sim 0.3$  mJy at 1.4 GHz), which has been corroborated by Mauch et al. (2013).

On the other hand, identification of the population leading to the flattening

mentioned above has been uncertain. WMO85 examined the optical identifications of faint radio sources and found that the sub-mJy radio source population is dominated by blue spiral galaxies. Later studies, however, have arrived at discordant results and identify the sub-mJy sources with different populations: starburst galaxies (Condon (1989), Benn et al. (1993), Huynh et al. (2005)), early type galaxies (Gruppioni et al., 1999), low (radio) luminosity active galactic nuclei (AGNs) (Huynh et al., 2008) or a mixture of these. Since spectroscopically complete samples of sub-mJy sources are difficult to obtain, the exact nature of the population observed as sub-mJy radio sources remains uncertain. Some samples of sub-mJy radio sources, which may have relatively high fraction of sources identified in other bands may be used to determine the nature of the flattening population. For example, Simpson et al. (2006) present a catalog of radio sources which have 90% identifications available through deep Subaru observations. Studies of radio sources at different frequencies may allow for spectral-index based methods to distinguish the population responsible for the flattening (see Ibar et al. (2009) and references therein). However, it is widely agreed that flattening below about 1.0 mJy requires an evolving population that is different from those that dominate counts at higher flux densities.

Accurate modeling of radio source counts involves accounting for *multiple, evolving* source populations which may be differentiated by the mode of energy generation, i.e. star-forming galaxies and AGNs. Further distinction may be necessary, e.g. radio-quiet AGNs and radio-loud AGNs, the latter of which may be further differentiated into low-luminosity FRIs and high-luminosity FRIIs and quasars. The different populations may exhibit different rates of cosmic evolu-

#### 4. THE RADIO SOURCE COUNTS

---

tion. This evolution may be pure luminosity evolution or pure density evolution or a combination of the two. There are many models proposed in the literature which strive towards an explanation of the cosmic evolution of the radio sources (see de Zotti et al. (2010) for a detailed description).

It may be noted here that the literature is not consistent in observing a flattening in counts at mJy flux density; for example, the counts in Prandoni et al. (2001) and Subrahmanyan et al. (2010) are consistent with a continuation in the slope of the differential counts below mJy flux density. Potential causes for the discrepancy are that deep radio surveys often suffer from inadequate sky coverage that is necessary to average over real-space clustering, wide-field surveys often do not go sufficiently deep and so biases arising from the proximity of the detection threshold to the image noise may distort measured counts. Additional uncertainty arises from lack of understanding of the radio structures in sub-mJy radio sources, which may lead to biases related to the ability of the survey to catalog sources from detections of source components. In conclusion, accurate measurements of the source counts at sub-mJy flux densities are needed to correctly estimate the cosmic evolution of radio sources.

The sensitive radio images produced for ATLAS survey regions as well as the availability of optical observations makes ATLAS well-suited for such a study. Therefore the improved imaging of the ATLAS survey regions has been used to revisit the 1.4 GHz source counts: the survey has sufficient sensitivity to probe the sub-mJy regime, and the relatively large sky coverage avoids clustering related uncertainties. A specific improvement in this work is the care taken to identify

sources with low surface brightness by making use of low resolution images, and using multiple indicators to identify components of sources. The low resolution images were used to make initial identifications so that the sources that might be resolved into multiple components at higher resolution are identified correctly. The blending issues inherent in using low resolution images have been avoided using higher resolution images to identify blends. In addition, the use of low resolution images (beam FWHM = 50") almost completely removes effects of resolution bias (for a detailed discussion, see Section. 4.3.1.4). These strategies, together with use of optical images (described in Chapter 3) to locate candidate galaxy hosts and a careful visual examination of resolved and complex sources instead of automated classification ensures that the ATLBS catalog is a ‘source catalog’ as opposed to a ‘component catalog’. The distinction between ‘sources’ (which are single sources) as opposed to components (which may be parts of a single source or unrelated sources which are close to each other due to projection effects) is crucial in estimating the true source counts.

The organization of this chapter is as follows. In Section (4.2) details of the procedure adopted for source detection and estimation of source flux densities are given. In Section (4.3) the source counts along with the corrections necessary to derive the true counts from the observations are presented. Subsequently, in Section (4.4), the ATLBS source counts are compared with previous work. Finally, in Section (4.5), the conclusions are presented.

### 4.2 On the identification of sources in the ATLBS survey

The low and high resolution ATLBS images have been jointly used in the strategy adopted for source detection and classification as well as for estimations of flux density. The former, with 50'' FWHM beam, was made using the 750-m arrays and the latter, with 6'' FWHM beam, was made using all of the visibilities up to 6 km baselines. The low resolution images are used to identify sky regions in which to search for source components using the high resolution images. The low resolution images have relatively lower chance of missing a source due to its being resolved: known in the literature as ‘resolution bias’, resolved sources with same integrated flux density would have relatively lower peak flux density and hence may not have image pixels above the detection threshold, this would result in high resolution images missing such sources that may be detected in lower resolution images. The high resolution images have been used to detect source components, identify blends and classify the sources. Various aspects that potentially introduce bias and errors in source detections such as the thermal noise in the images and the effects of blending-confusion have been examined, as described below.

#### 4.2.1 Thermal Noise Considerations

As mentioned above, regions which contain sources have been identified in the low resolution image. The size of these regions, or ‘footprints’, are of importance in determining the threshold for source detection, along with considerations related

## 4.2 On the identification of sources in the ATLAS survey

to the image thermal noise (where ‘thermal’ noise is the composite of the receiver noise, the sky as well as ground noise) and source blending-confusion effects in the high resolution image. Here the procedure to determine the detection thresholds separately for source identification in low resolution images and for component identification in high resolution images is described.

A source detection threshold can be derived for an image if the number of spurious sources expected above any threshold may be estimated. The latter can be calculated easily if the noise follows a Gaussian distribution with a known variance. But for an image convolved with a point spread function, this would only give the total area in the image above the threshold. The actual number of spurious ‘sources’ or ‘islands’ (connected pixels) above the threshold would depend on the shape and size of the point spread function. Above the threshold only the summits of the spurious ‘sources’ might be observed, with a smaller area than that corresponding to the FWHM of the main lobe of the point spread function. Therefore, the detection threshold needs to be determined taking this into account.

### **4.2.1.1 Detection Threshold in the Low Resolution Image**

For the low resolution image, an empirical approach towards threshold determination has been employed. Since the initial noise distribution before being convolved with the point spread function is expected to be Gaussian (with a zero mean), the number of positive noise peaks above a flux density value (say  $S_{cutoff}$ ) is expected to be the same as the number of negative noise peaks below  $-S_{cutoff}$ . Since the

#### 4. THE RADIO SOURCE COUNTS

---

positive noise peaks cannot be distinguished from real sources, the number of negative peaks has been used to estimate the detection threshold. The number of negative peaks is affected by the area which is covered by ‘sources’ at every detection threshold. This is because a negative peak occurring at the location of a source will not be detected as a negative peak in the counting. This has been corrected by the ratio of total area covered by the sources above any threshold and the total image area. For example, 68 noise peaks below  $-0.38$  mJy in the survey region were found and, after correction for the above, it was estimated that there are 71 spurious noise peaks below this threshold in the entire survey region including those areas covered by genuine sources. It is expected that very similar numbers of positive noise peaks above  $+0.38$  mJy are present in the survey region. If Gaussian statistics is assumed, only about 2 spurious sources in the entire survey region above a  $4\sigma$  threshold are expected; the significantly larger number of spurious sources suggests that the image noise is non-Gaussian at this level. Since 1244 sources above  $0.38$  mJy in the ATLBS survey region are found, it may be concluded that the fraction of spurious sources at a threshold of  $0.38$  mJy is  $5.7\%$ . The percentage of spurious sources changes with the detection threshold. The percentage of spurious sources goes from  $41\%$  at  $0.29$  mJy to merely  $0.3\%$  at a threshold of  $0.48$  mJy. However, the number of sources which will not be detected will also rise with the threshold. Therefore  $0.38$  mJy has been chosen as the threshold for the low resolution image (a  $4\sigma$  threshold), with an expected  $5.7\%$  of false detections. Therefore the reliability of the catalog is  $94.3\%$  at the detection threshold. The number of negative peaks might be affected by the fact that negative peaks have not been deconvolved, and they would retain the dirty beam pattern. This may give rise to negative peaks arising from the sidelobes of

## **4.2 On the identification of sources in the ATLBS survey**

the beam. However, since the sidelobe level is below 10%, the contribution from the sidelobes to negative peaks is not expected to affect the above analysis. It may be noted here that the above discussion does not consider the sources which have true flux density below the detection threshold but are detected above the threshold due to noise peaks biasing their intensity above the threshold. Simulations of noise bias which estimates this effect were carried out and the source counts were corrected for this effect; these corrections are discussed below in Section (4.3).

### **4.2.1.2 Detection Threshold in the High Resolution Image**

For the high resolution image, a different strategy for determining the thermal noise limited detection threshold has been followed. Because the search for the high resolution peaks is carried out in the footprints of the sources detected in the low resolution images, the threshold for the detection of the high resolution peaks is determined using the footprint area in which the source components might be located and not the complete area of the image. In this way, a unique detection threshold for each source component may be used which would depend on the footprint area in which the source component is located. The aim here is to keep the number of spurious components detected in high resolution images to be one per 10 footprints. Since in most cases one footprint corresponds to one source detected in the high resolution image, the above criterion corresponds to a false detection rate of approximately 10%. The mean number of pixels per negative peak by measuring the number of negative peaks and pixels at a given flux density cutoff has been determined empirically. It was found that the number of pixels

#### 4. THE RADIO SOURCE COUNTS

---

per peak is 1.37 for specifically the synthesized beam and image sampling in the high resolution ATLAS image. Assuming that the number of spurious positive pixels is similar to that of negative pixels, the number of spurious positive peaks can be estimated. For each footprint (in which source component peaks in the high resolution image were detected) the flux density threshold was chosen so as to keep the probability of including noise peaks as spurious source components below 10%. If a low threshold is chosen for identifying peaks in the high resolution image as source components, then a large number of spurious components would be considered as source components and, therefore, a large number of sources would be misclassified as multicomponent and hence complex. If a high threshold is chosen, then genuine source components might be missed and sources would be misclassified as extended and resolved in the high resolution images or misclassified as unresolved when they are actually complex. However the latter misclassification is avoided by recognizing that the integrated flux density in the high resolution image falls short of that in the low resolution image and by classifying such sources as complex in these cases. Misclassification of unresolved sources would happen predominantly in cases where the peak flux density is close to the rms image thermal noise. For a flux density threshold of  $S_{th}$ , if the probability of occurrence of spurious pixels above the threshold is  $P(S_{th})$  (the probability is determined by integrating the assumed Gaussian distribution for the pixels), then the number of spurious source components in the footprint area is  $A_f P(S_{th})/1.37$ , where  $A_f$  is the number of pixels in the footprint. To keep the number of spurious source components in each footprint less than 0.1, the flux density threshold is given by  $P(S_{th}) < 1.37 \times 0.1/(A_f)$ . This recipe has been used to compute the flux threshold uniquely for each footprint. As the number of

## 4.2 On the identification of sources in the ATLBS survey

spurious sources is not directly estimated from the number of negative peaks in the image, the effect due to the sidelobes of the dirty beam, as described above, does not influence the detection threshold directly.

The thermal noise limits discussed above along with considerations related to source blending-confusion, which are discussed next, lead to the adopted detection threshold for the ATLBS survey and hence determine the error in source counts and confidence in classification.

### **4.2.2 Source Blending-Confusion**

Source blending-confusion (also called source confusion in the literature) is because any telescope of finite size has only a finite angular resolution. Since the synthesized beam has a finite size, this makes the detection of two distinct sources that are located close to each other difficult because the sources may appear blended with each other in the image. Blending-confusion limits the flux density limit to which sources may be reliably identified distinctly in a survey, this is a limitation apart from that arising due to the image thermal noise. See Jauncey (1968) and Mitchell & Condon (1985) for some of the earliest descriptions of this effect. In this section the effects of the source blending-confusion on source detection in the ATLBS survey are described. Since thermal noise considerations suggest a source detection threshold of 0.38 mJy for the low resolution image, the source blending-confusion for this threshold has been examined to confirm that the latter are less important than the limitation arising from thermal noise.

#### 4. THE RADIO SOURCE COUNTS

---

The effects of source blending-confusion for the ATLAS high resolution images (beam FWHM =  $6''$ ) were estimated using simulations, which are described next. It was assumed that the flux density distribution of sources follows the source counts derived from the PDS survey (Hopkins et al., 2003). The simulation Poisson distributed sources over a sky area corresponding to the total area imaged in the ATLAS survey (8.42 square degrees). Blending-confusion causes sources to be shifted from the bin corresponding to their true flux density to a bin with higher flux density. The source counts in any given flux density bin change due to the migration of sources in and out of the bin: into the bin from lower flux density bins and out of the bin to higher flux density bins. The flux density range for the simulation was chosen to accurately model the effects of blending- confusion for ATLAS survey. The simulations allow for multiple blendings with other sources. The lower limit of the range was chosen so that the effects of the sources changing bins due to blending-confusion are reliably modeled for the bins above 0.38 mJy, which is the detection threshold flux density in this work. The upper limit of the range is chosen so that the brightest sources in the survey are accounted for (in the simulation, detection of only a single source in the highest flux density bin is expected). Additionally, the shapes of the sources in the synthesized images (which have been restored following deconvolution) were set to be Gaussian with a FWHM of  $6''$ . The ‘radius’ of each source was taken to be the distance from the source peak at which the intensity drops to half the threshold flux density. Sources were counted as blends if the distance between their peaks was smaller than the sum of the radii of the two sources, since in this situation the two sources would appear to be connected by emission above the threshold flux density in the image. Those sources that have peak flux density less than half the threshold flux

## 4.2 On the identification of sources in the ATLBS survey

---

density would appear ‘blended’ if they are located within the radius of a source that has peak exceeding half the threshold flux density, *i.e.*, if the radius of the stronger source is smaller than the distance between the peaks. An arbitrarily small radius  $\ll 6''$  is assigned to such sources, which allows for the possibility that two such sources blend together and then blend with other sources.

The simulations were made with octave bin ranges from 0.1 mJy upwards, and showed that the recovered flux density distribution was not significantly altered. Most blending-confusion of sources occurs at the lowest flux density bins, and the source counts remain unchanged for higher flux density bins. The number of sources migrating into a bin from lower flux density bins and the number of sources migrating out of the bin due to blending-confusion were also estimated. In the bin 0.4 – 0.8 mJy the source distribution was unchanged within errors. For these and higher flux density bins, the number of sources migrating to and out of the bin matches. For sources in bins above a flux density of 3.2 mJy, the blending-confusion effects were found to be negligible, possibly due to the relatively sparse distribution of sources above this flux density. For source counts derived herein from the ATLBS, based on a detection threshold of 0.38 mJy, the correction factors required to account for source blending-confusion is less than 0.1%.

It may be inferred from the above analysis that the threshold for source detection in the high resolution images might be placed at or even below 0.38 mJy, in so far as blending-confusion is concerned, while keeping the errors introduced in the source counts due to blending-confusion below 1%. Therefore, the detection threshold for components in the high resolution image (within the footprint area

## 4. THE RADIO SOURCE COUNTS

---

as outlined in the previous section) may be chosen based solely on thermal noise effects in the high resolution image. It may be noted here that it is possible that the low resolution image may have blends, which will be identified as separate sources using the high resolution image.

### 4.2.3 Bandwidth Smearing Correction

Bandwidth smearing, which is the radio analog of chromatic aberration, arises due to averaging of visibilities over a bandwidth. The effect of bandwidth smearing on the source image is to reduce the peak flux density and to ‘smear’ it around the source; the integrated flux density is unaltered. Since the peak flux density of detected sources is used in the classification of the sources (described in Section 4.2.4), in particular to differentiate between unresolved and resolved sources, the bandwidth correction needs to be applied prior to source classification. Below the estimation of the magnitude of this effect is described.

For the ATLBS survey, the total bandwidth is divided into 2 bands each with a useful width of 104 MHz. Each of these bands is further divided into 13 independent channels of equal width and the data is acquired as multi-channel continuum visibilities, which thus significantly reduces the bandwidth smearing effect. Simulations were carried out to estimate the bandwidth smearing for the ATLBS sources. Visibilities corresponding to unresolved sources with a flux density of 1 mJy were added to data in a single pointing at different distances from the image center. Any given source in the mosaic is at a maximum distance of  $16'.4$  from the nearest pointing center. The fact that bandwidth smearing depends on the

## 4.2 On the identification of sources in the ATLBS survey

---

product of the bandwidth and the source distance from the center was utilized to derived estimates of bandwidth smearing within the 8 MHz bands by scaling the offset distances at which sources are added by a factor of 13 and computing visibilities averaged over a band of  $13 \times 8$  MHz. The advantage of performing the above procedure is that it does not make any assumptions regarding the shape of the channel bandpass by using data from real observations used for producing the image. A polynomial fit was obtained for the attenuation as a function of distance, which is made use of to correct the measured peak flux densities. The maximum bandwidth smearing correction thus obtained is 8% at a distance of  $16'.4$  from the nearest pointing center.

The bandwidth smearing estimated above is that for a source in a single pointing. In a linear mosaic image, however, the total flux density at any point is an addition of contributions from different pointings. Since bandwidth smearing at any given point in a pointing depends on the distance of that point from the pointing center, different pointings contributing flux density at any point would each have different bandwidth smearing associated with the contributed flux density. This is especially important at those points in the mosaic where multiple pointings contribute. The following procedure was carried out to estimate the additional bandwidth smearing correction required for the ATLBS mosaic images.

At any point in a mosaic, the contribution of the flux densities is a linear sum:

$$F = \sum_i F_i'' \quad (4.1)$$

#### 4. THE RADIO SOURCE COUNTS

---

where  $F$  is the total flux density and  $F_i''$  are the weighted flux contributions from the ‘i’ contributing pointings. In absence of bandwidth smearing, the above is a weighted sum which will produce the least noise at the point. To ensure that the noise is least, the sum is weighted with the inverse of the variance of the noise in the individual images. This can be written as:

$$F = \frac{\sum_i F_i w_i}{\sum_i w(i)}, \quad (4.2)$$

where  $w(i) = \frac{1}{\sigma_i^2}$  are the weights and  $F_i$  is the primary beam corrected flux from the ‘i’th pointing. Assuming that the noise in each image is the same, the above equation can be written as :

$$F = \frac{\sum_i F_i P_i^2}{\sum_i P_i^2}, \quad (4.3)$$

using  $\sigma_i = \sigma_0/P_i$ , with  $P_i$  being the primary beam pattern and  $\sigma_0$  being the rms noise in the images (for a single pointing, this reduces to the identity  $F = F$ ). The actual flux density contribution from the pointing is:  $F_i' = F_i \times P_i$ , which means that the above equation can be written as :

$$F = \frac{\sum_i F_i' P_i}{\sum_i P_i^2} \quad (4.4)$$

However, the flux density contribution from the individual pointings is affected by the bandwidth smearing, i.e.  $F_i' = b_i P_i F$ , where  $b_i$  are the bandwidth smearing factor for the contributions from individual pointings. Therefore, the flux density actually obtained after the weighted sum is:

$$F' = b_t F = \frac{\sum_i b_i P_i^2 F}{\sum_i P_i^2} \quad (4.5)$$

## 4.2 On the identification of sources in the ATLBS survey

---

, which implies:

$$b_t = \frac{\sum_i b_i P_i^2}{\sum_i P_i^2}, \quad (4.6)$$

where  $b_t$  is the total bandwidth smearing factor.

Knowing the primary beam pattern of the ATCA antennas as well as the bandwidth smearing corrections for a single pointing, the total bandwidth smearing correction at any point in the mosaic may be estimated. The pointing grid for the ATLBS mosaic is a hexagonal grid, in which the pointing centers are separated by 28.6', which is large compared to the HWHM of the ATCA primary beam, which means that the pointings are well separated from each other. Combined with the fact that the contribution of sources outside the primary beam main lobe is explicitly rejected before forming the mosaic,  $b_t$  differs very little ( $\sim 1\%$ ) from the bandwidth smearing factor calculated without taking the effects of the mosaic geometry into account.

The correction factor derived above is correct for unresolved sources. The peak flux densities for resolved sources are less affected by bandwidth smearing; the correction factors depend on the source structure. Nevertheless, below the derived correction factors have been simply applied to the measured peak flux densities of all sources. In the case of unresolved sources, the correction is expected to aid correct classification; in the case of resolved sources, the overcorrection that results from the above prescription is not expected to alter the classification.

## 4. THE RADIO SOURCE COUNTS

---

### 4.2.4 On the classification of radio sources in the ATLBS survey

#### 4.2.4.1 Initial Source Classification Using the Low Resolution Image

The source detection and initial classification was made using the low resolution image. The ‘islands’ of pixels above a threshold of 0.38 mJy are identified in the low resolution image and these sky regions are used to estimate the source parameters in the low resolution image. The sources are classified into (i) unresolved sources, (ii) resolved single-Gaussian sources and (iii) complex sources. A fit with Gaussian models is attempted for all sources. In the case of resolved sources, if the Gaussian model fit is good, then the source is noted as a Gaussian source. If the fit fails and multiple Gaussian are needed to obtain a good fit to the source, then the source is flagged as a multicomponent or complex source.

#### 4.2.4.2 Final Source Classification Based on the High Resolution Image

The final classification of the sources is made using the high resolution image that has beam FWHM of  $6''$ , which provides a better representation of the source structure. The high resolution image also helps in distinguishing sources which might be blended together in the low resolution image. For this classification step a method similar to that described in the previous section has been used.

Unresolved sources are identified by comparing the peak flux densities in the low and high resolution images. For unresolved sources, it is expected that the

## 4.2 On the identification of sources in the ATLBS survey

---

peak flux at high and low resolution are equal, within errors. If the peak flux in the high resolution image is higher than the peak flux in the low resolution image, the source is classified as unresolved, since this can only happen if noise increases the peak flux in high resolution image and/or lowers it in the low resolution image. If the peak flux in the high resolution image is lower, the source is classified as a point source if it is within a  $2\sigma$  interval of the low resolution peak. The probability of a noise peak exceeding  $2\sigma$  is 2.2%; therefore, approximately 2% of unresolved sources may be misclassified by this scheme. Extended sources (in the high resolution image) might get misclassified as unresolved sources due to noise increasing the high resolution peak flux density or decreasing the peak flux density in the low resolution image so as to satisfy the above condition. However, if the source is extended in the high resolution image, then for sources in which the peak flux density is much greater than the image thermal noise the additive noise required for misclassification is large and has a very small probability associated with it. However, if the source peak flux density is close to the detection threshold and nearer the noise floor, then there is a higher chance that an extended source may get classified as an unresolved source. Therefore, close to the detection threshold, discriminating between unresolved and extended sources might be incorrect.

The ‘footprint’ of any source is defined to be the area of its ‘island’ in the low resolution image (If the peak flux of the source in the low resolution image is not more than twice the threshold, then the footprint is redefined to be the contour at half the peak flux. This is done so that the high resolution image is examined for components in at least a FWHM beam area of the low resolution image). The

#### 4. THE RADIO SOURCE COUNTS

---

footprint is used for estimating the flux density and for component identification in the high resolution image. The integrated flux of the source is estimated by iteratively fitting Gaussian models to the source and subtracting these model components till the peak residual in the footprint falls below a threshold. The threshold for any source in a given footprint is determined as outlined in the previous section. This may result in underestimation of the integrated flux in the high resolution image when source components in the high resolution image have their peak flux densities below the threshold, but the recipe avoids accumulating spurious flux density from noise peaks to the integrated flux. The number of iterations for each source is noted and the source is assigned a type based on the number of iterations, as discussed below.

If a single iteration is enough to satisfy the above condition then the source, as seen in the high resolution image, is deemed to be a single component. For these sources it is examined if the integrated flux in the low resolution image is the same as the integrated flux in the high resolution image (within errors). Only if both the above conditions are satisfied the source is classified as a single component Gaussian. Only those sources that have been classified as unresolved or resolved single component Gaussian sources in the low resolution image are examined in the above manner, since any source which is classified as complex in the low resolution image is unlikely to be a single component Gaussian in the high resolution image. The Gaussian sources and the unresolved sources together form the sources whose flux densities have been estimated in the above automated process.

If multiple iterations are needed for the modeling of the high-resolution inten-

## 4.2 On the identification of sources in the ATLBS survey

sity distribution within the footprint, or if the sum of the flux densities associated with the components in the high resolution image is less than the integrated flux density measured in the low resolution image, then the source is classified as a complex source. Multi-component Gaussian modeling of complex sources using the high resolution image may underestimate the integrated flux density of complex sources because such a method might miss flux density associated with extended emission, which may be present in such sources. To avoid such problems, the estimation of integrated flux density for the complex sources is best done not by modeling, but simply summing the pixel intensities enclosed within the ‘footprint’. Additionally if it is ascertained that the complex source is a single source (even if it has multiple components) and not multiple confused sources, then the integrated flux measured as in the low resolution image may be adopted as the integrated flux density of the source.

Sources for which the noise gives a fitted diameter less than the beam are considered point sources and the peak flux density is then the optimum estimate for both the flux densities.

For sources classified as unresolved or single-component Gaussians on the basis of the high resolution image, the low resolution integrated flux density has been adopted as the estimator of the true integrated flux density, rather than using its counterpart from the high resolution image. It may be noted that the integrated and peak flux densities of the single component Gaussians and unresolved sources are the same, within errors, in the high resolution and low resolution images.

## 4. THE RADIO SOURCE COUNTS

---

For those sources classified as complex in the high resolution images, it was examined whether the source was composed of only a single component in the high resolution image. If the source consists of a single component and the integrated flux contained in the low resolution image is deemed to be the entire integrated flux for the source then again the low resolution (fitted) integrated flux was taken as the estimate of the integrated flux density for the source. Those sources that are classified as complex in both the high and low resolution images as well as additional sources declared complex in the high resolution image and displaying multiple components are examined individually by eye rather than by the automated algorithm.

### 4.2.5 The identification of Sources with Complex Structures

In rare cases, it was found that different components of a single source (e.g. lobes of a radio galaxy) lie on separate islands and are hence misidentified as separate sources in the low resolution images. More frequently, it was found that unrelated sources are located within a single island in the low resolution image. Each such source was examined by eye (342 such sources in all) and it was ascertained if the components composing them are parts of a single source or unrelated sources which are only close in projection: the following steps were adopted to arrive at a classification. It may be noted here that it is essential to determine the classifications of such sources to better estimate the true source counts and all information available (radio as well as optical) for a given source ought to be used.

## 4.2 On the identification of sources in the ATLBS survey

---

1) Optical images ( $r'$  band) of the ATLBS survey regions were examined for the presence of hosts for the radio sources. The host was identified using overlays of the high resolution radio images to identify galaxies in the optical image at the location of the radio core. Where radio cores were undetected, the location of the centroid of the two radio components, which are suspected to be parts of a double source, was examined for the presence of an optical galaxy. If candidate optical hosts were indeed present at these locations, the pair of radio sources was deemed to be a double radio source and the galaxy was taken to be the host. The optical matching was attempted for 299 sources, out of which 187 were found to have optical identifications. Redshift information is available for 24 of these sources. None of these identifications appeared to be a QSO.

2) The radio sources for which no optical host was found were examined in radio images of intermediate resolution (beam FWHM =  $10''$ ) for any connected emission between the radio components. Separately, the integrated flux for these sources was compared to the integrated flux measured in the low resolution image (The estimation of flux density in these cases was done not through model fitting but by summing the pixel intensities within the sky area corresponding to the source). If the integrated flux of the components together is less than the integrated flux as estimated from the low resolution image, then this was interpreted as due to missing extended emission in the high resolution image. Assuming that the missing extended emission would connect the components, it was assumed that the component pair are parts of the same source.

#### 4. THE RADIO SOURCE COUNTS

---

Source Type	Classification Criteria	Number of Sources	Percentage
Unresolved Sources (P)	Peaks flux densities match between low and high resolution images.	562	41.0
Single Component Gaussian Sources (G)	Single iteration of Gaussian model fitting recovers all the integrated flux.	268	20.0
Complex Sources (C)	Multiple iterations of Gaussian model fitting needed to account for all the integrated flux.	382	28.0

Table 4.1: The source types and the classification criteria along with the number of sources of each type and the corresponding percentages. The remaining 154 sources out of a total of 1366 are unclassified. These sources have their peak densities below the detection threshold but have integrated flux densities above the flux density threshold.

Components deemed to be parts of a single source by the above methods were cataloged as a single source and classified as complex. In those cases where the sources were deemed to be unrelated, the flux for each source was measured separately. Using the high resolution image, the source classification was made as unresolved, single Gaussian or complex and the flux density estimated accordingly for each type (as described in the previous subsection).

In total, 128 sources in the low resolution image were found to be blends of separate sources. This is 10% of the sources found initially in the low resolution image.

Table 4.1 presents the classification criteria in condensed form. A sample of the ATLBS source catalog is presented in Table 4.2. The complete catalog is in Appendix 1.

### 4.2.6 Completeness in radio source detection

To estimate the true source counts, it is essential that the source list from which the counts are derived is complete - i.e. there are no sources missed in the detection down to the detection flux density threshold. There are a few effects which can affect the completeness of the source list. One of these is the resolution bias - the ‘resolving out’ of sources due to the high resolution of the image. This can lead to incompleteness in the source list. However, our strategy of using the low resolution image for the initial detection takes care of this issue. We have estimated the correction required to the detected source numbers. This ensures that the effects of resolution bias, while small, are accounted for. The details of addressing the resolution bias are presented in Section 4.3.1.4.

Another effect which can affect the completeness of the source list is the noise bias or Eddington bias. Very briefly, this is the effect introduced by the noise in the image which changes the measured flux density of the sources; which leads to changing the measured distribution of the sources with flux from the true distribution. More specifically, it may lead to incompleteness of the source list by lowering the flux of the sources near the detection threshold below the threshold. In fact, sources may also migrate from lower flux density bins to those above. This issue has been addressed in detail by carrying out simulations to estimate the fraction of the sources which may be lost or gained due to noise bias and correcting the number of detected sources by that fraction correspondingly. The detailed discussion on the noise bias is given in Section 4.3.1.1.

#### 4. THE RADIO SOURCE COUNTS

---

Source Name	RA (J2000)	Dec (J2000)	$S_{int}$ (mJy)	Source Type	Number of Components
J0025.5-6640	00:25:30.82	-66:40:31.5	1.87	G	
J0025.6-6700	00:25:38.90	-67:00:19.5	1.60	G	
J0025.7-6634	00:25:46.04	-66:34:35.1	0.56	M	
J0025.9-6621	00:25:58.71	-66:21:20.4	215.26	C	1
J0025.9-6629	00:25:54.62	-66:29:46.0	0.71	C	1
J0025.9-6632	00:25:56.75	-66:32:59.7	1.89	C	1
J0025.9-6725	00:25:59.89	-67:25:38.8	1.06	P	
J0026.0-6628	00:26:02.54	-66:28:06.0	0.61	M	
J0026.0-6638	00:26:05.38	-66:38:15.5	0.49	C	3
J0026.2-6643	00:26:12.76	-66:43:45.0	0.80	P	
J0026.2-6646	00:26:12.14	-66:46:01.7	0.72	C	1
J0026.3-6708	00:26:19.80	-67:08:43.0	2.36	P	
J0026.3-6713	00:26:21.13	-67:13:45.7	0.69	P	
J0026.4-6721	00:26:28.95	-67:21:49.7	1.68	C	3
J0026.5-6639	00:26:34.15	-66:39:53.9	1.00	G	
J0026.5-6708	00:26:34.95	-67:08:14.0	5.21	G	
J0026.5-6725	00:26:31.40	-67:25:04.7	3.41	P	
J0026.6-6646	00:26:37.80	-66:46:03.5	2.70	G	
J0026.6-6659	00:26:38.46	-66:59:35.5	0.47	P	
J0026.6-6731	00:26:37.16	-67:31:06.0	1.89	G	
J0026.7-6632	00:26:46.00	-66:32:00.2	5.38	G	
J0026.7-6640	00:26:45.80	-66:40:06.7	0.56	P	
J0026.7-6647	00:26:46.38	-66:47:38.0	0.96	C	1
J0026.8-6631	00:26:48.72	-66:31:06.8	0.54	P	
J0026.8-6643	00:26:49.59	-66:43:59.8	8.79	C	3
J0026.8-6649	00:26:53.14	-66:49:36.4	0.99	P	
J0026.8-6659	00:26:48.56	-66:59:51.3	0.45	C	1
J0026.8-6714	00:26:50.49	-67:14:03.8	0.41	M	
J0026.9-6626	00:26:57.67	-66:26:18.8	1.95	G	
J0026.9-6652	00:26:59.90	-66:52:14.8	0.74	C	1
J0026.9-6706	00:26:55.16	-67:06:22.8	0.58	M	
J0026.9-6732	00:26:56.81	-67:32:15.8	0.52	P	

Table 4.2: The ATLAS survey 1.4 GHz Source Catalog

### 4.3 Source Counts

In this section, the ATLBS source counts are computed and the corrections necessary to estimate the true source counts from the distribution of ATLBS sources in flux density are discussed. First, the sources were binned in octave bins based on their integrated flux density. The effective bin centers need to be defined carefully because in a given bin the source counts are not expected to be uniformly distributed (in which case, the mean would suffice). The corrections that translate observed counts to true counts depend on this distribution within the bins and, hence, the effective bin center. The bin centers in this study have been calculated using the expression given by Windhorst et al. (1984):

$$S_{bc} = [(1 - \gamma) \left( \frac{S_l - S_u}{S_l^{1-\gamma} - S_u^{1-\gamma}} \right)]^{1-\gamma}, \quad (4.7)$$

where  $\gamma = 2.52 + 0.321 \times \log(S_{gc}) + 0.042 \times \log^2(S_{gc})$  and  $S_{gc}$  is the geometric center of the bin. The factor  $\gamma$  has been obtained by a fit to the source counts using a collection of data from Windhorst et al. (1984), therefore taking care of the source distribution within any bin. Additionally, the value of  $\gamma$  was estimated from the source counts which have been derived; the value of the slope thus estimated is consistent with the above value of the slope over most of the flux density range.

The blending correction to the counts is negligible due to the high angular resolution in ATLBS images, and it has been discussed in detail in a previous section. To assure completeness of the source counts, resolution bias correction, effective area correction and noise bias correction were applied; these are discussed

## 4. THE RADIO SOURCE COUNTS

---

below.

### 4.3.1 Corrections to the source counts

#### 4.3.1.1 Noise Bias Correction

Noise bias arises because the ‘true’ source counts are modified by the the noise in the image. This is true for estimations of any distribution affected by additive noise (Eddington, 1913); noise bias corrections have been applied previously to radio source counts (Murdoch et al., 1973; Richards, 2000; Bondi et al., 2008). Noise in the image effectively redistributes sources across neighboring bins, the magnitude of the effect depends both on the image noise and the intrinsic source distribution. If a particular bin has nearby bins with nearly the same numbers of sources, then the number of sources migrating into the bin and out of the bin are the same, assuming symmetric noise distribution. Additionally, at high flux densities, the contribution of image noise to the source flux density is small and is usually a small fraction of the bin size, which most often increases in geometric progression. Therefore, the effects of noise bias are important for the lowest few bins.

The effects of noise bias for the images were estimated using simulations. The polynomial fit to the radio source counts given by Hopkins et al. (2003) was used as a model for the true source distribution (It may be noted here that later in this chapter in Section. 4.4 an improved estimate of noise bias has been derived and resultant source counts using Eqn. 4.15, which is derived from the ATLBS

counts for self consistency). The polynomial fit is :

$$\log[(dN/dS)/S^{-2.5}] = \sum_{i=0}^6 a_i [\log(S/mJy)]^i, \quad (4.8)$$

with  $a_1 = 0.859$ ,  $a_2 = 0.376$ ,  $a_3 = -0.049$ ,  $a_4 = -0.121$ ,  $a_5 = 0.057$ ,  $a_6 = -0.008$ .

Noise of random amplitude, consistent with a Gaussian distribution with rms equal to that of the image noise, was added to the integrated flux density of the sources derived from the distribution, and the sources were rebinned. This gives an estimate of the noise bias correction required for each bin. The correction is significant only for the lowest two bins. For the first bin, 0.38 – 0.768 mJy, the correction to the source counts is 23.8% which drops to 3.6% for the second bin and for the third bin the noise bias correction is only 0.69%. The derived corrections have been applied to the source counts for the above bins since for other bins the correction is negligible.

#### 4.3.1.2 Effective Area Correction for Sources

Only sources that have peak flux densities (without gain correction) above the detection threshold and located in the area of the mosaic where the primary beam gain is above 0.5 are included in deriving the source counts. Approximately 17% of sources above the detection threshold lie outside this area. Since the primary beam gain varies over the mosaic image this leads to a bias in source detection because sources with higher peak flux densities are potentially detectable over a larger sky area. Sources with peak flux density above twice the detection threshold may be detected anywhere in the area mentioned above (since the maximum attenuation suffered would lower the peak flux densities above or at the detection threshold);

## 4. THE RADIO SOURCE COUNTS

---

whereas the sources with peak flux densities between the detection threshold and twice that value would be detectable only within a restricted area. The correction factor to account for the change in effective sky area with flux density may be estimated as the ratio of the effective area for a given peak flux density and the total detection area, assuming that sources are uniformly distributed on the sky.

### 4.3.1.3 Effective Area Correction for Blended Sources

For blended sources (or rather those sources which are blended in the low resolution image and have been found to be multiple distinct sources at high resolution), the peak flux density as well as the integrated flux density have been determined using the high resolution image. An effective area correction derived from the low resolution peak flux density may be incorrect in these cases because in many such cases sources with a large difference in peak flux density are blended together. Blended sources with individual peak flux densities above the detection threshold would have all been detected irrespective of blending. For these sources the high resolution integrated flux density was used to derive the effective area correction. Blended sources with peak flux densities below the detection threshold but with integrated flux density above the detection threshold would also have been detected since at low resolution the peak flux density (in most cases) would have been equal to the integrated flux density in the high resolution image. There are 37 sources with peak flux densities below the detection threshold but with the integrated flux density above the detection threshold. For these sources, therefore, the effective area correction was estimated using the high resolution integrated flux density. Blended sources with integrated and peak flux densities below the detection threshold are not included in the derivation of source counts.

#### 4.3.1.4 Resolution Bias Correction

Resolution bias is because extended sources that have integrated flux density above the threshold may have their peak flux density below the detection threshold; this would not happen in the case of an unresolved source of the same integrated flux density. Owing to this effect a number of extended sources are lost in the source detection process, biasing the source counts to preferentially represent unresolved sources. This effect has been mitigated by using low resolution images for initial source detection. Below is given the estimate of the resolution bias correction applicable to the source counts. The expression given by Windhorst et al. (1990) has been used to represent the angular size distribution of sources and thereby derive the resolution bias. The fraction of radio sources above an angular size  $\phi$  is given by :

$$h(> \phi) = \exp [ -\ln 2 (\phi/\phi_{med})^{0.62}], \quad (4.9)$$

where the expression for  $\phi_{med}$  (median angular size) is:

$$\phi_{med} = 2''.0 S_{1.4GHz}^{0.3} \quad (4.10)$$

with  $S_{1.4GHz}$  in mJy.

The relationship between angular size and ratio of integrated to peak flux density is

$$1 + (\phi/b_s)^2 = (S_{int}/S_{peak}). \quad (4.11)$$

#### 4. THE RADIO SOURCE COUNTS

---

For a fixed integrated flux density, a source would be on the threshold of being missed if its peak flux density is equal to the detection threshold; such a source has an angular size:

$$\phi_{max} = b_s \times [(S_{int}/(S_{threshold})) - 1]^{1/2}. \quad (4.12)$$

Here  $b_s = 50''$  is the angular size of the synthesized beam for the low resolution images,  $S_{threshold} = 0.38$  mJy is the detection threshold and  $S_{int}$  is the mean flux density for the source bin.

Therefore, the fraction of sources missing due to being resolved is:

$$h(> \phi) = \exp [ -\ln 2 (\phi_{max}/\phi_{med})^{0.62} ]. \quad (4.13)$$

Thus the resolution bias correction for each bin is calculated as:

$$c = 1/(1 - h(> \phi_{max})). \quad (4.14)$$

Since the beam FWHM in this case is  $50''$ , the resolution bias is only a small correction to the source counts. The maximum effect of the resolution bias is seen in the lowest bin, where an estimated 1.25% sources are lost due to the resolution bias. In higher flux density bins, the effect of resolution bias is negligible. For source counts generated solely with high resolution images, however, the resolution bias corrections can be significant.

## 4.4 A discussion on the slope and magnitude of the counts at sub-mJy flux densities

---

### 4.3.1.5 The ATLBS source counts

The total number of sources in the ATLBS survey above a threshold of 0.38 mJy is 1366; this is the final number of sources after using the high resolution image to identify blended sources in the low resolution image. The differential source counts, with all of the corrections discussed above, are shown in Fig. 4.3. The fit to the source counts from the Australia Telescope Hubble Deep Field-South survey (ATHDFS) of Huynh et al. (2005) as well as the source counts for the Australia Telescope ESO Slice Project (ATESP) survey of Prandoni et al. (2001) are overlaid for comparison. Here the fit for ATHDFS is for a compilation of source counts of radio surveys including FIRST (Faint Images of Radio Sky at Twenty-Centimeters; Becker et al. (1994)), PDF, ATHDFS and ATESP. There is good agreement between the ATLBS source counts and ATESP source counts. ATLBS source counts are, however, lower than the ATHDFS counts over most of the flux density range by about 10%. The ATLBS source counts derived herein based on high resolution followup of the ATLBS survey is consistent with earlier derivations of ATLBS source counts (Subrahmanyam et al., 2010), which were based on the low resolution images.

## 4.4 A discussion on the slope and magnitude of the counts at sub-mJy flux densities

The flattening in the normalized differential source counts widely reported in the literature is not obvious in the ATLBS source counts. To take a closer look at the

## 4. THE RADIO SOURCE COUNTS

---

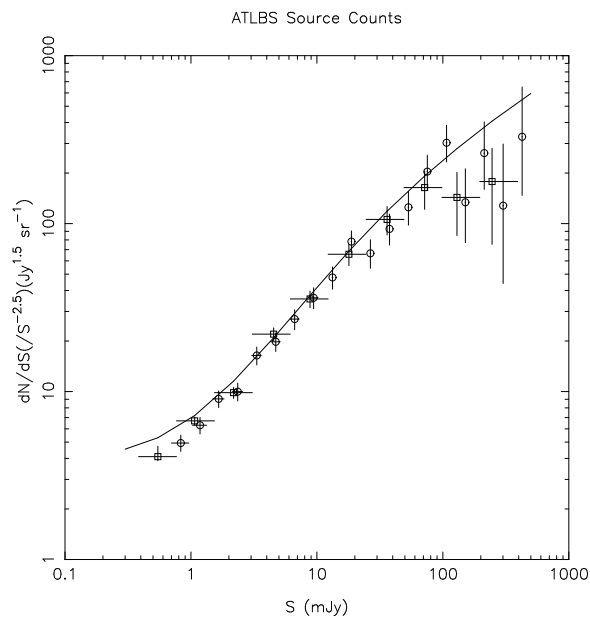


Figure 4.3: The normalized differential source counts for ATLBS are presented (using square symbols with associated error bars). The source counts for ATESP survey (Prandoni et al., 2001) (shown by circles) and the fit to the source counts for ATHDFS survey (Huynh et al., 2005) (continuous curve) are also depicted for comparison.

#### 4.4 A discussion on the slope and magnitude of the counts at sub-mJy flux densities

---

behavior of the ATLBS counts below about 1 mJy, the differential source counts have been estimates using binning with smaller bin sizes; these are displayed in Fig. 4.4. The ATLBS counts are consistent with the ATESP counts within the errors and continue the same trend to lower flux densities. However, the ATLBS counts appear not to follow the upturn of the ATHDFS counts and fall significantly short of the ATHDFS counts below about 1 mJy. In Fig. 4.4 the source counts from Simpson et al. (2006) have also been added for further comparison.

The ATHDFS survey catalog is reported to have been constructed as a source catalog as opposed to a component catalog (Huynh et al., 2005). However, the specific forms of the corrections applied to the source counts from the ATLBS and ATHDFS differ, which may explain the difference in the source counts in the two cases. Specifically, it may be noted that the corrections for noise bias are not applied to the source counts for ATHDFS as well as PDF survey (Hopkins et al., 2003). Since the sub-mJy counts are close to the detection threshold, the effect of noise bias is significant and needs to be applied to correctly estimate the source counts. In Fig. 4.4 are displayed the source counts for ATLBS, generated without applying the noise bias correction. It may be seen from the figure that in the absence of noise bias corrections, the differential source counts do exhibit a more pronounced flattening in the sub-mJy regime. Clearly, omitting noise bias corrections tend to generate flatter estimates for the source counts at levels close to the detection limit, and a factor responsible for the deficit in the ATLBS counts compared to those of the ATHDFS and PDF counts may be their having omitted the noise bias correction.

#### 4. THE RADIO SOURCE COUNTS

---

On the other hand, the radio source counts from Simpson et al. (2006) match rather well with the ATLBS source counts in the flux density range which has been explored in this work. The radio source counts of Simpson et al. (2006) have been derived from VLA 1.4 GHz observations of the Subaru/XMMNewton Deep Field (SXDF) over an area of 0.8 square degrees. The source counts presented in Simpson et al. (2006) have been corrected for the noise bias (Eddington Bias) which may be the reason for their radio source counts being at the lower end of the source counts reported in literature (see their Fig. 6). However, it should be noted that the source counts in Simpson et al. (2006) do show a change in the slope of differential source counts; this change, however is more prominent at lower flux densities than those which have been probed in this work.

#### 4.4 A discussion on the slope and magnitude of the counts at sub-mJy flux densities

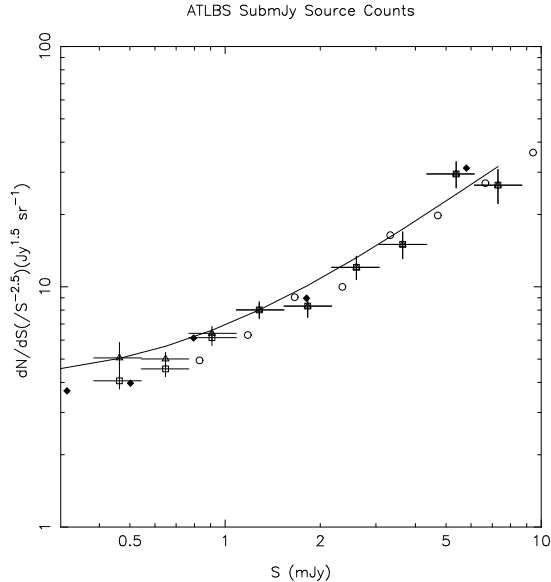


Figure 4.4: The ATLBS differential source counts with reduced bin widths. The squares represent the source counts corrected for noise bias and the triangles represent the source counts without noise bias correction. The filled diamonds represent the source counts from Simpson et al. (2006). The other symbols are same as that in Fig. 4.3.

Source counts derived from ‘component’ catalogs are expected to exhibit extra ‘sources’ at low flux densities, as extended sources are decomposed into components with relatively lower flux densities. Additionally, in the case of surveys done with high resolution, it is possible for extended sources to break up into two or more compact components if the connecting diffuse emission is missed in the imaging. As a demonstration, source counts have been from a component catalog generated from the ATLBS high resolution images (with beam FWHM of  $6''$ ). The catalog was generated using the MIRIAD task IMSAD, with a detection threshold of  $4\sigma$ , where  $\sigma = 72 \mu\text{Jy beam}^{-1}$  is the rms noise in the image, without

#### 4. THE RADIO SOURCE COUNTS

---

any attempt at constructing a ‘source’ catalog as has been done in this work. The source detection was restricted to regions with primary beam gain of 0.9, so that corrections for the attenuation due to the primary beam, and the effective area correction, may be neglected. The noise bias correction as well as the resolution bias correction (which is important in the case of images with high resolution) were separately derived for these counts in the same manner as described in earlier sections. In Fig. 4.6 the source counts generated from this component catalog are shown. As may be expected, this results in a substantially flatter distribution for the source counts; additionally, the source counts are now greater than before as well as greater than the ATHDFS counts. In Fig. 4.5 the ratio of component counts to source counts versus flux density are displayed. This ratio has an average value of 1.4 implying that on average the component counts are a factor 1.4 higher than the true source counts.

#### 4.4 A discussion on the slope and magnitude of the counts at sub-mJy flux densities

---

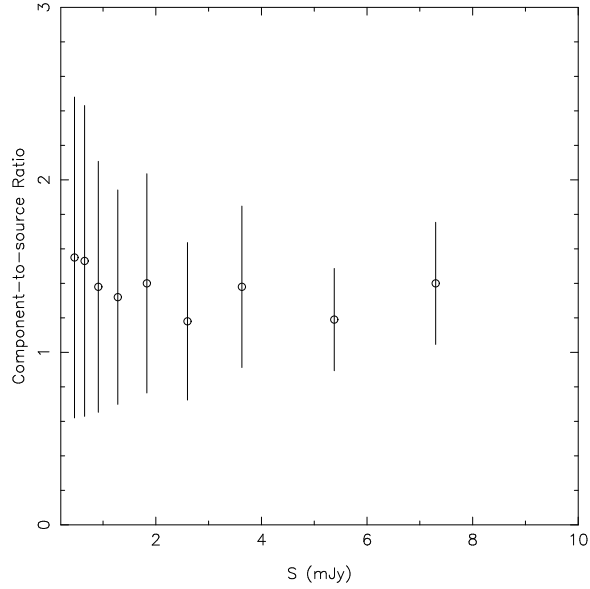


Figure 4.5: The component-to-source ratio as a function of flux density. Within errors the ratio is constant across the flux density bins.

The ATLBS counts are about 10% lower than the ATHDFS counts over the 0.4-10 mJy range. As seen in Fig. 4.6, a component catalog may overestimate the counts in this flux density range by as much as 30 – 50%; Hopkins et al. (2003) estimate that a component catalog may overestimate the counts by about 10%. The quantum of error would depend on the structures of radio sources at these flux densities and the quality of the imaging—the ability of the imaging to reproduce any connecting emission between components—and hence the correction factor necessary for deriving a source count from component counts may vary depending on the visibility coverage and imaging algorithms. Nevertheless, it may be concluded that the relatively lower source counts inferred in this work are in part owing to the ATLBS counts having been carefully prepared to represent a source catalog rather than a component catalog. Note that catalogs such as

#### 4. THE RADIO SOURCE COUNTS

---

NVSS are component and not source catalogs so any source count analysis based on these catalogs will have this problem. It is possibly for this reason that no source count analysis is included in the NVSS publication (Condon et al., 1998).

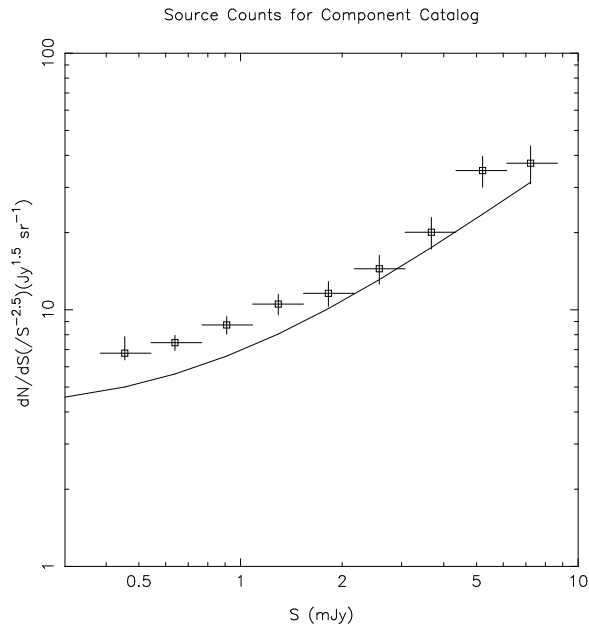


Figure 4.6: The normalized differential source counts for ATLBS, estimated using the high resolution images and a ‘component’ catalog. The continuous curve is the fit from ATHDFS. The sub-mJy counts show a pronounced flattening as well as counts higher than that from ATHDFS.

The noise bias correction depends on the assumption of what is the true source counts: this prior assumption is used to determine the true number of sources in each bin so that the effect of noise bias may be estimated. As discussed earlier, PDF source counts have been adopted for the determination of the noise bias. However, the PDF source counts show a more pronounced flattening compared to the ATLBS; therefore, a second iteration of noise bias correction using the derived ATLBS source counts has been carried out.

## 4.5 Summary and conclusions

$\Delta S$ mJy	$\langle S \rangle$ mJy	$dN/dS(/S_{-2.5})(Jy^{1.5}Sr^{-1})$	$(dN/dS)_{pdfnb}$	$dN/dS_{wonb}$
0.38 – 0.54	0.46	4.55(+0.76, –0.31)	4.06(+0.71, –0.30)	5.05(+0.81, –0.31)
0.54 – 0.77	0.65	4.76 ± 0.33	4.55 ± 0.33	5.00 ± 0.33
0.77 – 1.09	0.91	6.20 ± 0.45	6.14 ± 0.45	6.40 ± 0.44
1.09 – 1.54	1.28	7.90 ± 0.64	8.01 ± 0.64	8.02 ± 0.64
1.54 – 2.17	1.83	8.25 ± 0.85	8.31 ± 0.85	8.32 ± 0.85
2.17 – 3.07	2.60	12.05 ± 1.35	12.05 ± 1.34	12.05 ± 1.35
3.07 – 4.34	3.63	15.00 ± 1.92	15.01 ± 1.92	15.01 ± 1.92
4.34 – 6.14	5.38	29.48 ± 3.69	29.48 ± 3.69	29.49 ± 3.69
6.14 – 8.69	7.30	26.49 ± 4.30	26.49 ± 4.30	26.49 ± 4.30

Table 4.3: ATLAS 1.4 GHz source counts with a self-calibrated noise bias

A second order polynomial in flux density was fit to the ATLAS source counts derived above, which appears sufficient to express the features seen in source counts presented in this study. The polynomial fit is given by :

$$\log[(dN/dS)/S^{-2.5}] = 0.781 + 0.851 \times \log(S/mJy) - 0.066 \times \log^2(S/mJy). \quad (4.15)$$

Since the ATLAS source counts are relatively steeper compared to the PDF counts, the noise bias correction estimated from the ATLAS counts is smaller. For the lowest two bins 0.38-0.54 and 0.54-0.77 mJy, the noise bias correction is now derived to be 11.18% and 5.22% respectively, reduced from the previous values of 24.5% and 10%. This improved estimate of the source counts is shown in Fig. 4.7 and Table (4.3). The ATLAS source counts are still systematically lower than the ATHDFS source counts; however, the difference between the two source counts is reduced.

## 4.5 Summary and conclusions

In this chapter, a study of sub-mJy radio source counts for ATLAS survey is presented. The source catalog for ATLAS survey, the construction of which is

## 4. THE RADIO SOURCE COUNTS

---

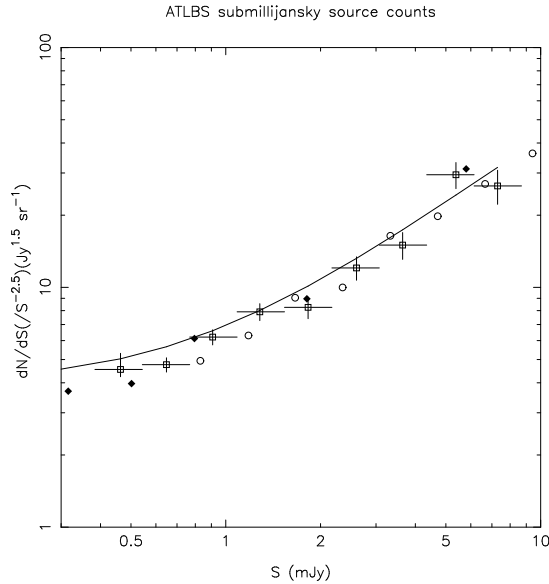


Figure 4.7: The differential source counts for ATLBS derived using noise bias correction derived from the ATLBS counts themselves. The other symbols are same as that in Fig. 4.4.

discussed above, is a carefully made source list as opposed to a component list. The source list has been generated using unique algorithms, multi-frequency and multi-resolution images, which simultaneously provides solutions for the issues of confusion and missing diffuse emission. The source list was used to estimate the radio source counts down to 0.4 mJy, which have been corrected for noise bias, resolution bias, and effective area. Comparing the counts with previous work - the ATHDFS and PDS counts - shows that the ATLBS counts are systematically lower and the upturn in sub-mJy source counts has not been found up to the flux densities probed. The work presented herein underscores the importance of noise bias correction, in particular for deriving counts close to the limit of the survey sensitivity and for correctly estimating the faint end slope and upturn in the source counts at sub-mJy flux density. Finally, the lack of an upturn in the source counts at faint flux densities implies that down to the faintest flux densi-

ties that have been probed (approximately 0.4 mJy) there is no evidence for any new population.

For generating the source list, the radio images were initially examined using automated algorithms, which used representations with different resolutions to identify sources and distinguish unresolved and single component sources and complex sources. All complex sources were carefully examined by eye to recognize blends and classify appropriately. Optical surveys of the ATLBS fields were also examined for candidate host galaxies to aid in the classification of complex sources. The integrated flux densities of the sources were derived in a variety of methods - the method appropriate for the source structural classification was adopted in each case. An emphasis is placed on the use of multi-resolution images, which may complement each other, as well as the need to use data from other wavebands such as optical, infrared etc. The source list is also presented online along with the integrated flux densities and classification.

The source list was used to estimate the radio source counts down to 0.4 mJy. The counts have been corrected for noise bias, resolution bias, and effective area. It may be noted that considerable care has been taken to ensure that the counts correspond to sources and not components. The counts presented in Fig. 4.7 and Table (4.3) above have been self-calibrated for the noise bias in that the counts derived in a first iteration have been used to derive the noise bias correction.

The systematically low counts for ATLBS are attributed to the ATLBS counts representing sources as opposed to components, as well as corrections for noise

#### 4. THE RADIO SOURCE COUNTS

---

bias. It has been demonstrated that the substantial difference in counts that results from using component catalogs as opposed to source catalogs: at 1 mJy flux density component counts may be as much as 50% above true source counts. This implies that automated image analysis for counts may be dependent on the ability of the imaging to reproduce connecting emission with low surface brightness and on the ability of the algorithm to recognize sources, which may require that source finding algorithms effectively work with multi-resolution and multi-wavelength data. The upturn in sub-mJy source counts reported in the literature may be due to a combination of small survey areas and identification of radio sources as opposed to components, as well as effects of noise bias close to the detection limit.

The source counts presented here form investigations into the fainter end of the radio source population. In the next chapter, the other end, i.e. powerful, extended sources are studied.

## Environments of Extended Radio Sources

### 5.1 Introduction

Examining the environments of radio galaxy hosts has been one of the aims of this thesis. Towards this goal as well as to obtain properties of the host galaxies multi-band optical observations were carried out, which were described in Chapter 3. A subset of extended radio sources detected in the ATLBS survey constitutes the extended source sample (ATLBS-ESS; Saripalli et al. (2012)); it contains radio galaxies observed to have the largest angular size and includes all sources with angular size  $> 30''$ . The examination of ATLBS-ESS source structures has yielded subsamples of restarted radio galaxy candidates,  $z > 0.5$  low-power radio galaxies, giant radio galaxies and other morphological types. The variety of radio structures detected and their relative abundance has been used to make inferences on the life cycles of radio sources. In this chapter the environments of the ATLBS-ESS radio sources are characterized.

## 5. ENVIRONMENTS OF EXTENDED RADIO SOURCES

---

Obviously, the gas environments in which radio sources reside and evolve ought to have a substantial influence on the structures that form; this expectation has been vindicated in many case studies where the radio structures have been compared with the X-ray gas environments (Blanton et al. (2011); Boehringer et al. (1993)). Numerous studies of the optical environments of radio galaxies have been carried out previously (Longair & Seldner, 1979; Yee & Green, 1984; Hill & Lilly, 1991; Zirbel, 1997). The motivation behind these studies has been to examine differences between different classes of radio sources, the evolution of environments with cosmic epoch as well as the possibility of identifying clusters/groups of galaxies using radio sources as a tracer (Wing & Blanton, 2011).

Several studies have found that the environments of FRI/FRII sources are different, and have a redshift dependence. Although FRI sources are found in richer environments, FRII sources at low redshifts are mostly observed to be hosted by field galaxies, where as at relatively higher redshifts ( $z > 0.5$ ) the FRII environments appear to be richer (Hatch et al., 2011; Best et al., 2003; Overzier et al., 2008). There have been fewer studies that relate the richness of the environments and morphological asymmetries of radio galaxies. Investigations by Subrahmanyan et al. (2008) and Safouris et al. (2009) are noteworthy in this regard where the radio structures of two giant radio galaxies were examined in the context of the large-scale galaxy distributions in their vicinity (also see Chen et al. (2012) and references therein). The study was also used to infer properties of the ambient thermal gas medium in which the structures evolved. Clear correlations between structural asymmetries and associated extended emission-

line gas were also found for radio galaxies that have relatively smaller sizes of a few hundred kpc (McCarthy et al., 1991).

## 5. ENVIRONMENTS OF EXTENDED RADIO SOURCES

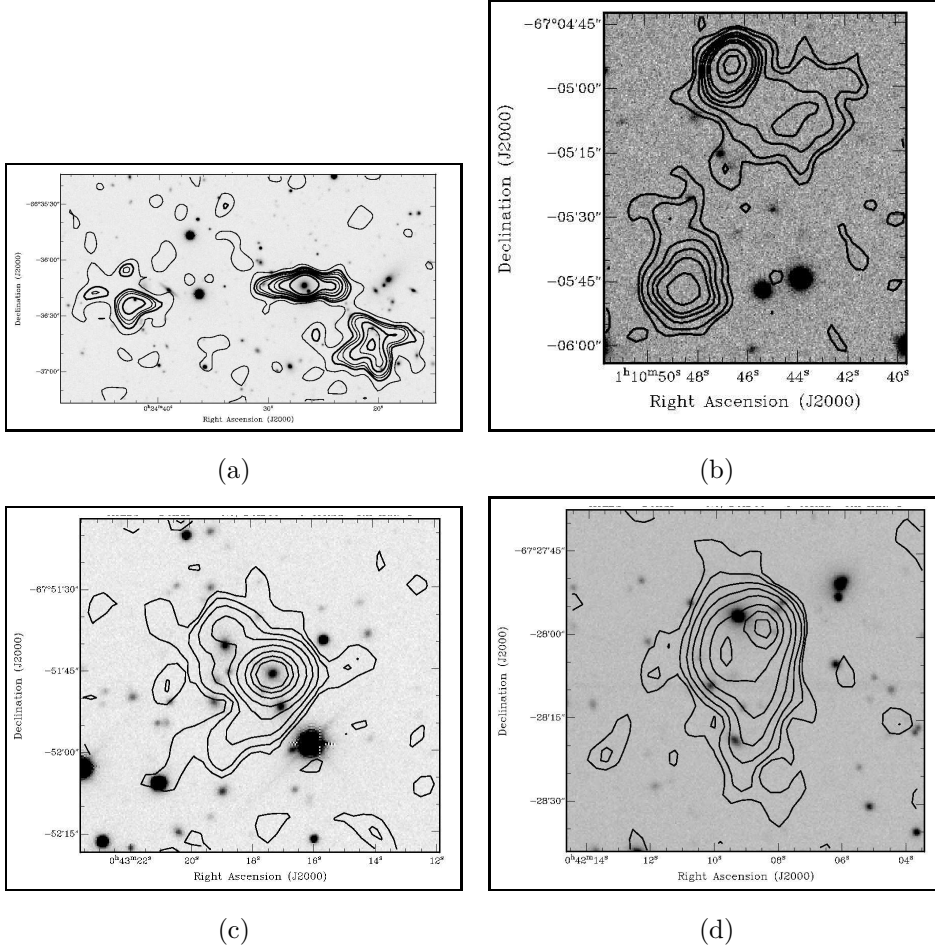


Figure 5.1: (a) The radio source J0024.4–6636, a FRI source. The source is also an asymmetric source. The radio contours are at  $1, 2, 2.5, 3, 4, 5, 6, 8 \times 10^{-4} \text{ Jy beam}^{-1}$  (b) The radio source J0110.7–6705, a FRII source. The radio contours are at  $1, 2, 4, 6, 8, 12, 16, 32, 48 \times 10^{-4} \text{ Jy beam}^{-1}$ . (c) The radio source J0043.2–6751, a WAT source. The radio contours are at  $1, 2, 4, 8, 16, 32, 48, 64 \times 10^{-4} \text{ Jy beam}^{-1}$  (d) The radio source J0042.1–6728, a HT source. The radio contours are at  $1, 2, 4, 8, 16, 32, 48, 64 \times 10^{-4} \text{ Jy beam}^{-1}$ . The grayscale in each of the above is optical taken from SDSS  $r'$  band images, described in 3. The examples of the sources given here show the same sources and follow the same contours as Figs. 1.5 (right panel), 1.117, 1.48 and 1.47 from Saripalli et al. (2012).

The outline of this Chapter is as follows. In the next section, the sample definition and selection process is described. In Section 5.3, the redshift-magnitude relation is derived that has been subsequently used to estimate redshifts for those sources in the sample that lack spectroscopic redshift measurements. Section 5.4 presents a description of the method adopted to quantify the environmental richness and spatial distribution relative to the radio axis. The last section is a presentation and discussion of the results of the study. A  $\Lambda$ CDM cosmology with  $H_o = 71 \text{ km s}^{-1} \text{ Mpc}^{-1}$  and  $\Omega_\Lambda = 0.73$  has been adopted.

## 5.2 Sample Definition and Selection

This study of the environments of radio sources from the ATLBS survey is restricted to those that are extended and hence to a subset of the ATLBS-ESS sources. Briefly, the ATLBS-ESS subsample consists of 119 radio sources that have angular size exceeding  $0'.5$ . All sources where no magnitude or redshift information is available have been omitted. Additionally, since radio galaxies at high redshifts may suffer from greater incompleteness in the detection of neighboring galaxies, a redshift cut has been imposed, choosing only sources below redshift of  $z = 1$ . Moreover, those sources near the edges of the optical images in which consequently the environmental information is truncated in sky projection are rejected: in practice sources within a linear distance of 0.5 Mpc of the image edge have been rejected (for more discussion on this see Section 5.4.2).

The final sample of sources chosen for the environment study has 43 sources

## 5. ENVIRONMENTS OF EXTENDED RADIO SOURCES

---

(Fig. 5.1 presents images of sources of different morphologies from the selected sample). In Table 5.2 this source list is presented. For these most extended of ATLBS radio sources, with good structural information and hence well classified morphology, an attempt has been made to examine the environments in relation to different source classifications and radio structure.

### 5.3 Redshift-magnitude relation

A study of the galaxy environments of ATLBS radio sources requires estimates for their redshifts. Since only a fraction of the host galaxies of the ATLBS radio sources have spectroscopic redshifts, a redshift-magnitude relation for the host galaxies of ATLBS sources has been derived here, which has been used in subsequent sections that explore the galaxy environments.

The ATLBS-ESS sample (Saripalli et al., 2012) was selected based on the angular size of the sources. Of this sample, only 19 radio galaxies have good quality redshift measurements as well as optical magnitudes. To have additional data for deriving a better fit for the relation, 61 ATLBS sources have been included that were relatively compact and hence not in the ATLBS-ESS list. These are ATLBS radio galaxies that have good quality redshifts available from on-going AAOmega observations (Johnston et al., in preparation). Quasars have been omitted while assembling this sub-sample for deriving the magnitude-redshift relation since their optical magnitudes may be dominated by the AGN at the center. Most of the sub-sample of radio galaxies have redshifts in the range 0.2–0.5. The sources

## 5.4 Quantifying the galaxy environments of extended radio sources

utilized to derive the redshift-magnitude relation are presented in Table. 5.1.

Examining the  $r - z$  plot for these sources, it was seen that 20 of the sources were systematically offset from the principal clustering in the  $r - z$  plot. Some of these outliers were spirals or showed spiral-like features; the remainder, though ellipticals, showed clear signs of disturbed optical morphology. Excluding these, there were 80 sources in all that were used to estimate the magnitude-redshift relation.

A fit has been attempted for coefficients of the equation

$$m_r = a \times \log_{10}z + b. \quad (5.1)$$

The fit yielded parameter values  $a = 5.752$  and  $b = 21.82$ , with an rms error of 0.09. These may be compared with corresponding values of  $a = 5.3$  and  $b = 21.05$  derived by Eales et al. (1997) for  $R$  band, and  $a = 5.917$  and  $b = 21.65$  derived by Gendre et al. (2010) from the  $r'$  band data of the CONFIG survey. In Fig. 5.2 the fitted relation is also plotted along with the data.

## **5.4 Quantifying the galaxy environments of extended radio sources**

While there are many methods in the literature for measuring the environmental richness of extragalactic sources (see Gal (2008) for a review), most rely on the availability of redshifts. When working with a photometric catalog however,

## 5. ENVIRONMENTS OF EXTENDED RADIO SOURCES

---

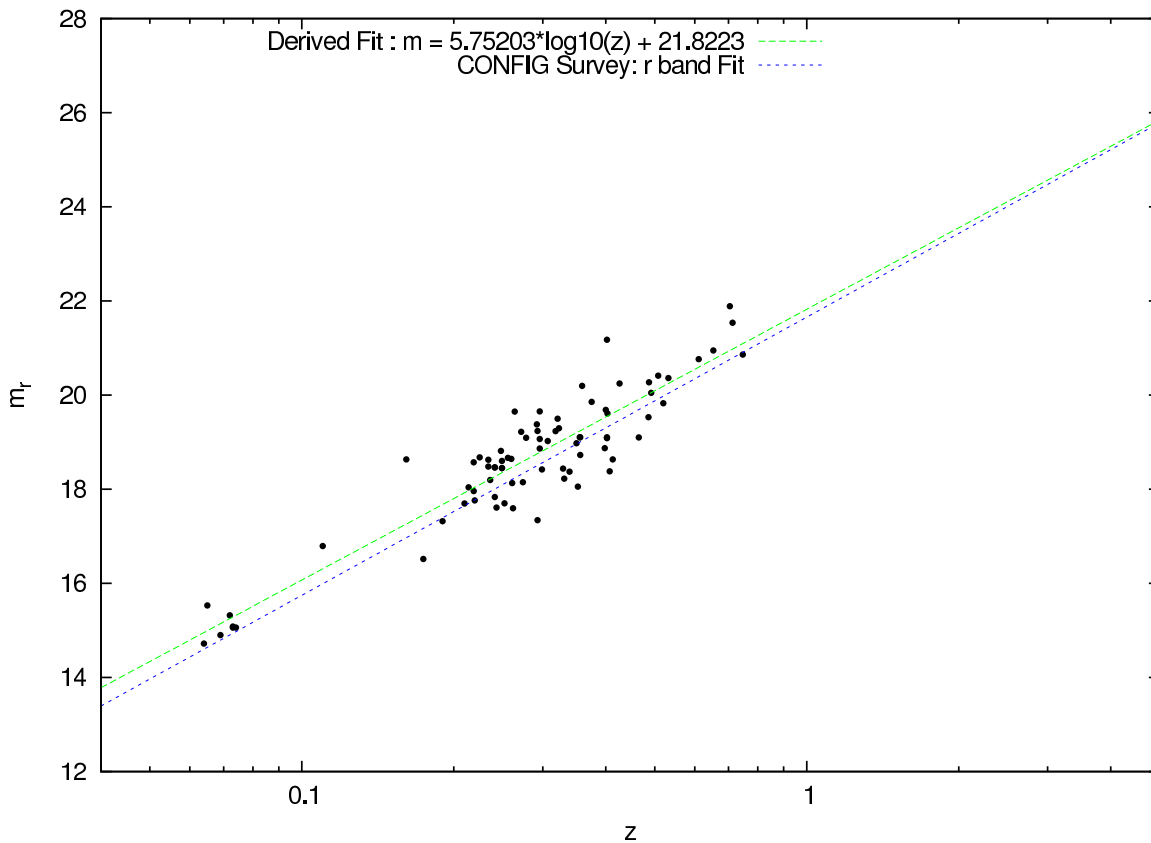


Figure 5.2: The fitted magnitude-redshift relation is shown as lines along with the data points used in deriving the fits; the data points correspond to the compilation of ATLBS radio galaxies with redshift measurements. The average error in  $z$  from this relation is 0.09. For comparison, the relation derived by Gendre et al. (2011) (CONFIG Survey) is also shown.

## 5.4 Quantifying the galaxy environments of extended radio sources

RA (J2000)	Dec (J2000)	RA (Id) (J2000)	DEC (Id) (J2000)	Redshift	$m_r$
0:22:45.10	-66:53:06.3	0:22:45.10	-66:53:06.3	0.234	18.48
0:26:14.33	-66:45:55.1	0:26:14.41	-66:45:54.9	0.426	20.25
0:26:21.47	-67:13:41.6	0:26:21.54	-67:13:41.7	0.249	18.45
0:26:21.47	-67:13:41.6	0:26:21.54	-67:13:41.7	0.249	18.45
0:26:28.92	-67:21:49.6	0:26:28.52	-67:21:48.8	0.274	18.15
0:26:49.08	-66:31:22.0	0:26:49.10	-66:31:23.0	0.323	19.3
0:26:49.18	-66:44:00.8	0:26:49.09	-66:44:01.1	0.219	17.96
0:27:15.59	-66:24:18.5	0:27:15.59	-66:24:18.1	0.073	15.06
0:27:15.60	-66:24:18.7	0:27:15.50	-66:24:18.6	0.074	15.06
0:27:46.63	-67:49:51.9	0:27:46.64	-67:49:52.5	0.174	16.52
0:27:56.29	-67:37:53.8	0:27:56.28	-67:37:53.8	0.252	17.7
0:28:08.51	-66:14:15.9	0:28:08.55	-66:14:16.5	0.272	19.22
0:28:09.84	-66:29:38.8	0:28:09.73	-66:29:39.0	0.339	18.37
0:28:22.42	-66:53:44.1	0:28:22.41	-66:53:43.5	0.190	17.32
0:28:29.45	-67:18:43.6	0:28:29.47	-67:18:44.3	0.243	17.61
0:28:33.98	-67:21:50.2	0:28:33.98	-67:21:50.3	0.241	17.83
0:28:41.04	-66:43:45.1	0:28:41.19	-66:43:44.5	0.234	18.62
0:28:51.94	-67:58:39.3	0:28:52.02	-67:58:39.9	0.352	18.05
0:29:02.47	-66:39:51.6	0:29:02.65	-66:39:51.9	0.219	18.57
0:29:04.64	-66:03:20.4	0:29:04.58	-66:03:21.4	0.400	19.69
0:29:07.17	-67:22:56.4	0:29:07.12	-67:22:55.6	0.220	17.76
0:29:25.65	-67:21:30.7	0:29:25.55	-67:21:31.5	0.292	19.38
0:29:44.03	-66:56:23.4	0:29:43.95	-66:56:23.3	0.402	19.09
0:29:52.63	-66:06:53.2	0:29:52.98	-66:06:53.5	0.402	21.18
0:30:01.70	-67:14:02.2	0:30:01.69	-67:14:03.3	0.413	18.63
0:30:09.02	-67:26:44.9	0:30:09.18	-67:26:45.1	0.713	21.54
0:30:44.21	-67:36:10.6	0:30:44.32	-67:36:11.1	0.321	19.5
0:31:14.79	-67:18:02.0	0:31:14.68	-67:18:01.5	0.501	20.64
0:31:17.26	-67:50:52.3	0:31:17.12	-67:50:53.2	0.375	19.86
0:31:29.22	-66:55:16.9	0:31:29.37	-66:55:16.8	0.532	20.36
0:31:32.05	-67:48:58.7	0:31:32.49	-67:49:01.1	0.355	19.1
0:31:32.48	-67:49:00.4	0:31:32.50	-67:49:00.5	0.356	19.1
0:31:47.04	-66:20:50.6	0:31:47.05	-66:20:50.4	0.278	19.09
0:31:55.80	-66:44:05.8	0:31:55.81	-66:44:05.1	0.653	20.95
0:32:01.00	-66:44:06.7	0:32:00.86	-66:44:06.4	0.611	20.76
0:32:45.72	-66:29:12.1	0:32:45.69	-66:29:11.9	0.214	18.04
0:33:29.46	-67:14:20.2	0:33:29.35	-67:14:19.2	0.407	18.38
0:33:46.81	-67:38:03.3	0:33:46.69	-67:38:04.7	0.356	18.73
0:33:47.32	-68:00:50.4	0:33:47.48	-68:00:49.8	0.225	18.68
0:33:56.56	-66:52:05.7	0:33:56.48	-66:52:05.4	0.402	19.1
0:34:05.59	-66:39:34.5	0:34:05.59	-66:39:34.5	0.110	16.79
0:34:08.85	-66:26:21.7	0:34:08.98	-66:26:21.7	0.486	19.53
0:34:29.18	-66:45:35.7	0:34:29.19	-66:45:35.6	0.403	19.61
0:34:33.18	-67:36:26.8	0:34:33.12	-67:36:28.4	0.069	14.9
0:34:57.51	-66:30:29.8	0:34:57.44	-66:30:29.6	0.487	20.27
0:35:02.08	-66:12:52.2	0:35:01.97	-66:12:52.5	0.465	19.1
0:35:05.24	-67:41:14.4	0:35:05.08	-67:41:14.5	0.072	15.32
0:35:34.52	-66:07:24.4	0:35:34.55	-66:07:25.6	0.264	19.65
0:35:35.41	-66:56:20.7	0:35:35.33	-66:56:20.0	0.296	19.65
0:35:35.85	-66:18:44.3	0:35:35.80	-66:18:44.3	0.508	20.41
0:36:58.16	-66:34:16.3	0:36:58.17	-66:34:16.4	0.241	18.46
0:36:58.16	-66:34:16.3	0:36:58.17	-66:34:16.4	0.241	18.46

Table 5.1: Sources used to fit the magnitude-redshift relation. Column 1 and 2 give the RA and Dec (J2000) of each source, Columns 3 and 4 give the same for the optical ID for each radio source. Column 5 and 6 give the redshift and magnitude for each source.

## 5. ENVIRONMENTS OF EXTENDED RADIO SOURCES

---

RA (J2000)	Dec (J2000)	RA (Id) (J2000)	DEC (Id) (J2000)	Redshift	$m_r$
0:37:29.07	-67:02:50.8	0:37:29.06	-67:02:50.3	0.350	18.98
0:39:01.31	-67:49:43.7	0:39:01.39	-67:49:43.5	0.073	15.08
0:39:03.72	-66:54:36.6	0:39:03.69	-66:54:34.7	0.256	18.66
0:40:44.35	-67:24:32.4	0:40:46.67	-67:24:35.8	0.296	19.07
0:40:55.50	-66:50:16.1	0:40:55.46	-66:50:16.5	0.747	20.86
0:41:00.98	-67:24:32.3	0:41:01.05	-67:24:33.0	0.299	18.42
0:41:12.20	-67:51:22.2	0:41:12.33	-67:51:22.1	0.359	20.2
0:41:20.87	-67:08:06.8	0:41:20.92	-67:08:05.2	0.492	20.05
0:41:46.39	-67:26:27.5	0:41:47.29	-67:26:26.8	0.293	17.34
0:41:46.80	-67:26:15.4	0:41:46.80	-67:26:15.4	0.293	19.24
0:41:58.21	-66:54:11.6	0:41:58.46	-66:54:11.0	0.520	19.83
0:42:01.69	-67:29:00.8	0:42:01.83	-67:29:03.0	0.296	18.87
0:42:14.21	-66:54:49.4	0:42:14.25	-66:54:48.6	0.161	18.63
0:42:23.49	-66:25:27.9	0:42:23.51	-66:25:28.1	0.210	17.7
0:43:08.54	-66:35:33.2	0:43:08.59	-66:35:33.9	0.318	19.23
0:52:06.50	-66:22:51.9	0:52:07.18	-66:22:55.8	0.704	21.89
0:56:57.22	-66:32:38.8	0:56:57.22	-66:32:38.8	0.249	18.6
0:57:04.57	-67:34:11.8	0:57:04.41	-67:34:12.8	0.307	19.02
0:57:07.00	-66:32:41.4	0:57:07.00	-66:32:41.4	0.248	18.81
0:57:12.34	-66:51:17.5	0:57:06.98	-66:50:59.0	0.236	18.2
0:57:27.20	-67:03:20.9	0:57:27.23	-67:03:18.9	0.260	18.64
0:57:43.62	-67:01:36.2	0:57:43.62	-67:01:36.2	0.261	18.13
0:57:48.60	-67:02:25.1	0:57:48.60	-67:02:25.1	0.064	14.72
1:02:41.48	-67:34:03.1	1:02:41.48	-67:34:03.1	0.065	15.53
1:03:10.45	-66:32:21.2	1:03:09.93	-66:32:21.1	0.398	18.87
1:03:14.16	-66:14:40.0	1:03:14.97	-66:14:24.9	0.331	18.22
1:03:44.44	-67:47:52.4	1:03:44.58	-67:47:52.0	0.329	18.44
1:06:01.66	-66:53:37.0	1:06:01.85	-66:53:37.1	0.262	17.6

Table 5.1: Table. 5.1 continued.

#### 5.4 Quantifying the galaxy environments of extended radio sources

where redshifts are not available for most galaxies, there are fewer methods available for estimating the environmental richness. One of the more common methods used with photometric catalogs is the counts-in-a-cell method, which was used by Abell (1958) to estimate richness of clusters. In this method the over-density of galaxy counts relative to a mean background density of galaxies is estimated. In determining the environments of radio galaxies, Hill & Lilly (1991), for example, used a variant of this method. However, the latter method has the disadvantage that the galaxies counted in a chosen volume (for example near a radio source) would include contamination from galaxies along the line of sight. Additionally, the selected volume may not sample the cluster fully, either in spatial or luminosity (*i.e.*, magnitude) range. The above method gives good estimates of the environmental richness in cases where clusters are *a priori* known to exist; however, for the purpose of the blind study presented herein, which involves estimating environmental richness for regions with no *a priori* information available, it may not be useful. Another method that has been used for estimation of environmental richness is that using the galaxy-galaxy two-point correlation function (Hardcastle, 2004), which has been used to detect galaxy clustering around any specified point of interest. The two-point correlation method has the advantage of not being dependent on a particular form for the structure (*e.g.* galaxy cluster).

In the work presented here, the method of spatial filtering as put forward by Postman et al. (1996) (P96 henceforth) has been used. This method gives the large-scale environment of the source under examination in the form of a map as opposed to quantifying the environmental richness at specific points (e.g. host galaxy location). This enables a characterization of environmental anisotropy on

## 5. ENVIRONMENTS OF EXTENDED RADIO SOURCES

---

the sky relative to the projected geometry of the source.

### 5.4.1 Description of the Method

The spatial filter method, which has been devised for use when only photometric information is available, is as follows. A smoothed galaxy map is created by using a convolving function, which is a composite of two filters: a spatial filter and a magnitude filter. The filters are chosen so as to match the density profile of a galaxy cluster and the luminosity function.

The spatial filter is the projected cluster radial profile. The form of the radial filter is given by Eqn. 19 from P96:

$$\begin{aligned} P(r/r_c) &= \frac{1}{\sqrt{1 + (r/r_c)^2}} \\ &\quad - \frac{1}{\sqrt{1 + (r_{co}/r_c)^2}} \quad \text{for } r < r_{co} \\ &= 0 \quad \text{otherwise,} \end{aligned} \tag{5.2}$$

where  $r_c$  is the cluster core radius and  $r_{co}$  is the cutoff radius. In literature, a choice of  $1h^{-1}$  Mpc for the cluster cutoff radius has been made, and the core radius has been adopted to be a factor of 10 smaller at  $100h^{-1}$  kpc (P96 and references therein; Kim et al. (2002)). The cutoff radius is more important in determining the efficiency in the detection of clusters, compared to the actual form of the radial filter (Kim et al., 2002). The smoothing is essentially a spatial filter that rejects structures with scale size well below the cutoff radius; therefore,

## 5.4 Quantifying the galaxy environments of extended radio sources

a somewhat smaller cutoff radius of 0.5 Mpc has been used so as to retain galaxy distribution structures corresponding to relatively poorer clusters. Following P96, a core radius that is a factor of 10 smaller than the cutoff radius has been used:  $r_c = 50$  kpc.

The magnitude filter has been chosen to be a Schechter luminosity function with the following form:

$$\phi \propto 0.4 \times \ln(10) 10^{-0.4(m-m_c)(\alpha+1)} e^{-10^{-0.4(m-m_c)}}. \quad (5.3)$$

The adopted values in this study are  $\alpha = -1.03$  and  $m_c$ , the characteristic magnitude of the luminosity function, is adopted to be  $-20.6$  (in absolute magnitude units); these are values typical for galaxy clusters (Popesso et al., 2005).

The matched filtering essentially creates a smoothed image optimized for the detection of clusters whose properties match the filter characteristics. Galaxy clustering structure with properties that deviate from the chosen model would be represented in the smoothed image with reduced prominence. The smoothed image represents the likelihood that a cluster is present at each pixel location and at the redshift of the host galaxy.

A few drawbacks of the method may be pointed out here. The form of the smoothing filter is assumed a priori. This means that any over-densities in the environments that have a form that deviates substantially from the filter, such as a filamentary structure, will be represented with smaller significance. An accu-

## 5. ENVIRONMENTS OF EXTENDED RADIO SOURCES

---

rate estimate of the galaxy background (a detailed description of the background is in Section 5.4.2 below) is required as a correction to the counts; the background may contain galaxies from both cluster as well as non-cluster galaxies and non-uniformity in the distribution may result in errors in the estimate of the background. This does not cause problems provided the optical images are large and clusters occupy small sky area; however, in smaller images where clusters may be dominant over non-cluster or field galaxies, the erroneous estimate of the background may give incorrect results for the inferred structure at the redshift of interest. The optical  $r'$  band images used herein have a fairly large size ( $37' \times 37'$ ), which obviates the latter concern.

An issue that merits mention here is that the redshift dependence of the core and cutoff radius has not been taken into account, as also the absolute characteristic magnitude of the cluster or their radial profiles; the clusters at high redshifts may have substantially different parameters compared to those that have been used.

### 5.4.2 Implementation of the Method

In this section the nomenclature used by P96 has been used. The output smoothed image is evaluated with a sampling that is sparse relative to the input image; the output image is evaluated at its ‘pixels’ as a weighted summation over the input image:

$$S(i, j) = \sum_{k=1}^{N_{gal}} P[r_k(i, j)]L(m_k), \quad (5.4)$$

## 5.4 Quantifying the galaxy environments of extended radio sources

where  $L(m_k)$  corresponds to:

$$L(m) = \frac{\phi(m - m_c)}{b(m)} = \frac{\phi(m - m_c)10^{-0.4(m-m_c)}}{b(m)}. \quad (5.5)$$

In the above equation,  $b(m)$  is the ‘background’ surface density of galaxies and the factor  $10^{-0.4(m-m_c)}$  has been introduced to keep  $L(m)$  integrable (see P96). The sum is evaluated at pixels of the output image denoted by the indices (i, j) and the index k is over all the galaxies in the field ( $N_{gal}$  is the total number of galaxies in the field).  $r_k$  is the distance from the position of the output pixel to the position of the galaxy with index k; this galaxy has an apparent magnitude ‘ $m_k$ ’.

The various terms in the sum  $S(i, j)$  are calculated as follows. For a given radio source for which the environmental richness is to be quantified, a unique smoothed map (see Fig. 5.3) is created that depends on the source redshift. The characteristic apparent magnitude, the characteristic radius and the cutoff radius for the image corresponding to any radio source depend on its redshift. The characteristic apparent magnitude is determined from the characteristic absolute magnitude using the relation:  $M_c = m_c - DM - K$ , where  $DM$  is the distance modulus and  $K$  is the k-correction appropriate to the redshift of the source. The k-correction for sources below redshift of 0.7 was based on the analytical expressions of Chilingarian et al. (2010) for SDSS r’ band. The luminous red galaxy (LRG) template results have been used for the galaxies, which gives k-correction as a function only of redshift, and yields results similar to

## 5. ENVIRONMENTS OF EXTENDED RADIO SOURCES

---

that derived by Fukugita et al. (1995) for elliptical galaxies. Beyond redshift of 0.7 the k-correction given by Metcalfe et al. (1991) using galaxy colors given by Fukugita et al. (1995) were used. The distribution function  $b(m)$ , which is supposed to be the ‘background’ galaxy counts, is taken to be simply the number counts for galaxies in the field that are fainter than magnitude  $m$ . This is because it is not known *a priori* which galaxies belong to the background as opposed to clusters.

The normalization for the sum is determined using the following equations (equations 20 and 21 of P96):

$$\int_0^{\infty} P(r/r_c)2\pi r dr = 1 \quad (5.6)$$

and

$$\int_0^{m_{\text{lim}}} \phi(m - m_c)10^{-0.4(m - m_c)} dm = 1. \quad (5.7)$$

Here the radial integration is truncated at the cutoff radius due to the form of  $P(r)$ . The integration over magnitudes is limited by the limiting magnitude  $m_{\text{lim}}$  of the survey. The normalizations of the radial and magnitude filter produce a background level of unity in the smoothed map (see P96). Therefore, on normalizing, the pixels are expected to have a centrally concentrated distribution about unity, with values exceeding unity representing over-densities. Pixel distributions covering a large range were obtained, with a tail towards positive values. The mode of the distribution is close to unity, and depends on the specific galaxy distribution in the image.

## 5.4 Quantifying the galaxy environments of extended radio sources

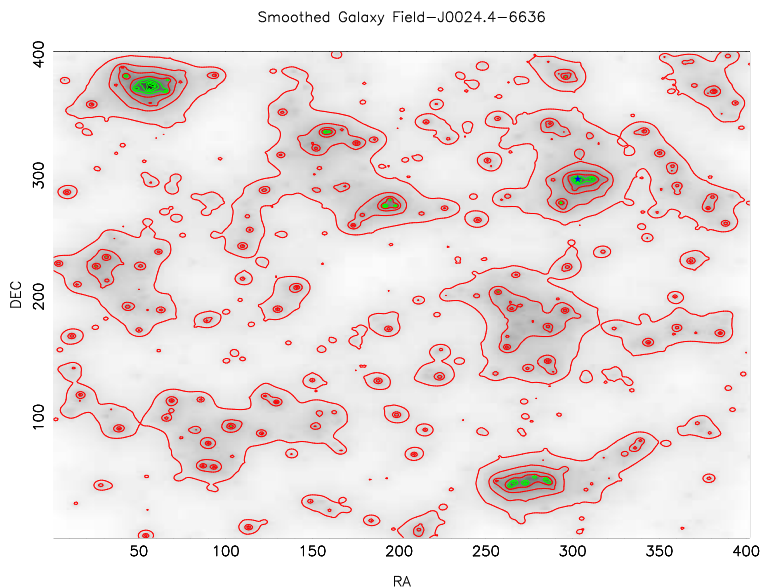


Figure 5.3: A smoothed map of the environment of the source J0024.4–6636, where the position of the radio source is shown by a blue star. The grayscale and contours show the overdensity of the environment, with the green contours showing the highest overdensity. The RA and DEC are given in pixel coordinates where 1 pixel = 5''.

Initially a catalog of galaxies (objects that have stellarity index less than 0.4) was made from the optical image excluding those sources within 200 image pixels from the edge to avoid these regions of higher image noise. Smoothed images with grid size between half the core radius to twice the core radius yields similar results (see P96); therefore, it was chosen to compute the summation above on a grid of pixels spaced by a distance corresponding to the core radius.

### 5.4.3 Parameters quantifying radio source environment

To examine the environments of the radio sources, parameters have been constructed which quantify the environmental over-density and its distribution in

## 5. ENVIRONMENTS OF EXTENDED RADIO SOURCES

---

the vicinity of the radio source. For each source, a radio axis vector has been defined whose direction is taken to be the direction of the longer radio lobe. The angle made by the longer radio lobe with the east-west direction, measured from north to east is designated as the PA (position angle) of the source. For Wide Angle Tailed (WAT) and Head-Tail (HT) sources, the bisecting direction instead of the direction of the larger lobe is used to define the radio axis in this study. With the radio axis as reference, the smoothed map is resampled.

A circle of 0.5 Mpc radius is constructed centered at the host galaxy of the radio source and this circular region is further divided into annular rings 100 kpc wide. Along the circumference of each annular region 16 new equidistant grid-pixels are generated at constant angular distance from each other and at constant distance from the host galaxy. The smoothed image values at the new grid-pixels are calculated by interpolating using neighboring pixels from the original smoothed map. For the annular region defined by each ring 5 quantities are calculated:

$$a_k = \frac{\sum S_i f_k}{\bar{a}_1}, \quad (5.8)$$

where the summation is over index ‘i’; *i.e.*, over the new grid pixels in the annular region. The functions  $f_k$  that weight the values of the pixels are 1,  $\sin(\theta_i)$ ,  $\cos(\theta_i)$ ,  $\sin(2\theta_i)$  and  $\cos(2\theta_i)$  for, respectively,  $k = 1, 2, 3, 4$  and 5. The argument of the functions is given by  $\theta_i = \theta_{ia} + \pi/2$ , where the angle  $\theta_{ia}$  is the angle of the  $i^{\text{th}}$  grid-pixel as measured from the radio axis defined above and  $S_i$  is the value at the grid pixel. The first quantity simply gives a measure of the over-density in the environment of the radio source. The other four quantities provide informa-

#### 5.4 Quantifying the galaxy environments of extended radio sources

tion regarding the dipole and quadrupole anisotropy in the environment of the source. All the quantities are normalized by the average of the  $a_1$  estimated for the different annuli for each source.

## 5. ENVIRONMENTS OF EXTENDED RADIO SOURCES

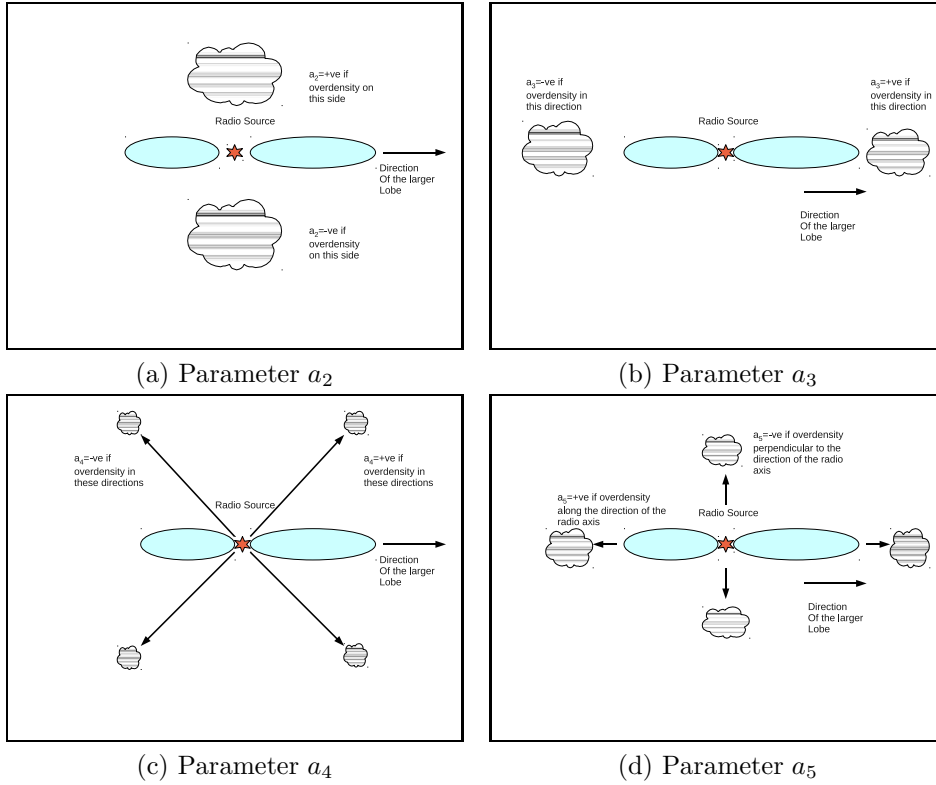


Figure 5.4: The figure above give schematic depiction of the overdensity parameters  $a_2$ - $a_5$  (Panels a-d).

The ‘a’ parameters represent Fourier components of the angular distribution of galaxy overdensity or, more specifically, the amplitudes of a Fourier harmonic decomposition of angular distributions in galaxies about the radio axis. A schematic depiction of the parameters  $a_2 - a_5$  is given in Fig. 5.4.

The  $a_1$  parameter is the mean overdensity and is the amplitude of the zeroth Fourier component. The  $a_2$  and  $a_3$  parameters are the fractional side-to-side asymmetry in the galaxy distribution; if the angular distribution follows a dipolar asymmetry then this quantity is unity and the two coefficients  $a_2$  and  $a_3$  as well as their signs give the direction of the dipole in the 2D sky plane. The  $a_4$  and

$a_5$  parameters are the quadrupolar anisotropy and are the Fourier components of the next order terms.

The errors in these parameters for any source are calculated by sampling different regions of the smoothed map containing the source and constructing the parameters  $a_k$  in those randomly offset regions. This procedure is repeated at 100 random positions offset from each source. As shown above, the quantities  $a_k$  are weighted sums of the pixel values in the vicinity of each source. Therefore, it has been chosen to normalize each quantity by the mean of the first parameter  $a_1$ , which represents the average over-density in the smoothed map. The standard deviations of the five parameters obtained by the above process are also normalized by this  $\bar{a}_1$ . The parameters  $a_k$  and their standard deviations for all the sample sources are listed in Table 5.2.

## 5.5 Results and Discussion

The sources in the sample used in this study are divided morphologically into multiple classes. The main classification scheme adopted is the Fanaroff-Riley classification (Fanaroff & Riley, 1974). Wide-Angle Tailed (WAT) and Head-Tail (HT) sources are in separate classes. For a discussion of the classification of the sample sources, see Saripalli et al. (2012). The results of the environmental study for each of the classes are described below.

The errors in the derived  $a_k$  parameters for the individual sources are indeed substantial (see Table 5.2). Therefore, while estimating the environment

## 5. ENVIRONMENTS OF EXTENDED RADIO SOURCES

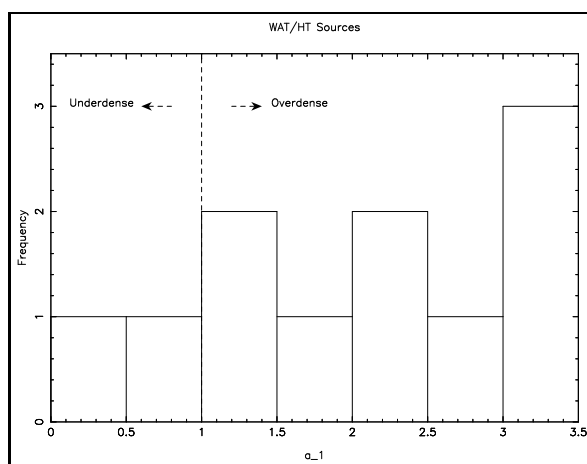
---

for samples of sources of a particular class, the confidence has been improved by computing a weighted mean of each parameter over the sources in the class: this is equivalent to a stacking of images with a weighting corresponding to the noise in the individual images. Additionally, the errors in the weighted means have also been computed.

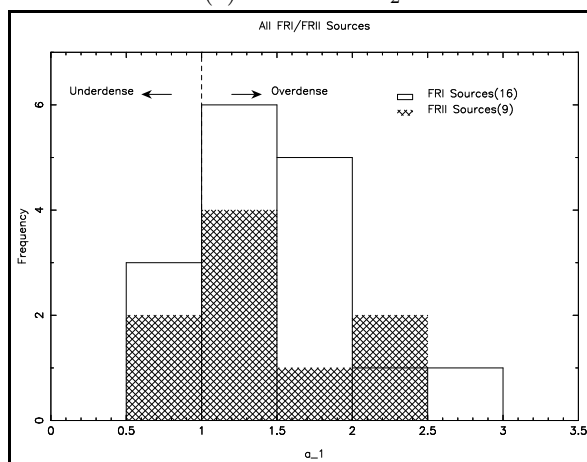
### 5.5.1 The environments of Head-Tail and Wide-angle Tailed ATLBS-ESS sources

Wide angle tailed and Head-tail sources are radio galaxies that show extensive signs of ‘disturbed’ radio morphology. These sources have bent radio jets/lobes. It has been a long held view that the WAT/HT morphology is a result of the interaction of the radio source with cluster gas, either because of ram pressure forces during the movement of the host galaxy through the cluster gas (Owen & Rudnick, 1976) or owing to intra-cluster gas weather created in cluster mergers (Burns et al., 2002). The association of these sources with cluster environments has been taken advantage of to detect galaxy clusters at high redshifts (Best et al., 2003). It is expected, therefore, that the WAT/HT sources show evidence of inhabiting rich environments.

In the sample there are 11 WAT/HT sources. Of the eleven sources, six appear to lie in relatively rich environments (showing values above 2.0 for the parameter  $a_1$ , which gives a measure of the ‘average’ overdensity in the environment of the source). All the four HT sources in the sample are at relatively low redshifts



(a) Parameter  $a_2$



(b) Parameter  $a_2$

Figure 5.5: Histograms of  $a_1$  parameter for (a) WAT/HT and (b) FRI/FRII sources.

## 5. ENVIRONMENTS OF EXTENDED RADIO SOURCES

---

(below redshift of 0.3) and all four are found in rich environments with weighted mean of  $2.465(\pm 0.197)$  for the  $a_1$  parameter. The 7 WAT sources also have a high overdensity, with a weighted mean value of  $1.969(\pm 0.145)$  for  $a_1$  indicating overdense environments as expected for this class of sources. There is a hint of decreasing overdensity with redshift suggesting that the WATs do not appear to be constrained to overdense regions at higher redshifts. However, given the difficulties in detecting faint galaxies at higher redshifts, completeness in galaxy counts will certainly be affected at faint galaxy magnitudes ( $m_r > 22.75$ ) and this limits the confidence in the finding of any trend with redshift. Nevertheless, the finding that WAT and HT sources do indeed inhabit relatively rich environments is consistent with previous findings and lends confidence in the new method proposed herein for studies of environments of radio sources. A histogram of the values of  $a_1$  parameter for WAT/HT subsample is presented in Fig. 5.5a.

### 5.5.2 The environments of FR I and FR II ATLAS-ESS sources

FRI sources have been known to inhabit rich environments: this property has been established with greater confidence for FRIs at relatively lower redshifts. In contrast, FRII sources have been known to favor sparse environments at low redshifts, and are known to reside in richer environments at higher ( $z > 0.5$ ) redshifts (Hill and Lilly 1991; Zirbel 1997). Thus FRII radio sources present a remarkable change in their environments with cosmic epoch. Below are described the findings from the above study for these two classes of sources in the sample.

There are 17 FRI and 15 FR II sources in the source sample. The weighted mean value of  $a_1$  for the 17 FRIs is  $1.326(\pm 0.08)$  where as the corresponding value for the 15 FR IIs is  $1.294 \pm 0.098$ . The sample includes 4 FRI sources that have  $a_1$  below 1. These sources are J0026.8–6643, J0026.4–6721, J0049.3–6703, and J0059.6–6712. These sources are not at particularly high redshifts (all of them have redshifts less than 0.5). However, in case of the latter two sources, it is possible that imaging artifacts and the presence of bright stars in the vicinity may have played a role in underestimating the environmental overdensity.

The subsamples of FRI and FR II sources have been separated into two redshift regimes, one below redshift 0.5 and another above and their environments are compared in each of these regimes. Environments of FRI sources at high redshifts have remained unexplored because of sensitivity issues: FRI sources are lower in luminosity and have more diffuse structures making their detection more difficult at high redshifts. ATLBS is a survey with high surface brightness sensitivity and has imaged sky regions with good resolution; the ATLBS has detected several FRI sources with  $z > 0.5$  (Saripalli et al., 2012). In the source sample of 17 FRIs the redshifts range from 0.21 to 0.97 and there are 4 at redshifts above 0.5. Therefore, an examination of the environments of these FRI sources at relatively high redshifts may be attempted.

However, before examining the results it should be reiterated that because of the finite limit to the sensitivity, neighboring galaxy counts at higher redshifts will be progressively underestimated. Interpreting the results accordingly, it may

## 5. ENVIRONMENTS OF EXTENDED RADIO SOURCES

---

be emphasized that the environments of high redshift sources may only be a lower limit.

It was found that at redshifts above 0.5, FRI and FRII sources inhabit environments that are not too dissimilar in richness. Moreover, both FRI and FRII type sources are found to lie in relatively overdense environments in the  $z > 0.5$  regime. There are 9 FRII sources and 5 FRI sources with  $z > 0.5$ . However, the FRI source J0059.6–6712 has not been used in this comparison as it is on the redshift boundary. Two FRII sources J0105.7–6609 and J0057.7–6655 for which the results may have been affected by nearby bright stars, as well the FRII source J0105.0–6608 for which the host galaxy identification is unclear and the source J0056.6–6743 which displays hybrid morphology have been excluded from this exercise. This gives 5 FRII sources and 4 FRI sources for the study. The average richness (as quantified by the parameter  $a_1$ ) for  $z > 0.5$  FRI sources is  $1.335 \pm 0.196$  as compared to an average value of  $1.305 \pm 0.177$  for the FRII sources at high redshift. Since the comparison is between groups in the same redshift regime, underestimation of galaxy counts will affect both similarly.

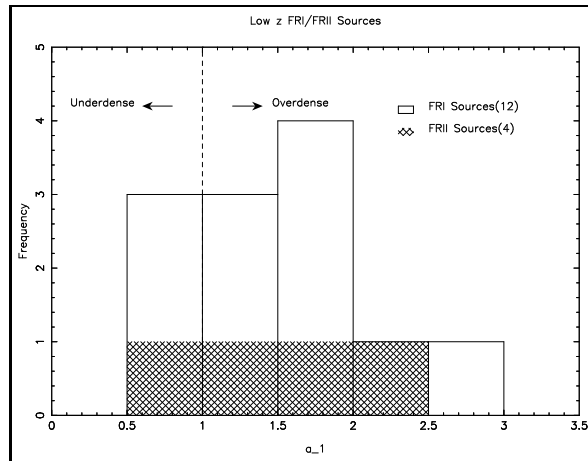
FRI sources at low redshifts appear to inhabit a variety of environments: their  $a_1$  parameters cover the range 0.68 to 2.57. The overall average value of  $a_1$  for low redshift FRI sources is  $1.39 \pm 0.094$  indicating that at  $z < 0.5$  FRI sources, as expected, generally prefer the relatively higher density environments. Of the 12 low-redshift FRIs, only 3 sources are in underdense environments and these have an average value of 0.86 for  $a_1$ . The source sample includes only a small number of FRII sources at low redshifts (only 4 sources in all). Also omitted is the source

J0046.2–6637 for which the identification of the host galaxy is uncertain and the source J0044.3–6746 that has a bright star nearby, leaving 4 FRII sources at low redshifts. 3 of the 4 of these low- $z$  FRIIs are found to have relatively rich environs, with average value of  $1.33 \pm 0.159$  for  $a_1$ . It should be noted that the environmental richness parameter  $a_1$  is similar for the low redshift FRIIs compared to the low redshift FRIIs in the sample. The above comparison between FRI/FRII sources at high and low redshift is depicted graphically in Fig. 5.6.

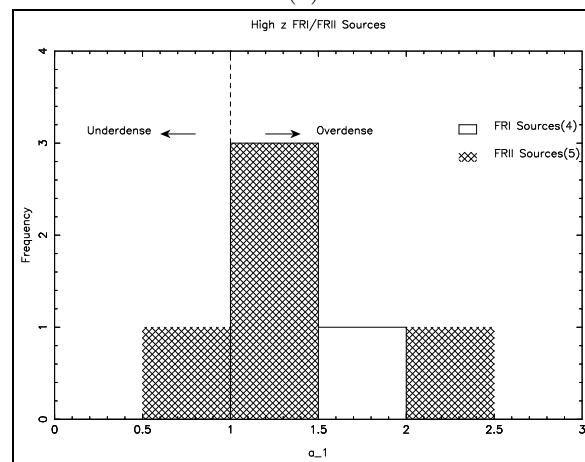
An examination of the FRI subsample as a whole reveals that the FRI sources inhabit environments that are more or less similar, over the redshift range examined here, barring the extreme outliers. And a similar result appears to emerge for FRIIs as well: their subsamples formed above and below redshift of 0.5 display similar  $a_1$  coefficients on the average (see Fig. 5.5b and Fig. 5.6). The weighted mean values of  $a_1$  parameter for the selected 16 FRIIs and 9 FRIIs (Fig. 5.5b) are  $1.38 \pm 0.08$  and  $1.32 \pm 0.12$ . It may be noted here that the HT and WAT sources have been separated from this comparison: most HT and WAT sources are FRIIs and these clearly lie in more overdense regions compared to the FRI source sample (which has HT and WAT sources excluded). This study suggests that the FRIIs and FRIIs may have similar environments and occur in moderately overdense galaxy distribution space within galaxy groups and filaments of the large scale structure; however, the WAT and HT sources inhabit the more extreme overdensities of clusters of galaxies. As is expected in structure formation, the highest density regimes that include clusters of galaxies evolve most rapidly at low redshifts and, therefore, it is unsurprising that redshift evolution across a  $z = 0.5$  boundary appears to be significant only for the WAT sources.

## 5. ENVIRONMENTS OF EXTENDED RADIO SOURCES

---



(a)



(b)

Figure 5.6: Comparative view of the overdensity (as characterized by the parameter  $a_1$ ) of (a) low redshift FRI v/s FRII sources and (b) high redshift FRI and FRII sources.

### 5.5.3 Dipole and quadrupole environmental anisotropy

Next, the environmental parameters  $a_2 - a_5$  were examined. These provide information regarding the dipole and quadrupole *angular* distribution of the overdensity in the vicinity of the sample sources. If the distribution of the overdensity about the radio source is uniform, then these parameters would be expected to vanish. If the distribution is nonuniform, then the parameters may have non-zero values and the sign of each parameter gives further information regarding the angular distribution. In practice, the value of the parameter is compared with the standard deviation for that parameter to estimate the significance. The arguments of the weighting functions  $f_k$  are the angles of the points in the grid with respect to the radio axis.

$a_2$  and  $a_3$  measure the dipole anisotropy in density distribution. The parameter  $a_2$ , which is the overdensity weighted with a sine function, is a measure of the side-to-side density difference on the two sides of the radio axis. The sign of  $a_2$  indicates which side of the source is overdense, and there is no reason to expect any preference for the sign. The parameter  $a_2$  would be expected to average to zero for any population of sources because the sign of this parameter would be equally likely to be positive and negative, although individual sources may have a significant magnitude. The parameter  $a_3$  is the integral of the azimuthal variation in overdensity weighted with a cosine function. This parameter is of importance when examining asymmetric sources because it is a measure of the overdensity

## 5. ENVIRONMENTS OF EXTENDED RADIO SOURCES

---

along the radio axis. A positive sign implies that the density in the direction of the longer radio lobe is higher than that towards the shorter radio lobe, and a negative sign implies the opposite.

$a_4$  and  $a_5$  measure the quadrupole anisotropy in galaxy density distribution about the radio source. The parameter  $a_4$  is the integral overdensity weighted with a sine function for which the argument is twice the position angle with respect to the source axis. This parameter is a matched filter for a quadrupole angular anisotropy in overdensity that has maxima or minima at angles of  $\pi/4$  and  $5\pi/4$  to the radio axis. A positive sign for this parameter implies that the quadrupole anisotropy has overdensities at angles of  $\pi/4$  and  $5\pi/4$  from the direction defined by the vector towards the more extended lobe, and a negative sign implies that the overdensity is along  $3\pi/4$  and  $7\pi/4$ . The last parameter  $a_5$  is weighted by a cosine function that once again has argument twice the position angle with respect to the source axis. This parameter is sensitive to quadrupole anisotropy in density that has maxima along the radio axis or along a direction perpendicular to the source axis. A positive sign for this parameter implies that the overdensity along the radio axis is larger than off the axis, and a negative sign implies that the overdensity in a direction perpendicular to the radio axis is larger. Together, these parameters  $a_2$ – $a_5$  provide a good description of the dipole and quadrupole distribution of the density in the environments of radio sources.

The parameter  $a_3$ , which is a measure of the environmental dipolar overdensity along the radio axis, has a value consistent with zero (within errors) for most of the source types except HT sources. The weighted mean  $a_3$  is  $0.123 \pm 0.046$

(for HT sources),  $0.018 \pm 0.02$  (for FRI source sub-sample),  $-0.021 \pm 0.027$  (for FRII sources) and  $-0.044 \pm 0.037$  (for WAT sources). The weighted mean value of  $a_3$  is significant only for the HT population and it is notable that the value of  $a_3$  for all of the HT sources is positive. These suggest that the tail of Head-tail sources preferentially—and in all cases in the ATLBS-ESS subsample of HT sources used in this work—points in the direction of higher local galaxy density. This result may be interpreted in several ways. One explanation may be that the host galaxies of these HT sources are orbiting around the cluster center and currently in projection the hosts are moving away from the cluster centers with the tails pointing back towards the cluster center. Alternatively, the sources may be in clusters undergoing merger events and the tails of the HT sources are being dragged by the intracluster weather toward the cluster center.

### 5.5.4 Asymmetric ATLBS-ESS sources

Next the sources which exhibit significantly asymmetric radio morphology have been examined. A subsample of ‘asymmetric’ sources was compiled on the basis of lobe asymmetry; for inclusion in this sub-sample, one of the lobes is required to be more than 1.5 times the extent of the opposite lobe. With this selection criterion, 7 asymmetric sources were found in ATLBS-ESS. The asymmetric source sample has been separately presented in Table. 5.3.

The environmental parameters have been examined for the selected asymmetric sources. Almost all the asymmetric sources in the sample appear to lie in rich

## 5. ENVIRONMENTS OF EXTENDED RADIO SOURCES

---

environments, as indicated by high to moderate values of  $a_1$ ; the one exception is J0101.1–6600, which has an  $a_1$  parameter corresponding to an underdense region. It was noted that all the asymmetric sources, except J0045.5–6726, show negative values for the parameter  $a_3$ , which is a clear indication that the ambient galaxy density is almost always higher in the direction of the shorter lobe. The weighted mean value for  $a_3$  is  $-0.0359 \pm 0.0341$ . The latter value is significant when taken in the context of the values of  $a_3$  for the subsample of *symmetric* sources. The values of  $a_3$  parameter are positive or negative for symmetric sources, without any significant preference towards positive or negative sign. In comparison, all except one of the sources in the asymmetric source sample have a negative sign for the value of the  $a_3$  parameter. Examined in this light, the distribution of the  $a_3$  parameter is significant.

All of the asymmetric sources have a positive  $a_5$  and the weighted mean  $a_5$  for the asymmetric sources is, significantly,  $0.051 \pm 0.013$ . This implies that asymmetric radio sources are usually aligned along the line of excess galaxy density with a quadrupole asymmetry apart from any dipole component. It may be that when double radio sources are created by jets that happen to be aligned with galaxy overdensity, and the galaxy clustering is on one side, the associated gas inhibits jet advance via ram pressure interaction and it is radio galaxies in such environmental circumstances that display grossly asymmetric morphology. It may also be noted that none of the subsamples of sources, except the asymmetric sources, show significant values of  $a_5$ . In most of the asymmetric cases, there is more galaxy overdensity on the shorter side consistent with the expectations that gas density follows galaxy density and the side with higher gas density would be

expected to be shorter owing to slower advance speed for the jets. The positive value of  $a_5$ , together with a negative value of  $a_3$  for most of the sample, implies that the environmental overdensity is not a gradient but is a concentration in the direction of the shorter lobe. The  $a_4$  parameter for these asymmetric sources has less significance in magnitude and appears random in signs, as expected. Curiously, the parameter  $a_2$  for this sample is positive for all of the asymmetric sources; however, the weighted mean  $a_2$  is  $0.048 \pm 0.034$  and is not significant.

All of the six asymmetric sources with negative values for  $a_3$  have linear size in the range 400 – 600 kpc. J0045.5–6726, which alone has a positive value for  $a_3$ , has a significantly smaller linear size of 164 kpc and, therefore, the anomalous behavior for this source may be understood as arising from its relatively small size due to which the lobe extent may be more influenced by the local inter-stellar medium of the host galaxy rather than the intergalactic gas associated with the large scale galaxy distribution, which is what is probed by the approach used in this work. The high value of  $a_1$  for the FRI source J0045.5–6726 indicates a rich environment for this source; however, the positive sign for  $a_3$  implies that the longer side of the source is in denser regions. Additionally, the source has a high value for  $a_5$ , showing that the density distribution is along the radio axis. This source has an FRI morphology and an alternate explanation for the positive value of  $a_3$  for this source may be that the higher galaxy density on the longer side preserves the diffuse emission on that side by limiting expansion losses.

### 5.6 Summary

In Chapter 3, details of optical observations and data reduction for the ATLBS survey regions have been presented. In this chapter, the optical observations were used to determine the redshifts and magnitudes of the host galaxies of the ATLBS-ESS sample of radio sources formed of the extended radio sources detected in the ATLBS survey. In this study, galaxy catalogs constructed from the optical data were utilized to estimate the environmental parameters of selected sources from the ATLBS-ESS sample. A set of parameters  $a_1 - a_5$  has been defined to quantify the local galaxy overdensity and its angular anisotropy with respect to the axis of the radio sources using smoothed galaxy density maps. Dipole and quadrupole anisotropy has been estimated for the individual sources and these measures have been stacked (averaged) to estimate mean measures and their errors for different classes of radio source morphologies. The method used to quantify environmental asymmetry is new and used here for the first time.

Examining the anisotropy parameters for a sub-sample of extended double radio sources that includes all sources with pronounced asymmetry in lobe extents, good evidence was found for environmental anisotropy being the dominant cause for lobe asymmetry in that higher galaxy density occurs almost always on the side of the shorter lobe, and this validates the usefulness of the method proposed and adopted here. The environmental parameters have been used to examine and compare the environments of FRI and FRII radio sources in two redshift regimes ( $z < 0.5$  and  $z > 0.5$ ). Wide-angle tail sources and Head-tail sources lie in the most overdense environments. The Head tail source environments display

dipolar anisotropy in that higher galaxy density appears to lie in the direction of the tails. Excluding the Head-tail and Wide-angle tail sources, subsamples of FRI and FRII sources from the ATLBS survey appear to lie in similar moderately overdense environments, with no evidence for redshift evolution in the regimes studied herein.

# 5. ENVIRONMENTS OF EXTENDED RADIO SOURCES

Source Name	Extended Source Name	Redshift	Source Type	PA	$\alpha_1$	$\sigma_{\alpha_1}$	$\alpha_2$	$\sigma_{\alpha_2}$	$\alpha_3$	$\sigma_{\alpha_3}$	$\alpha_4$	$\sigma_{\alpha_4}$	$\alpha_5$	$\sigma_{\alpha_5}$
J0024.4-6636	J002426-663612	0.21	I	90	2.57237	0.4	0.0907	0.1	-0.15	-0.14	0.0302	0.04	0.04	0.04
J0025.0-6658	J002500-665804**	0.64	WAT	27	1.31131	0.37	-0.14	0.14	-0.01	-0.02	-0.01	0.05	-0.01	0.01
J0026.4-6721	J002628-672148	0.27*	I	-90	0.97087	0.25	0.0908	0.07	0.0809	0.07	0.0202	0.03	0.08	0.03
J0026.8-6643	J002648-664402**	0.21	I	207	0.93093	0.4	-0.07	0.07	-0.01	0.01	-0.05	0.04	0.01	0.04
J0030.7-6714	J003045-671437**	0.97	I	37	1.07107	0.59	0.13012	0.21	0.0809	0.2	-0.06	0.06	0.11	0.09
J0031.1-6642	J003108-664245**	0.77	II	-6	0.65065	0.47	-0.07	0.07	0.06	0.07	0.02	0.06	-0.03	0.06
J0032.9-6614	J003257-661417**	0.92*	I	-34	1.63163	0.58	-0.55	0.57	0.20	0.15	-0.06	0.05	-0.04	0.09
J0033.4-6714	J003329-671415**	0.41*	I	239	1.33133	0.25	0.16	0.11	0.14	0.13	0.1	0.03	-0.06	0.03
J0035.0-6612	J003501-661252**	0.47*	I	187	1.616	0.32	0.12	0.12	0.01	0.01	-0.05	0.05	0.01	0.03
J0036.9-6645	J003654-664513	0.23	I	63	1.21121	0.34	-0.07	0.08	-0.08	0.08	0.03	0.04	-0.04	0.04
J0040.2-6553	J004014-655325	0.51*	II	243	1.313	0.3	-0.07	0.07	0.05	0.04	0.02	0.03	-0.09	0.04
J0041.7-6726	J004145-672629**	0.29*	HT	256	3.32332	0.45	-0.02	0.03	0.06	0.06	0.02	0.02	-0.02	0.03
J0042.1-6728	J004208-672805**	0.25	HT	180	2.97297	0.48	0.23	0.25	0.18	0.16	-0.04	0.02	-0.14	0.03
J0043.2-6751	J004317-675147**	0.38	WAT	90	3.01301	0.32	-0.06	0.08	0.19	0.18	0.07	0.07	0.01	0.04
J0043.6-6624	J004337-662447	0.99	WAT	124	0.46046	0.74	0.05	0.05	0.01	0.19	0.01	0.05	0.05	0.11
J0044.3-6746	J004419-674657**	0.29	II	198	1.73173	0.36	0.19	0.19	0.04	0.06	0.02	0.03	-0.06	0.04
J0044.7-6656	J004451-665628**	0.72	II	55	2.02202	0.4	-0.19	0.19	0.05	0.06	-0.03	0.05	-0.02	0.05
J0045.5-6726	J004532-672635**	0.27	I	72	1.93193	0.46	0.01	0.01	0.21	0.21	0.01	0.03	0.13	0.03
J0046.2-6637	J004613-663708**	0.37	II	135	1.75175	0.36	0.20	0.21	0.09	0.11	0.05	0.05	-0.01	0.04
J0049.3-6703	J004922-670358	0.47	I	240	0.68068	0.29	-0.04	0.04	0.01	0.01	-0.01	0.03	-0.03	0.03
J0052.7-6651	J005248-665109**	0.24	HT	-45	2.39239	0.44	-0.04	0.07	0.19	0.19	0.06	0.04	-0.01	0.04
J0055.7-6610	J005548-661031**	0.22	HT	56	1.92192	0.3	-0.06	0.07	0.1	0.11	0.01	0.03	0.07	0.07
J0056.4-6651	J005627-665122**	0.19	WAT	-45	2.13213	0.44	0.01	0.02	-0.11	0.12	-0.05	0.05	0.02	0.04
J0056.6-6743	J005637-674343**	0.93	II	79	1.26126	0.51	0.39	0.38	0.15	0.12	0.02	0.09	-0.07	0.09
J0056.9-6632	J005657-663239	0.25*	II	53	2.03203	0.41	-0.06	0.06	-0.4	0.05	0.02	0.01	0.05	0.03
J0057.0-6734	J005704-673413	0.31*	II	-90	1.73173	0.32	-0.15	0.17	-0.15	0.13	-0.01	0.03	-0.01	0.04
J0057.2-6651	J005707-665059	0.24*	I	112	1.82182	0.41	0.1	0.09	-0.03	0.02	-0.03	0.04	0.04	0.04
J0057.4-6703	J005728-670325**	0.26*	WAT	225	3.13313	0.35	-0.05	0.04	-0.13	0.13	0.06	0.03	0.02	0.03
J0057.7-6655	J005745-665507	0.66	II	120	0.79079	0.33	0.05	0.02	-0.07	0.07	0.05	0.04	0.07	0.05
J0059.6-6712	J005941-671254**	0.5	I	180	0.81081	0.26	-0.1	0.09	0.0	0.01	0.03	0.03	0.02	0.03
J0101.1-6600	J010107-660018	0.24	II	174	0.81081	0.3	0.02	0.02	-0.01	0.01	0.03	0.02	0.04	0.03
J0101.5-6742	J010134-674214**	0.59	WAT	-63	1.29129	0.29	-0.1	0.09	-0.19	0.2	-0.02	0.02	-0.01	0.01
J0102.6-6658	J010238-665813**	0.61	I	40	1.46146	0.4	0.07	0.05	-0.19	0.2	-0.02	0.03	0.04	0.04
J0102.9-6722	J010256-672220	0.84	WAT	135	0.56056	0.54	0.25	0.22	-0.24	0.25	-0.02	0.03	0.05	0.04
J0103.1-6632	J010310-663221	0.4*	I	90	1.212	0.31	0.02	0.02	0.06	0.04	0.04	0.07	-0.04	0.08
J0103.2-6614	J010315-661425	0.33*	II	186	1.17117	0.28	0.02	0.02	-0.01	0.01	-0.03	0.03	0.02	0.03
J0103.7-6632	J010344-663227	0.59	II	-90	1.212	0.37	0.04	0.05	-0.04	0.05	0.03	0.03	0.01	0.03
J0103.7-6747	J010345-674746**	0.33*	I	-63	2.26226	0.44	-0.08	0.08	-0.12	0.11	0.02	0.01	0.04	0.05
J0105.0-6608	J010500-660856**	0.85	II	248	0.32032	0.59	-0.04	0.03	-0.05	0.04	0.06	0.03	-0.01	0.03
J0105.7-6609	J010540-660940**	0.98	II	-85	0.14014	0.94	-0.02	0.01	-0.06	0.06	0.02	0.08	0.09	0.09
J0106.0-6653	J010601-665337	0.26*	I	63	1.717	0.29	0.15	0.15	0.02	0.01	0.06	0.06	-0.1	0.09
J0108.6-6655	J010838-665527**	0.53*	I	27	1.27127	0.27	0.08	0.07	0.08	0.09	0.01	0.01	0.0	0.04
J0110.7-6705	J011046-670507**	0.8	II	159	1.03103	0.64	-0.19	0.17	0.21	0.23	-0.12	0.09	0.08	0.1

**Table 5.2:** The table presents the sample along with the parameters  $\alpha_k$  and their standard deviations. Column 1 gives the source name, with the extended designation given in column 2 (\*\* denotes a source designation taken from the Sydney University Molonglo Sky Survey (SUMSS) (Mauch et al., 2003)) Column 3 and 4 give the redshift of the source and the source type respectively, (\*, \*\* denoting spectroscopically measured values for the redshift). Column 5 gives the position angle of the sources in degrees. Columns 6-14 present each overdensity parameter and the normalized standard deviations for each parameter. The column for each of the overdensity parameter gives three values: the best estimate of the value of the parameter itself as well as the values it may have at  $\pm 5$  degrees from the listed PA, giving the uncertainty in the parameter due to the uncertainty in PA.

Source Name	Extended Source Name	Redshift	Source Type	PA	$a_1$	$\sigma_{a_1}$	$a_2$	$\sigma_{a_2}$	$a_3$	$\sigma_{a_3}$	$a_4$	$\sigma_{a_4}$	$a_5$	$\sigma_{a_5}$
J0024.4-6636	J002426-663612	0.21	I	90	2.57 <sup>2.57</sup>	0.4	0.09 <sup>0.07</sup>	0.1	-0.15 <sup>-0.14</sup>	0.11	0.03 <sup>0.02</sup>	0.04	0.04 <sup>0.04</sup>	0.04
J0045.5-6726	J004532-672635**	0.27	I	72	1.93 <sup>1.93</sup>	0.46	0.01 <sup>-0.01</sup>	0.1	0.21 <sup>0.21</sup>	0.09	0.01 <sup>-0.01</sup>	0.03	0.13 <sup>0.13</sup>	0.03
J0057.2-6651	J005707-665059	0.24*	I	112	1.82 <sup>1.82</sup>	0.41	0.1 <sup>0.09</sup>	0.08	-0.03 <sup>-0.02</sup>	0.08	-0.03 <sup>-0.04</sup>	0.03	0.04 <sup>0.04</sup>	0.03
J0101.1-6600	J010107-660018	0.24	II	174	0.81 <sup>0.81</sup>	0.3	0.02 <sup>0.02</sup>	0.07	-0.01 <sup>-0.01</sup>	0.08	0.03 <sup>0.03</sup>	0.03	0.04 <sup>0.04</sup>	0.03
J0102.6-6658	J010238-665813**	0.61	I	40	1.46 <sup>1.46</sup>	0.4	0.07 <sup>0.09</sup>	0.11	-0.24 <sup>-0.23</sup>	0.11	-0.02 <sup>-0.03</sup>	0.05	0.04 <sup>0.03</sup>	0.04
J0103.2-6614	J010315-661425	0.33*	II	186	1.17 <sup>1.17</sup>	0.28	0.02 <sup>0.02</sup>	0.08	-0.04 <sup>-0.05</sup>	0.08	0 <sup>0.03</sup>	0.03	0.01 <sup>0.01</sup>	0.03
J0103.7-6632	J010344-663227	0.59	II	-90	1.21 <sup>1.2</sup>	0.37	0.04 <sup>0.03</sup>	0.11	-0.12 <sup>-0.11</sup>	0.1	0.02 <sup>0.01</sup>	0.04	0.04 <sup>0.05</sup>	0.05

Table 5.3: The table presents the asymmetric source subsample along with the parameters  $a_k$  and the standard deviations in each of the parameters. Various columns follow the same scheme as that for Table. 5.2.

## **5. ENVIRONMENTS OF EXTENDED RADIO SOURCES**

---

## Conclusions

This thesis discusses population studies of the radio sources as observed in the ATLBS survey. The aim of the ATLBS survey was to make images of the radio sky with exceptional surface brightness; which gives a complete picture of mJy and sub-mJy radio sources allowing studies of diffuse components associated with extragalactic radio sources in the sky. The sub-mJy population of sources is crucial in understanding the cosmic evolution of radio sources. The images used have the sensitivity and dynamic range to explore the transition regime from mJy to sub-mJy radio source counts and usefully constrain the flux density of the emergence of new populations. The latter part of the thesis has presented an investigation into the optical environments of extended radio sources and the impact of environment on the morphology of radio sources. Below, the salient points of the thesis work are presented.

## 6. CONCLUSIONS

---

### 6.1 Summary and Results

The study of the cosmic population of radio sources presented here has been carried out using the the ATLBS survey radio observations and the accompanying optical observations. ATLBS radio survey is a moderately wide-field survey covering 8.42 square degrees sky area. The radio observations have been carried out using the Australia Telescope Compact Array. The visibility coverage of the data is complete out to 750 m and hence provides good representation of extended emission components associated with radio sources. High-resolution radio images of the ATLBS survey regions have been made with a beam FWHM of  $6''$ , with rms noise  $72 \mu\text{Jy beam}^{-1}$ , free of any imaging errors and artefacts. The survey area has been divided into two adjacent regions in the sky, each of which is covered by a 19-pointing mosaic image.

The ATLBS survey regions have been also imaged in optical SDSS  $r'$  band using the CTIO 4 meter Blanco Telescope, with a total of 28 images. The imaging has been carried out using the MOSAIC II multi-CCD imager, which allows large fields ( $37' \times 37'$ ) to be imaged at the same time. The optical images provide information regarding the hosts of the radio sources in the ATLBS survey and their galaxy environments. From these images, optical catalogs of the galaxies in the ATLBS survey regions have been constructed which go to a depth of 22.75 magnitudes.

Using these radio and optical images, a source catalog of ATLBS radio sources has been created. *It is noteworthy that the catalog has been specifically made to*

*be a source catalog as opposed to a component catalog, a feature that is unlikely in the case of catalogs constructed in a completely automated manner.* The catalog construction used new strategies, such as the use of multi-resolution images to simultaneously remove the issues of confusion-blending and missing sources as well as use of multi-resolution data, including optical images to identify radio sources. The radio source catalog lists the positions, flux densities, source type (classified into unresolved, single component Gaussian and Complex sources) as well as the number of components for sources with complex morphology.

The source catalog has been used to estimate radio source counts to a depth of 0.4 mJy. The radio source counts have been corrected for possible sources of error which affect the correct determination of source counts; especially noise bias, which is important in determination of the source counts near the detection thresholds. The radio source counts for ATLBS survey are systematically lower than those from deep surveys reported in literature. The upturn or flattening reported widely in previous studies has not been found in the source counts for ATLBS survey down to 0.4 mJy flux density limit that has been probed. Possible reasons for the substantially higher flux density at which the upturn has been observed previously are: non-inclusion of corrections for noise bias in some previous studies, the small sky areas covered by the deep surveys and the lack of adoption of imaging and analysis methods that identify sources as opposed to components.

The optical images were used to determine the large scale environments of extended sources in the ATLBS survey. The Extended Source Sample (ESS) is

## 6. CONCLUSIONS

---

a sub-sample of ATLAS sources with projected linear sizes larger than half an arcminute. A sub-sample of ESS has been selected for examination of optical environments as characterized by galaxy density distribution. Smoothed galaxy density maps were used to derive an estimate of the richness of environments of the radio sources. Further, a set of parameters  $a_1$  to  $a_5$  was devised, which give the angular distribution of the richness of galaxy environments in the vicinity of radio sources. This method is used to characterize the environments of radio sources and gives the *angular distribution* of the galaxy density around the radio source with respect to the jet axis of the extended radio source.

Using this method, the environments of WAT and HT sources were found to be rich, which was expected from previous studies. This confirmation of a previous finding gives confidence in the new method described and adopted here. The environments of FRI and FRII sources were, contrary to expectations, found to be of similar richness at both high and low redshifts. A special study was made of the angular distribution of galaxies in the neighbourhood of radio sources that were highly asymmetric in radio morphology, which demonstrated clearly that environments have an impact on radio source morphology, presumably via ram pressure limiting of head advance speeds by associated intergalactic gas.

In conclusion, the thesis points out (a) the importance of low surface brightness imaging and identification of sources in correctly estimating evolutionary transitions in radio source populations, (b) the importance of large scale structure in the growth and formation of asymmetry in extended radio sources. Finally, the radio and optical images as well as the techniques and methods described in

this thesis form an important resource for future studies.

## 6.2 Pathways for Continued Work

As mentioned above, the radio and optical images may be used in future studies of radio sources. Below are listed several possible studies which may be attempted with the data.

In particular, since the radio images are available not only in total intensity but Stokes in Q and U polarization as well; polarization studies of radio sources in the ATLBS survey are possible. One of the studies not elaborated in this thesis is the study of the coherence of magnetic fields in extended radio sources. ATLBS survey data is well suited for this purpose due to the sensitive radio images and high resolution. The coherence of the magnetic field in extended sources can be measured by calculating the polarization in extended sources in two different ways: one assuming that the resolution of the images is equal to the size of the source and the other with the existing high resolution of the images. The ratio of the polarization obtained via these two ways can provide information regarding the coherence of magnetic fields across the radio source under consideration.

Another possible study that may be carried out is the study of the feedback provided by radio galaxies in kinetic mode via PdV work done by the radio lobes in the environments of the radio source. Since the radio lobe luminosity provides a time-integrated estimate of the energy injected by the radio galaxy into its environs, the influence of the radio galaxy on its environs can be accurately measured,

## 6. CONCLUSIONS

---

which is not possible in other wave bands such as optical and X-ray, where only the instantaneous energy output of the AGN may be available. ATLAS survey images are eminently suited for this study, since the diffuse emission associated with radio galaxies has been detected in its entirety because of the high sensitivity of the images and because sources are detected to moderately high redshifts.

In summary, the work presented in this thesis demonstrates (a) importance of low surface brightness imaging and identification of sources in correctly estimating evolutionary transitions in radio source populations, (b) the importance of large scale structure in the growth and formation of asymmetry in extended radio sources. The methods and techniques that have been used in the study of the ATLAS survey data form important tools which are useful in the imaging, analysis and interpretation of new wide-field, deep surveys which would be carried out with new interferometers such as LOFAR and SKA.

## Radio Images of the ATLBS Survey

In this appendix the high resolution radio images described in Chapter 2 are attached. These images of the two regions A and B (centered at RA:  $00^h 35^m 00^s$ , DEC:  $-67^\circ 00' 00''$  and RA:  $00^h 59^m 17^s$ , DEC:  $-67^\circ 00' 00''$  respectively) are given separately.

## A. APPENDIX

---

## BIBLIOGRAPHY

Abell, G. O. 1958, *ApJS*, 3, 211, 211-117

Alfvén, H., & Herlofson, N. 1950, *Physical Review*, 78, 616, 616-13

Alvarado, F., Wenderoth, E., Alcaïno, G., & Liller, W. 1995, *AJ*, 110, 646, 646-53

Archer, S., Baldwin, J. E., Edge, D. O., et al. 1959, in *IAU Symposium, Vol. 9, URSI Symp. 1: Paris Symposium on Radio Astronomy*, ed. R. N. Bracewell, 487-2

Baade, W., & Minkowski, R. 1954, *ApJ*, 119, 206, 206-2, 12, 13

Becker, R. H., White, R. L., & Helfand, D. J. 1994, in *Astronomical Society of the Pacific Conference Series, Vol. 61, Astronomical Data Analysis Software and Systems III*, ed. D. R. Crabtree, R. J. Hanisch, & J. Barnes, 165-5, 95

Becker, R. H., White, R. L., & Helfand, D. J. 1995, *ApJ*, 450, 559, 559-5

Begelman, M. C., Blandford, R. D., & Rees, M. J. 1984, *Reviews of Modern Physics*, 56, 255, 255-14

## **BIBLIOGRAPHY**

---

- Benn, C. R., Rowan-Robinson, M., McMahon, R. G., Broadhurst, T. J., & Lawrence, A. 1993, MNRAS, 263, 98, 98 iv, 65
- Bertin, E., & Arnouts, S. 1996, A&AS, 117, 393, 393 54
- Best, P. N. 2009, Astronomische Nachrichten, 330, 184, 184 16
- Best, P. N., Lehnert, M. D., Miley, G. K., & Röttgering, H. J. A. 2003, MNRAS, 343, 1, 1 vi, 108, 128
- Bicknell, G. V. 1995, ApJS, 101, 29, 29 16
- Blandford, R. D., & Rees, M. J. 1974, MNRAS, 169, 395, 395 13
- Blanton, E. L., Randall, S. W., Clarke, T. E., et al. 2011, ApJ, 737, 99, 99 vi, 108
- Bock, D. C.-J., Large, M. I., & Sadler, E. M. 1999, AJ, 117, 1578, 1578 4
- Boehringer, H., Voges, W., Fabian, A. C., Edge, A. C., & Neumann, D. M. 1993, MNRAS, 264, L25, L25 vi, 108
- Bolton, J. G., Stanley, G. J., & Slee, O. B. 1949, Nature, 164, 101, 101 2
- Bondi, M., Ciliegi, P., Schinnerer, E., et al. 2008, ApJ, 681, 1129, 1129 90
- Bondi, M., Ciliegi, P., Zamorani, G., et al. 2003, A&A, 403, 857, 857 7
- Burns, J. O., Loken, C., Roettiger, K., et al. 2002, New Astronomy Review, 46, 135, 135 128
- Chen, R., Peng, B., Strom, R. G., & Wei, J. 2012, MNRAS, 420, 2715, 2715 vi, 108

## BIBLIOGRAPHY

---

- Chilingarian, I. V., Melchior, A.-L., & Zolotukhin, I. Y. 2010, MNRAS, 405, 1409, 1409 121
- Ciliegi, P., McMahon, R. G., Miley, G., et al. 1999, MNRAS, 302, 222, 222 6
- Clark, B. G. 1980, A&A, 89, 377, 377 29
- Condon, J. J. 1989, ApJ, 338, 13, 13 iv, 65
- . 1992, ARAA, 30, 575, 575 17
- Condon, J. J. 2007, in Astronomical Society of the Pacific Conference Series, Vol. 380, Deepest Astronomical Surveys, ed. J. Afonso, H. C. Ferguson, B. Mobasher, & R. Norris, 189 v, 8
- Condon, J. J., Cotton, W. D., Greisen, E. W., et al. 1998, AJ, 115, 1693, 1693 5, 34, 102
- Condon, J. J., Cotton, W. D., Yin, Q. F., et al. 2003, AJ, 125, 2411, 2411 8
- Condon, J. J., Griffith, M. R., & Wright, A. E. 1993, AJ, 106, 1095, 1095 4
- Condon, J. J., Cotton, W. D., Fomalont, E. B., et al. 2012, ApJ, 758, 23, 23 7, 19
- de Zotti, G., Massardi, M., Negrello, M., & Wall, J. 2010, Astronomy and Astrophysics Reviews, 18, 1, 1 3, 66
- Dupé, F.-X., Rassat, A., Starck, J.-L., & Fadili, M. J. 2011, A&A, 534, A51, A51 5

## **BIBLIOGRAPHY**

---

- Eales, S., Rawlings, S., Law-Green, D., Cotter, G., & Lacy, M. 1997, *MNRAS*, 291, 593, 593–113
- Eddington, A. S. 1913, *MNRAS*, 73, 359, 359–90
- Edge, D. O., Shakeshaft, J. R., McAdam, W. B., Baldwin, J. E., & Archer, S. 1959, *Memoirs of the RAS*, 68, 37, 37–2
- Fanaroff, B. L., & Riley, J. M. 1974, *MNRAS*, 167, 31P, 31P–14, 127
- Fixsen, D. J., Kogut, A., Levin, S., et al. 2011, *ApJ*, 734, 5, 5–18
- Franzen, T. M. O., Davies, M. L., Waldram, E. M., et al. 2010, *ArXiv e-prints*, arXiv:1012.3711–3
- Fukugita, M., Shimasaku, K., & Ichikawa, T. 1995, *PASP*, 107, 945, 945–122
- Gal, R. R. 2008, in *Lecture Notes in Physics*, Berlin Springer Verlag, Vol. 740, *A Pan-Chromatic View of Clusters of Galaxies and the Large-Scale Structure*, ed. M. Plionis, O. López-Cruz, & D. Hughes, 119–113
- Garn, T., Green, D. A., Riley, J. M., & Alexander, P. 2008a, *MNRAS*, 383, 75, 75–64
- . 2008b, *MNRAS*, 387, 1037, 1037–64
- Gendre, M., Wall, J. V., & Best, P. N. 2011, in *American Astronomical Society Meeting Abstracts*, 218, 317.02–114
- Gendre, M. A., Best, P. N., & Wall, J. V. 2010, *MNRAS*, 404, 1719, 1719–113
- Gopal-Krishna, & Wiita, P. J. 2001, *A&A*, 373, 100, 100–16

## BIBLIOGRAPHY

---

- Gregory, P. C., Scott, W. K., Douglas, K., & Condon, J. J. 1996, *ApJS*, 103, 427, 427 4
- Griffith, M. R., & Wright, A. E. 1993, *AJ*, 105, 1666, 1666 4
- Griffith, M. R., Wright, A. E., Burke, B. F., & Ekers, R. D. 1994, *ApJS*, 90, 179, 179 4
- . 1995, *ApJS*, 97, 347, 347 4
- Gruppioni, C., Mignoli, M., & Zamorani, G. 1999, *MNRAS*, 304, 199, 199 iv, 65
- Hardcastle, M. J. 2004, *A&A*, 414, 927, 927 117
- Hatch, N. A., De Breuck, C., Galametz, A., et al. 2011, *MNRAS*, 410, 1537, 1537 vi, 108
- Hey, J. S., Parsons, S. J., & Phillips, J. W. 1946, *Nature*, 158, 234, 234 11
- Heywood, I., Jarvis, M. J., & Condon, J. J. 2013, *MNRAS*, 432, 2625, 2625 8
- Hill, G. J., & Lilly, S. J. 1991, *ApJ*, 367, 1, 1 vi, 108, 117
- Hodge, J. A., Zeimann, G. R., Becker, R. H., & White, R. L. 2009, *AJ*, 138, 900, 900 5
- Hopkins, A. M., Afonso, J., Chan, B., et al. 2003, *AJ*, 125, 465, 465 iv, 63, 90, 97, 101
- Hopkins, A. M., Mobasher, B., Cram, L., & Rowan-Robinson, M. 1998, *MNRAS*, 296, 839, 839 6

## **BIBLIOGRAPHY**

---

- Huynh, M. T., Jackson, C. A., Norris, R. P., & Fernandez-Soto, A. 2008, AJ, 135, 2470, 2470 iv, 65
- Huynh, M. T., Jackson, C. A., Norris, R. P., & Prandoni, I. 2005, AJ, 130, 1373, 1373 iv, 63, 65, 95, 96, 97
- Ibar, E., Ivison, R. J., Biggs, A. D., et al. 2009, MNRAS, 397, 281, 281 64, 65
- Jauncey, D. L. 1968, ApJ, 152, 647, 647 73
- Jennison, R. C., & Das Gupta, M. K. 1953, Nature, 172, 996, 996 12
- Kaiser, C. R., & Best, P. N. 2007, MNRAS, 381, 1548, 1548 16
- Kawakatu, N., Kino, M., & Nagai, H. 2009, ApJL, 697, L173, L173 16
- Kim, R. S. J., Kepner, J. V., Postman, M., et al. 2002, AJ, 123, 20, 20 118
- Lin, Y.-T., Shen, Y., Strauss, M. A., Richards, G. T., & Lunnan, R. 2010, ApJ, 723, 1119, 1119 16
- Longair, M. S., & Seldner, M. 1979, MNRAS, 189, 433, 433 vi, 108
- Maltby, P., & Moffet, A. T. 1962, ApJS, 7, 141, 141 13
- Mauch, T., Klöckner, H.-R., Rawlings, S., et al. 2013, MNRAS, 435, 650, 650 64
- Mauch, T., Murphy, T., Buttery, H. J., et al. 2003, MNRAS, 342, 1117, 1117 4, 142
- McCarthy, P. J., van Breughel, W., Kapahi, V. K., & Subrahmanya, C. R. 1991, AJ, 102, 522, 522 vi, 109

## BIBLIOGRAPHY

---

- McGreer, I. D., Helfand, D. J., & White, R. L. 2009, *AJ*, 138, 1925, 1925 5
- Metcalfe, N., Shanks, T., Fong, R., & Jones, L. R. 1991, *MNRAS*, 249, 498, 498  
122
- Mills, B. Y., & Thomas, A. B. 1951, *Australian Journal of Scientific Research A  
Physical Sciences*, 4, 158, 158 12
- Mitchell, K. J., & Condon, J. J. 1985, *AJ*, 90, 1957, 1957 17, 73
- Moss, D., Seymour, N., McHardy, I. M., et al. 2007, *MNRAS*, 378, 995, 995 64
- Murdoch, H. S., Crawford, D. F., & Jauncey, D. L. 1973, *ApJ*, 183, 1, 1 90
- Norris, R. P., Huynh, M. T., Jackson, C. A., et al. 2005, *AJ*, 130, 1358, 1358 6
- Norris, R. P., Afonso, J., Bacon, D., et al. 2013, *Publications of the Astron. Soc.  
of Australia*, 30, 20, 20 9, 10
- Oke, J. B., & Schmidt, M. 1963, *AJ*, 68, 288, 288 3
- Overzier, R. A., Bouwens, R. J., Cross, N. J. G., et al. 2008, *ApJ*, 673, 143, 143  
vi, 108
- Owen, F. N., & Laing, R. A. 1989, *MNRAS*, 238, 357, 357 16
- Owen, F. N., & Ledlow, M. J. 1994, in *Astronomical Society of the Pacific Confer-  
ence Series*, Vol. 54, *The Physics of Active Galaxies*, ed. G. V. Bicknell, M. A.  
Dopita, & P. J. Quinn, 319 16
- Owen, F. N., Ledlow, M. J., & Keel, W. C. 1996, *AJ*, 111, 53, 53 16
- Owen, F. N., & Morrison, G. E. 2008, *AJ*, 136, 1889, 1889 7

## **BIBLIOGRAPHY**

---

- Owen, F. N., & Rudnick, L. 1976, *ApJL*, 205, L1, L1 128
- Pearson, T. J., & Readhead, A. C. S. 1984, *ARAA*, 22, 97, 97 32
- Ponente, P. P., Ascasibar, Y., & Diego, J. M. 2011, *MNRAS*, 418, 691, 691 18
- Popesso, P., Böhringer, H., Romaniello, M., & Voges, W. 2005, *A&A*, 433, 415, 415 119
- Postman, M., Lubin, L. M., Gunn, J. E., et al. 1996, *AJ*, 111, 615, 615 x, 117
- Prandoni, I., Gregorini, L., Parma, P., et al. 2000, *A&AS*, 146, 31, 31 6
- . 2001, *A&A*, 365, 392, 392 v, 8, 66, 95, 96
- Reber, G. 1940, *ApJ*, 91, 621, 621 2
- Rengelink, R. B., Tang, Y., de Bruyn, A. G., et al. 1997, *A&AS*, 124, 259, 259 4
- Richards, E. A. 2000, *ApJ*, 533, 611, 611 7, 90
- Ryle, M. 1949, *Proceedings of the Physical Society A*, 62, 491, 491 11
- Safouris, V., Subrahmanyan, R., Bicknell, G. V., & Saripalli, L. 2009, *MNRAS*, 393, 2, 2 vi, 108
- Saripalli, L. 2012, *AJ*, 144, 85, 85 16
- Saripalli, L., Subrahmanyan, R., Thorat, K., et al. 2012, *ApJS*, 199, 27, 27 107, 110, 112, 127, 131
- Sault, R. J., Teuben, P. J., & Wright, M. C. H. 1995, in *Astronomical Society of the Pacific Conference Series*, Vol. 77, *Astronomical Data Analysis Software and Systems IV*, ed. R. A. Shaw, H. E. Payne, & J. J. E. Hayes, 433 29

## BIBLIOGRAPHY

---

- Sault, R. J., & Wieringa, M. H. 1994, *A&AS*, 108, 585, 585–33
- Schinnerer, E., Smolčić, V., Carilli, C. L., et al. 2007, *ApJS*, 172, 46, 46–7
- Schmidt, M. 1963, *Nature*, 197, 1040, 1040–3
- . 1965, *ApJ*, 141, 1, 1–12
- Seymour, N., Dwelly, T., Moss, D., et al. 2008, *MNRAS*, 386, 1695, 1695–18
- Shklovskii, I. S. 1961, *Soviet Astronomy*, 4, 885, 885–13
- Simpson, C., Rawlings, S., & Martínez-Sansigre, A. 2006, *Astronomische Nachrichten*, 327, 270, 270–65, 97, 98, 99
- Sirothia, S. K., Dennefeld, M., Saikia, D. J., et al. 2009, *MNRAS*, 395, 269, 269–64
- Smolčić, V., Schinnerer, E., Scodreggio, M., et al. 2008, *ApJS*, 177, 14, 14–18
- Solovyov, D. I., & Verkhodanov, O. V. 2011, *Astrophysical Bulletin*, 66, 416, 416–5
- Subrahmanyan, R., & Cowsik, R. 2013, *ArXiv e-prints*, arXiv:1305.7060 19
- Subrahmanyan, R., Ekers, R. D., Saripalli, L., & Sadler, E. M. 2010, *MNRAS*, 402, 2792, 2792–v, 28, 35, 66, 95
- Subrahmanyan, R., Saripalli, L., Safouris, V., & Hunstead, R. W. 2008, *ApJ*, 677, 63, 63–vi, 108
- Tasker, N. J., Condon, J. J., Wright, A. E., & Griffith, M. R. 1994, *AJ*, 107, 2115, 2115–4

## **BIBLIOGRAPHY**

---

- Urrutia, T., Becker, R. H., White, R. L., et al. 2009, *ApJ*, 698, 1095, 1095 5
- Valtonen, M. J. 1977, *ApJ*, 213, 648, 648 13
- van Weeren, R. J., Hoeft, M., Röttgering, H. J. A., et al. 2011, *A&A*, 528, A38, A38 4
- van Weeren, R. J., Röttgering, H. J. A., Brügger, M., & Hoeft, M. 2010, *Science*, 330, 347, 347 4
- Windhorst, R., Mathis, D., & Neuschaefer, L. 1990, in *Astronomical Society of the Pacific Conference Series*, Vol. 10, *Evolution of the Universe of Galaxies*, ed. R. G. Kron, 389–403 93
- Windhorst, R. A., Miley, G. K., Owen, F. N., Kron, R. G., & Koo, D. C. 1985, *ApJ*, 289, 494, 494 iv, 63
- Windhorst, R. A., van Heerde, G. M., & Katgert, P. 1984, *A&AS*, 58, 1, 1 89
- Wing, J., & Blanton, E. 2012, in *American Astronomical Society Meeting Abstracts*, Vol. 219, *American Astronomical Society Meeting Abstracts*, 207.04 16
- Wing, J. D., & Blanton, E. L. 2011, *AJ*, 141, 88, 88 vi, 108
- Wright, A. E., Griffith, M. R., Burke, B. F., & Ekers, R. D. 1994, *ApJS*, 91, 111, 111 4
- Wright, A. E., Griffith, M. R., Hunt, A. J., et al. 1996, *ApJS*, 103, 145, 145 4
- Yasuda, N., Fukugita, M., Narayanan, V. K., et al. 2001, *AJ*, 122, 1104, 1104 58, 59

## **BIBLIOGRAPHY**

---

Yee, H. K. C., & Green, R. F. 1984, ApJ, 280, 79, 79 vi, 108

York, D. G., Adelman, J., Anderson, Jr., J. E., et al. 2000, AJ, 120, 1579, 1579 5

Zhao, Y.-H., Huang, J.-S., Ashby, M., Fazio, G., & Miyazaki, S. 2009, Research  
in Astronomy and Astrophysics, 9, 1061, 1061 58, 59

Zirbel, E. L. 1997, ApJ, 476, 489, 489 vi, 108